



저작자표시-비영리-변경금지 2.0 대한민국

이용자는 아래의 조건을 따르는 경우에 한하여 자유롭게

- 이 저작물을 복제, 배포, 전송, 전시, 공연 및 방송할 수 있습니다.

다음과 같은 조건을 따라야 합니다:



저작자표시. 귀하는 원저작자를 표시하여야 합니다.



비영리. 귀하는 이 저작물을 영리 목적으로 이용할 수 없습니다.



변경금지. 귀하는 이 저작물을 개작, 변형 또는 가공할 수 없습니다.

- 귀하는, 이 저작물의 재이용이나 배포의 경우, 이 저작물에 적용된 이용허락조건을 명확하게 나타내어야 합니다.
- 저작권자로부터 별도의 허가를 받으면 이러한 조건들은 적용되지 않습니다.

저작권법에 따른 이용자의 권리는 위의 내용에 의하여 영향을 받지 않습니다.

이것은 [이용허락규약\(Legal Code\)](#)을 이해하기 쉽게 요약한 것입니다.

[Disclaimer](#)

공학박사학위논문

비틀림과 자기변형 패치 트랜스듀서의
등가 회로 모델 연구

Equivalent circuit model for torsional
magnetostrictive patch transducer

2019년 8월

서울대학교 대학원

기계항공공학부

이준규

비틀림과 자기변형 패치 트랜스듀서의 등가 회로 모델 연구

Equivalent circuit model for torsional
magnetostrictive patch transducer

지도교수 김 윤 영

이 논문을 공학박사 학위논문으로 제출함
2019년 7월

서울대학교 대학원
기계항공공학부
이 준 규

이준규의 공학박사 학위논문을 인준함
2019년 8월

위원장 : 조 맹 효

부위원장 : 김 윤 영

위 원 : 윤 병 동

위 원 : 김 도 년

위 원 : 승 홍 민

ABSTRACT

Equivalent circuit model for torsional magnetostrictive patch transducer

Jun Kyu Lee

School of Mechanical and Aerospace Engineering

The Graduate School

Seoul National University

The research in this dissertation aims at developing a fully coupled circuit model of a magnetostrictive patch transducer designed for generating and receiving the lowest torsional ($T(0,1)$) guided wave. Despite various types of magnetostrictive patch transducers have been developed, there appears no fully coupled circuit model to accurately account for the mechanism of wave actuation and sensing of the transducers. In addition, a circuit model to be useful for both wave actuation and sensing has not been proposed yet. Unlike piezoelectric transducers for which various circuit models for field variable quantification and their application are studied, however, the related research on the magnetostrictive patch transducers is very limited. The lack of such models makes it difficult for the magnetostrictive patch transducers to be further used in industrial applications. Motivated by this need,

we aim to develop a fully coupled circuit model of a magnetostrictive patch transducer used to generate and measure the lowest torsional (T(0,1)) guided wave. Prior to construct the quantitative circuit model, we compared the field variables from the existing simplified constitutive equations of the magnetostriction with those of strain gauge to confirm the possibility of quantification. After that, in order to achieve the aim, structural impedances considering both a specimen and the transducer are obtained. Nonlinear magnetostriction phenomenon in a magnetostrictive patch which requiring magnetic material properties is expressed in the designed equivalent circuit. In particular, the static magnetic field caused by the magnet, which greatly influences the magnetostriction phenomenon, is also considered in the equivalent circuit. These processes form a single model that converts a voltage output from the transducer to the actual strain in the specimen and vice versa. The validity of the developed model was confirmed by comparing the values of the predicted field variables and those by experiments.

Keywords: Guided wave, Magnetostriction, Magnetostrictive patch transducer, Quantification, Equivalent circuit

Student Number: 2012-23944

CONTENTS

ABSTRACT	i
CONTENTS.....	iii
LIST OF TABLES.....	vii
LIST OF FIGURES.....	viii
CHAPTER 1. INTRODUCTION	1
1.1 Motivation.....	1
1.2 Research Objectives	2
1.3 Outline of thesis	5
CHAPTER 2. THEORETICAL BACKGROUND.....	8
2.1 Magnetostriction.....	8
2.1.1 Overview of magnetostriction phenomenon	9
2.1.2 Nonlinear properties of magnetostrictive material	10
2.2 Guided waves in a hollow cylinder	13
2.2.1 Wave equation in a hollow cylinder	13
2.2.2 Torsional mode in a hollow cylinder	16
2.3 Circumferential Shear-Horizontal (SH) mode in a hollow cylinder.....	24
CHAPTER 3. MAGNETOSTRICTIVE PATCH TRANSDUCER FOR TORSIONAL ELASTIC WAVES	43
3.1 Configuration of the magnetostrictive patch transducer	44
3.2 Simplified analysis of magnetoelastic effect using magnetostriction	

equation.....	45
3.2.1 Linear magnetostriction equation.....	45
3.2.2 Effect of static magnetic field on the performance of magnetostrictive patch transducer.....	52
3.3 Relative quantification with qualified strain gauge.....	56
3.3.1 Experimental setup.....	56
3.3.2 Experimental validation	58
CHAPTER 4. STRUCTURAL IMPEDANCE MODEL OF SPECIMEN AND MAGNETOSTRICTIVE PATCH TRANSDUCER	80
4.1 Structural impedance model.....	81
4.1.1 Structural impedance configuration of specimen and magnetostrictive patch transducer.....	81
4.1.2 Input impedance by transmission line theory.....	83
4.2 Effective patch width by the shear lag phenomenon.....	87
CHAPTER 5. FULLY COUPLED CIRCUIT MODEL FOR MAGNETOSTRICTION IN MAGNETOSTRICTIVE PATCH TRANSDUCER	96
5.1 Fully coupled magnetostriction equation	97
5.1.1 Approximate expressions for nonlinear properties of magnetostrictive material (HiperCo 50A).....	97
5.1.2 Improvement of magnetostriction equation with consideration of nonlinear properties.....	99

5.2 Circuit model of torsional magnetostrictive patch transducer.....	105
5.2.1 Circuit equations converted from the mechanical equations.....	105
5.2.2 Equivalent circuit model based on torsional magnetostrictive patch transducer	109
CHAPTER 6. EXPERIMENTAL VERIFICATION FOR QUALIFICATION OF MAGNETOSTRICTIVE PATCH TRANSDUCER WITH FULLY COUPLED CIRCUIT MODEL	118
6.1 Experimental setup.....	119
6.2 Comparison of field variables from the circuit model and those of the experimental results.....	120
6.3 Database on measurement performance based on various variables.....	122
6.3.1 Changes in measurement performance due to the structural variables	122
6.3.2 Influence of static magnetic field by the permanent magnet.....	124
CHAPTER 7. CONCLUSIONS	139
APPENDIX A. MAGNETIC INTERFERENCES IN ULTRASONIC MAGNETOSTRICTIVE PATCH TRANSDUCERS	141
A.1 Overview	141
A.2 Analysis of the dynamic magnetic interference in a receiver	142
A.3 Analysis of the static magnetic interference between adjacent transmitters	146
REFERENCES.....	161

ABSTRACT (KOREAN)	176
ACKNOWLEDGEMENTS	178

LIST OF TABLES

Table 2.1 Selected Bessel functions depending on the range of ω	30
Table 2.2 λ value selection criterion according to the range of each frequency ..	31
Table 3.1 Material property and geometry of magnetostrictive patch transducer ...	64
Table 3.2 Comparison between theoretical and experimental natural frequencies of torsional vibration.....	65
Table 3.3 Specifications of the magnetostrictive patch transducer system	66
Table 4.1 List of frequency-specific equipment used in the experiments for verifying the proposed model.....	91

LIST OF FIGURES

Fig. 2.1 The inside of a ferromagnetic body rearranged by a magnetic field.....	32
Fig. 2.2 Nonlinear magnetostriction curve of a magnetostrictive material (HiperCo 50A).	33
Fig. 2.3 magnetization curve of a magnetostrictive material (pure nickel) with a hysteresis property [24]. The red line denotes experimental results and black line denotes simulation results.	34
Fig. 2.4 magnetostriction curve of a magnetostrictive material (pure nickel) with a hysteresis property [24]. The red line denotes experimental results and black line denotes simulation results.	35
Fig. 2.5 A plate of thickness $2h$. It is assumed to be infinitely long in the y direction.	36
Fig. 2.6 Coordinates for an infinitely long hollow circular cylinder.	37
Fig. 2.7 The geometry of a hollow cylinder with inner and outer radii, r_{in} and r_{out}	38
Fig. 2.8 Dispersion curve (Relation between frequency and wave number) for torsional waves in a hollow aluminum cylinder with an outer diameter of 25 mm and a thickness of 2 mm.	39
Fig. 2.9 Dispersion curve (Relation between group velocity and frequency) for torsional waves in a hollow aluminum cylinder with an outer diameter of	

25 mm and a thickness of 2 mm.	40
Fig. 2.10 Dispersion curve (Relation between frequency and wave number) for circumferential SH waves in a hollow aluminum cylinder with a different outer diameters 12 mm and 25 mm which have same thickness of 2 mm.	41
Fig. 2.11 Dispersion curve (Relation between group velocity and frequency) for circumferential SH waves in a hollow aluminum cylinder with a different outer diameters 12 mm and 25 mm which have same thickness of 2 mm.	42
Fig. 3.1 Coupling constants d_{11} , d_{35} calculated by the magnetostriction curve ...	67
Fig. 3.2 Schematic configuration of the proposed torsional magnetostrictive patch transducer for measuring torsional vibrations in a rotating shaft.....	68
Fig. 3.3 A cross sectional view of the magnetostrictive patch transducer (left figure) and the magnetic induction in the patch (right figure) for $N_p = 6$ and $R = 25$ mm, calculated by the two-dimensional magnetostatic finite element model.....	69
Fig. 3.4 The d_p distribution in the patch for varying N_p values. (The abscissa presents the position in a single patch where 0 represents the patch center.)	70
Fig. 3.5 The normalized mean values of d_p in the patch (d_p^{Norm}) (blue line) and the normalized peak-to-peak voltages of the transducer signals ($V_{\text{MTVS}}^{\text{Norm}}$) (red	

line) for varying N_p values.....	71
Fig. 3.6 Experimental setup for torsional vibration transduction in a stationary solid shaft of $R = 25$ mm. Magnetostrictive patch transducers are used both for vibration excitation and measurement. IDC cables (64 turns) are used as the solenoid coils of the transducer.....	72
Fig. 3.7 The time signals of the input current in the exciting magnetostrictive patch transducer and the induced voltage by the receiving magnetostrictive patch transducer.....	73
Fig. 3.8 Experimentally obtained torsional frequency response functions of the shafts of different lengths (L_s) by using the proposed transducer both as an exciter and a sensor. (The red dotted circles are used to indicate the peaks corresponding the eigenfrequencies.)	74
Fig. 3.9 Comparison of experimentally obtained torsional strain eigenmodes by using the transducers and the theoretical ones for a shaft of $L_s = 2$ m. The error rates on the node points of each mode are about less 5%.	75
Fig. 3.10 The experimental setup used to compare the signals measured by the MTVS and the strain gauge system with a telemetry unit. The hydraulic exciting system was used to generate torsional vibrations.	76
Fig. 3.11 The measured time signals, phases and their FFT results by (a) the strain gauge and (b) the magnetostrictive patch transducer installed on a stationary shaft excited at 20 Hz.....	77

Fig. 3.12 (a) The amplitudes of the measured signals by the magnetostrictive patch transducer at different excitation frequencies. (b) The comparison of the frequency-adjusted signals measured by the magnetostrictive patch transducer through (9) and the signals measured by the strain gauge. (c) The detailed plot of the dotted rectangular area in (b).....	78
Fig. 3.13 The measured signal amplitudes according to varying input voltages for three different excitation frequencies of 10, 20 and 30 Hz.	79
Fig. 4.1 Cross section of the specimen and the magnetostrictive patch transducer. the structural impedance configuration of these is shown in the blue box. ...	92
Fig. 4.2 Equivalent circuit model representing the structural impedance of the specimen and the magnetostrictive patch transducer.	93
Fig. 4.3 Deformation profile of the patch, the specimen and the adhesive layer. ...	94
Fig. 4.4 Model results according to shear lag effect.....	95
Fig. 5.1 Experimental configuration for HiperCo 50A magnetostriction analysis.	111
Fig. 5.2 Graphs of magnetic properties of HiperCo 50A. Experimentally obtained $M - H$ curve.	112
Fig. 5.3 Graphs of magnetic properties of HiperCo 50A. Experimentally obtained $\lambda - H$ curve and reference data.....	113
Fig. 5.4 Fundamental equivalent circuit model for magnetostriction. Basic model of the magnetostriction phenomenon	114
Fig. 5.5 Fundamental equivalent circuit model for magnetostriction. The model with additional coil parts for electric transfer energy.....	115

Fig. 5.6 The configuration of the magnetostrictive patch transducer used in this study.
..... 116

Fig. 5.7 Equivalent circuit model for non-linear magnetostriction phenomenon
considering solenoid coils for dynamic magnetic field and magnet for the
static magnetic field. 117

Fig. 6.1 Experimental configuration for comparison between the model and the
actual magnetostrictive patch transducer. For excitation performance, the
signal generated from the magnetostrictive patch transducer is converted
to a strain value through the strain gauge. For measurement performance,
the signal from the shaker is measured simultaneously with the
magnetostrictive patch transducer and the strain gauge to perform a
quantitative comparison. 126

Fig. 6.2 Comparison of excitation performance in low-frequency range (20 ~ 55 Hz).
The top graph shows the peak to peak values (red dots) of the measured
signals and the value obtained from the model simulation (blue solid line)
according to the frequencies, and the graph at the bottom compares the time
signals at 50 Hz. 128

Fig. 6.3 Comparison of measurement performance in low-frequency range (20 ~ 55
Hz). The top graph shows the peak to peak values (red dots) of the
measured signals and the value obtained from the model simulation (blue
solid line) according to the frequencies, and the graph at the bottom
compares the time signals at 50 Hz. 129

Fig. 6.4 Comparison of excitation performance in high-frequency range (50 ~ 150 kHz). The top graph shows the peak to peak values (red dots) of the measured signals and the value obtained from the model simulation (blue solid line) according to the frequencies, and the graph at the bottom compares the time signals at 60 kHz..... 130

Fig. 6.5 Comparison of measurement performance in high-frequency range (50 ~ 150 kHz). The top graph shows the peak to peak values (red dots) of the measured signals and the value obtained from the model simulation (blue solid line) according to the frequencies, and the graph at the bottom compares the time signals at 60 kHz..... 131

Fig. 6.6 Results for measured voltage values with distance from a shaker and frequency of a magnetostrictive patch transducer using a 25 mm wide patch attached to a steel solid shaft. (left) Low-frequency range measurement experiment, (right) low-frequency range model simulation. 132

Fig. 6.7 Results for measured voltage values with distance from a shaker and frequency of a magnetostrictive patch transducer using a 25 mm wide patch attached to a steel solid shaft. (left) High-frequency range measurement experiment, (right) high-frequency range model simulation. 133

Fig. 6.8 Results for measured voltage values with distance from a shaker and frequency of a magnetostrictive patch transducer using a 25 mm wide patch attached to an aluminum solid shaft. (left) Low-frequency range measurement experiment, (right) low-frequency range model simulation.

.....	134
Fig. 6.9 Results for measured voltage values with distance from a shaker and frequency of a magnetostrictive patch transducer using a 25 mm wide patch attached to an aluminum solid shaft. (left) High-frequency range measurement experiment, (right) high-frequency range model simulation.	135
.....	135
Fig. 6.10 Measurement results of the magnetostrictive patch transducer with 10 mm and 15 mm patch widths at low frequency range.....	136
Fig. 6.11 Measurement results of the magnetostrictive patch transducer with 10 mm and 15mm patch widths and the first mode resonant frequency (black solid line) of patches at high frequency range.	137
Fig. 6.12 Comparison of signal amplitude results from the model (solid line) and the experiment (dash-dotted line) according to the intensity of the permanent magnet.....	138
Fig. A.1 Experimental setups (a) for measurement of a cross-talk signal and (b) for investigation of the mutual interference caused by a static magnetic field.	154
.....	154
Fig. A.2 (a) Photo of the developed PCB based OL-MPT. The nickel patch (not shown) is located under the dashed circle. (b) The OL-MPT shielded by aluminum foil. (c) The cross-talk signals of the OL-MPT without aluminum foil (blue diamonds) and of the OL-MPT with aluminum foil (red circles) installed on an aluminum plate.	155

Fig. A.3 The Gabor pulse centered at 400 kHz used as the excitation signal, plotted in (a) the time and (b) frequency domains.156

Fig. A.4 Radiation patterns of the normalized magnitudes of Lamb wave signals obtained (a) from the experiments, (b) from the semi-analytic analysis and (c) variance ratios of the normalized magnitudes of Lamb wave signals obtained from the experiments (blue line with circles) and the semi-analytic analysis (red line with rectangles).157

Fig. A.5 Schematic illustrations of magnetic fields distributions in the transmitter (a) without and (b) with an external magnet and a magnetostrictive patch for the magnetic interference.158

Fig. A.6 Radiation pattern of strain S_{xx} when a receiver is located on the x axis and an external magnet and a patch are located on the η direction.159

Fig. A.7 Relation of the distance of limit L_{limit} and the patch diameter D . The fitted curve refers to the linear relation between them.160

CHAPTER 1.

INTRODUCTION

1.1 Motivation

A magnetostrictive patch transducer (MPT) is a transducer using a magnetostriction phenomenon which refers to the coupling phenomenon between strain and magnetic field in a ferromagnetic material. They typically consist of thin magnetostrictive patches, magnets providing static bias magnetic field and coils providing dynamic magnetic field. Depending on the type of generated (measured) waves, the field directions can be either parallel or perpendicular. The advantages of using these transducers are that they can generate and measure vibrations and ultrasonic waves at a low cost with a relatively simple structure [1-8]. Compared with more-widely used piezoelectric transducers, they do not require direct wiring to the transducers. Therefore, they can be useful when direct wiring should be avoided as in the vibration measurement of rotating shafts [9-11]. Unlike piezoelectric transducers for which various circuit models for field variable quantification and their application [12-16] are available, however, the related research on the magnetostrictive patch transducers is very limited. The lack of such research makes it difficult for the magnetostrictive patch transducers to be further used in industrial applications. Motivated by this need, we aim to quantify the magnetostrictive patch transducer by

analyzing the structural and magnetic properties.

In the case of magnetostrictive patch transducer, we should consider both mechanical deformation and magnetic properties of magnetostrictive patches. In most earlier studies, relatively simple magnetic field models were used. For instance, the ideal condition by means of an infinitely long coil is adapted instead of a permanent magnet [17-19] when externally applied static field is considered. Or a simplified linear magnetic model was to depict the static magnetic behavior [20, 21]. To consider external static magnetic field, Choi et al. [22] expressed the impedance of the magnetostrictive transducer using an equivalent circuit. However, their model did not consider static magnetic field and the actual impedance value of an MPT was quite different from that calculated from their model. On the other hand, Clemente et al. [23] took into account the effect of permanent magnets on the circuit model and the voltage outputs predicted by their model were quite close to those obtained experimentally. However, this study, mainly focused on energy harvesting, considers a model valid for measurement not for excitation. Therefore, a unified model equally applicable to both measurement and excitation should be developed for precise quantification of magnetostrictive patch transducers to increase the applicability in industrial field.

1.2 Research Objectives

In this study, the model of a magnetostrictive patch transducer for torsion installed on a cylindrical structural specimen will be covered. As mentioned above, a magnetostrictive patch transducer is possible to operate without contact with the specimen because of the gap between the patch and the coil. While a piezoelectric transducer is difficult to produce a torsional deformation, a magnetostrictive patch transducer can simply deal with a pure torsional deformation. Therefore, that configuration of the transducer is adapted in this study because it is judged that it would have a unique advantage over other transducers in industrial field application.

The main objective of this research is to develop a precise model of the magnetostrictive patch transducer for quantification. In order to target the actual physical quantity like a strain or a voltage through the advanced model, both the quantification possibility and the consideration of the structure and the magnetic characteristics of the magnetostrictive patch transducer should be confirmed.

The specific objectives concerned in this research can be summarized as follows:

- *Relative calibration of magnetostrictive patch transducer*

Contents begin with the working principle of the magnetostrictive patch transducer and to express the magnetostriction phenomenon inside the magnetostrictive patch using simplified linear equations. These equations are not quantitative, but they provide the behavior of magnetostrictive phenomenon. Then, the numerical findings

by these equations are compared with results from experiments performed in a solid shaft on a laboratory. Furthermore, the measurement results by the magnetostrictive patch transducer are compared with those obtained by the commercial strain gauge system [24, 25]. The comparison not only validates the effectiveness of the magnetostrictive patch transducer but also confirms the suggested frequency-dependent calibration scheme.

● Construction of equivalent circuit model for magnetostrictive patch transducer

For precise quantification, the proposed model needs to consider nonlinear magnetostrictive phenomenon of a magnetostrictive patch, the mechanical impedance of the patch and a test specimen and the applied static bias magnetic field. The derived full-coupled circuit model is constructed to be valid for both actuation and sensing. Therefore, the model can convert a voltage output from the transducer to the actual strain in the test specimen and vice versa. It may be worth elaborating on the development of the model. First of all, the magnetic constitutive relation as well as the strain-magnetic strength relation of the magnetostrictive patch material is identified. Here, HiperCo 50A [26] is used as the material. The structural impedances of the patch and specimen are calculated by considering their geometry and material properties and are considered in developing the circuit model. Not only the static magnetic field by a permanent magnet but also its resistance is considered in the model. Then the overall magnetostriction phenomenon, representing the conversion between mechanical energy (strain) and electromagnetic energy (voltage),

can be explained by the developed model. To check the validity of the developed model, the predicted field quantities (voltage and strain) by the developed model are compared with those obtained by experiments. Furthermore, the model is checked if it is valid when a different specimen material is used and also when the patch dimensions and the frequency ranges are altered.

1.3 Outline of thesis

In Chapter 2, theoretical backgrounds of magnetostriction phenomenon and general information of guided wave based NDE (Non-destructive evaluation) and SHM (Structural health monitoring) are explained. The theory on the magnetostriction is described first. Then theory of guided waves in cylinder are then introduced. Among several wave modes, torsional waves and circumferential shear-horizontal waves are handled in detail.

In Chapter 3, magnetostrictive patch transducer for torsional elastic waves which is used in this study is introduced. First, the configuration and working principle of the transducer are presented. After that, simplified analysis of magnetoelastic effect using magnetostriction equation is done. In this analysis, linear magnetostriction equations are used and the effect of static magnetic field on the magnetostrictive patch transducer is also examined. The preceding analysis will be compared to the experimental values of a magnetostrictive patch transducer and the relative

calibration of the magnetostrictive patch transducer is performed through an already validated strain gauge.

In Chapter 4, In order to construct a fully-coupled model for quantification, the physical structure of the transducer and the specimen are considered. Therefore, structural impedances based on cylinder or shaft type specimen and magnetostrictive patch attached on the specimen are constructed. Using this impedances, the overall input impedance of the transducer is obtained through transmission line theory. In addition, considering the adhesive layer between the specimen and the patch, the effective patch width is taken into impedance by shear lag phenomenon.

In Chapter 5, a fully coupled model expressing the magnetostriction phenomenon occurring inside the patch is constructed. In order to improve the lack of linear equations, the nonlinear properties of materials are obtained and the magnetostriction equations are improved. The nonlinear property values for the HiperCo 50A used here are obtained by approximate expressions through experiments. The improved magnetostriction equations are transformed into equivalent circuit equations using electrical circuit elements, and a circuit model of the magnetostrictive patch transducer can be built on this basis. Finally, applying the structural impedance obtained in Chapter 4, a fully coupled model considering both the entire specimen and the transducer can be built.

In Chapter 6, experimental verification of the previously constructed model so far and quantification is carried out. The field variables obtained from the model according to both actuation and sensing are compared with those obtained from the experiment. The correspondence of the field variables verifies the quantification of the transducer through the proposed model. Also, in order to know the robustness of the model according to various variables, the database is constructed by changing the structural variables such as the material of specimen or size of the patch and the static magnetic field which greatly affects the magnetostriction phenomenon.

In Chapter 7, the conclusion remarks for this research will be presented.

CHAPTER 2.

THEORETICAL BACKGROUND

2.1 Magnetostriction

The magnetostriction phenomenon, which is the basis of the magnetostrictive patch transducer, is described in detail. And it is a chapter about the dispersion phenomenon of guided wave in the specimen which is mainly aimed at the transducer and the properties of magnetostrictive materials that exhibit this phenomenon are discussed.

First, magnetostriction is a phenomenon that occurs due to the coupling between magnetic field and mechanical deformation, which is a characteristic of ferromagnetic materials. Properties such as the nonlinearity of the magnetostrictive material itself that exhibit this phenomenon will be described in accordance with the transducer operating basis. Magnetostrictive transducers generate and measure elastic waves mainly in waveguides such as plates and pipes. These media have properties that change wave characteristics (mode, speed, etc.) according to frequency and material properties. Therefore, the wave-dispersion phenomena of guided waves will be explained in order to provide an overall understanding of the use of transducers.

2.1.1 Overview of magnetostriction phenomenon

The magnetostriction phenomenon is a phenomenon that occurs in a ferromagnetic body, and refers to a phenomenon in which mechanical deformation occurs when a magnetic field is applied from the outside. In 1842, James Joule discovered the phenomenon when experimenting with iron and called the Joule effect [27], which increases in size when a magnetic field is applied.

The ferromagnetic body is basically in a stable state that balances the internal magnetism to be the same. When a magnetic field is applied to the ferromagnetic material, the internal structure starts to be rearranged by the movement and rotation according to the direction of the magnetic field. In the case of the ferromagnetic material, since the internal structure has a magnetocrystalline anisotropy, a change in the volume of the film is caused (Figure. 2.1).

Since magnetostriction phenomenon has a second order relation between input and output as in figure. 2.2, if the direction of the external magnetic field is changed, the direction of deformation does not change and the reverse phenomenon does not occur. In other words, even if force is applied from the outside, the magnetic state does not change. However, this means that the reverse phenomenon does not occur in the

initial state in which the material has no magnetic field or electric field at all. If an external force is exerted in a state where an appropriate magnetic field is applied from the outside, the magnetic state changes.

In addition to the magnetostriction phenomena found by Joule, there are several ways to explain magnetostriction according to some conditions and the direction of the phenomenon. When externally applied force is applied to the magnetic field of the bias, there is a phenomenon that the magnetic state of the target material changes and is called the Villari effect [28] after the discoverer Villari. The Matteucci effect [29] is a phenomenon in which the magnetic state changes in a helical direction when a torque is applied, and the Wiedemann effect [30] is a phenomenon in which a torsional deformation occurs when a magnetic field is applied in a helical direction.

2.1.2 Nonlinear properties of magnetostrictive material

It is nonlinearity that makes the biggest difficulty in using magnetostriction phenomenon in transducers. In the case of using a magnetostrictive transducer, a certain condition can be solved to some extent by designing only the linear characteristic. However, in addition to nonlinearity, Hysteresis is a difficult factor in quantifying the performance of a transducer.

Hysteresis, as shown in figure 2.3, is the state of the system changes according to the progress of the system, which causes the transducer to have different values of generations / measurements by the process in the same situation. Generally, when the propulsion is weak, it is not a big problem, but when the performance of the transducer is maximized and the propulsion is desired to be strong, this effect will appear. In addition to magnetostrictive materials, piezoelectric materials also exhibit such hysteresis phenomenon, and studies are underway to interpret them [31]. However, this chapter only explains the information of the hysteresis required from using the magnetostrictive transducer and the basic method to overcome it.

When the ferromagnetic body is magnetized in one direction, the magnetized characteristics do not completely disappear even if the magnetic field applied for magnetization is removed. In order to completely eliminate this magnetized property, it is necessary to apply a magnetic field in the opposite direction. If the changing magnetic field is applied to the ferromagnetic material, the magnetization moves along the Hysteresis curve, which is related to the presence of the magnetic domain of the ferromagnetic material. If the magnetic field is rearranged, additional energy is needed to reverse it. This characteristic is called a "magnetic memory" of a ferromagnetic body, and a material permanently memorizing the magnetization added by such memory is referred to as "permanent magnet".

The magnetization component that can not be returned due to the rearrangement is

restored by itself when it is left in a natural state for a long time, which is the most classical method for preventing the hysteresis of the transducer. In order to reduce the time, the magnetization of the material is made zero by using a demagnetizer. The way to reduce hysteresis without this additional work is to use a material that is less impacted because the hysteresis curve itself is narrow. Tefenol-D, Galfenol, and HiperCo, which are alloys used mainly in transducers, are different from iron, which is a general ferromagnetic material, and are used with influence of strong magnetostriction characteristic and relatively negligible small Hysteresis curve.

There are many ways, but that does not mean that Hysteresis will disappear completely. Therefore, by suggesting a reasonable quantitative model for hysteresis, studies have been carried out to consider the effect of hysteresis. Typically, there are Preisach model [32] and Domain wall model [33], both of which are based on Jiles and Atherton's magnetic theory [34]. If these two models were the study of the hysteresis of the material itself, there are also studies to reduce the effect of the hysteresis, considering the overall devices and systems in addition to the material [31].

The magnetostrictive Hysteresis curve changes with the preload applied to the material (Figure 2.5). If external forces are applied, the magnetic properties will also change as they affect the movement and rotation of the internal structure of the material. Generally, when the force is applied, the saturation strain of the

magnetostriction curve increases [31]. However, it is possible to improve the performance of the magnetostrictive material by applying a moderate intensity force because the saturation strain is reduced again from a certain moment when the force is applied too much. In addition, since the slope and hysteresis of the magnetostriction curve are changed, it is useful to consider the change of the magnetostriction curve according to the preload so that the hysteresis is narrowly formed even in a small magnetic field.

2.2 Guided waves in a hollow cylinder

Because the magnetostrictive patch transducers are supposed to be used in waveguides, the understanding of their underlying wave physics, such as dispersion relations, is crucial to choose appropriate types of magnetostrictive patch transducers. Accordingly, this subsection discusses the dispersion relations in a hollow cylinders (pipes).

2.2.1 Wave equation in a hollow cylinder

Let's start with the elasticity theory, which shows total wave propagation, before considering the cylinder. Thick plate and lamb wave are considered for easy understanding of the equation of elasticity theory. As the first kind of guided waves,

the Lamb waves in elastic plate of thickness can be considered. Specifically, the guided Lamb waves propagating along the x axis in a plate of thickness $2h$ is considered. The plate is assumed to be infinitely long in the y direction, satisfying the plane strain condition. The top and bottom surfaces (at $z = \pm h$) are traction-free. The Lamb waves can be a wave mode resulting from the coupling between the longitudinal wave (which is usually referred to as the P wave) and vertical-horizontal wave (which is usually referred to as the SV wave) that propagate in an infinite medium. The coupling inevitably occurs in order to satisfy the traction-free boundary condition. Because the thickness in the z direction is finite, the Lamb wave forms standing wave forms in the z direction while it generates propagating or evanescent waves in the x direction. Depending on the symmetry of wave motion about the $z = 0$ plane, the Lamb wave can be grouped into the symmetric modes denoted by S_0, S_1, S_2, \dots and the antisymmetric modes denoted by A_0, A_1, A_2, \dots . Here, S_0 and A_0 are the lowest mode and thus n in S_n and A_n denotes the $(n+1)$ th mode.

If the elastodynamic equation is written for an elastic medium having two Lamé constants (μ and λ) and density (ρ) as

$$\mu \nabla^2 \mathbf{u} + (\lambda + \mu) \nabla \nabla \cdot \mathbf{u} = \rho \frac{\partial^2 \mathbf{u}}{\partial t^2}. \quad (2.1)$$

the displacement vector \mathbf{u} can be expressed in term of a scalar potential ϕ and a vector potential \mathbf{A} through the Helmholtz decomposition as

$$\mathbf{u} = \nabla \phi + \nabla \times \mathbf{A} \quad (2.2)$$

$$\nabla \cdot \mathbf{A} = f . \quad (2.3)$$

where equation (2.3) is the gage condition. Typically, f is chosen to be zero (for the dispersion analysis for a plate) but one can show that as long as f satisfies the following condition

$$\left(\nabla^2 - \frac{1}{(c_T)^2} \right) f = 0 . \quad (2.4)$$

where c_L and c_T are called the speeds of the longitudinal and shear waves, respectively, in an elastic medium composing the plate. They can be explicitly written as

$$c_L = \sqrt{\frac{\lambda + 2\mu}{\rho}} , \quad c_T = \sqrt{\frac{\mu}{\rho}} . \quad (2.5)$$

The general gage condition with nonzero f will be used later for the dispersion analysis of hollow cylinders.

2.2.2 Torsional mode in a hollow cylinder

This time, we consider longitudinal waves propagating along the z axis in a hollow cylinder shown in figure 2.6. The cylinder is traction-free on its inner and outer radii as

$$\sigma_{rr} = \sigma_{rz} = \sigma_{r\theta} = 0 \quad \text{at } r = r_{in} \quad \text{and } r = r_{out}. \quad (2.6)$$

To find the dispersion relation for longitudinal waves in a hollow cylinder, the following form of displacement field may be assumed [35]

$$\begin{aligned} u_r &= U_r(r) \cos(n\theta) e^{i(kz - \omega t)}, \\ u_\theta &= U_\theta(r) \sin(n\theta) e^{i(kz - \omega t)}, \\ u_z &= U_z(r) \cos(n\theta) e^{i(kz - \omega t - \pi/2)}. \end{aligned} \quad (2.7)$$

where u_r , u_θ and u_z are the radial, circumferential and axial displacement components and n is the Fourier number in the circumferential direction

($n = 0, 1, 2, \dots$). Because the cylinder forms a complete annular cross section, the Fourier harmonics in the θ direction. One can also consider an alternative set of the Fourier harmonics by replacing $\cos n\theta$ and $\sin n\theta$ in equation (2.7) by $\sin n\theta$ and $\cos n\theta$, respectively but the same dispersion relation should be obtained except $n=0$. For $n=0$, the field behaving as $u_r, u_z \sim \cos(0\theta)$ and $u_\theta = 0$ denotes the longitudinal wave by and the field behaving $u_\theta \sim \cos(0\theta)$, the torsional wave. The waves associated with $n \neq 0$ will be denoted by the flexural waves. It is common practice to denote the follow symbols to denote different wave types as

$$\begin{aligned}
 &\text{Longitudinal wave: } L(0, m) \\
 &\text{Torsional wave: } T(0, m) \\
 &\text{Flexural wave: } F(n, m)
 \end{aligned} \tag{2.8}$$

where $m = 1, 2, \dots$ denotes the mode number.

Using the Helmholtz resolution in equation (2.2), the potential function ϕ and \mathbf{A} must satisfy

$$\nabla^2 \phi = \frac{1}{c_L} \frac{\partial^2 \phi}{\partial t^2}, \tag{2.9}$$

$$\nabla^2 \mathbf{A} = \frac{1}{c_T} \frac{\partial^2 \mathbf{A}}{\partial t^2}, \quad (2.10)$$

with

$$\nabla = \mathbf{e}_r \frac{\partial}{\partial r} + \mathbf{e}_\theta \frac{\partial}{r \partial \theta} + \mathbf{e}_z \frac{\partial}{\partial z}, \quad (2.11)$$

$$\mathbf{A} = A_r \mathbf{e}_r + A_\theta \mathbf{e}_\theta + A_z \mathbf{e}_z \quad (2.12)$$

where \mathbf{e}_r , \mathbf{e}_θ , and \mathbf{e}_z are the unit base vectors in the r , θ and z directions, respectively. If the potential functions of the following forms are inserted into equations (2.9) and (2.10),

$$\begin{aligned} \phi &= \Phi(r) \cos(n\theta) e^{i(kz - \omega t)}, \\ A_r &= \Psi_r(r) \sin(n\theta) e^{i(kz - \omega t - \pi/2)}, \\ A_\theta &= \Psi_\theta(r) \cos(n\theta) e^{i(kz - \omega t - \pi/2)}, \\ A_z &= \Psi_z(r) \sin(n\theta) e^{i(kz - \omega t)}. \end{aligned} \quad (2.13)$$

The governing equations for $\Phi(r)$, $\Psi_r(r)$, $\Psi_\theta(r)$, and $\Psi_z(r)$ are obtained as

$$\left[\frac{d^2}{d(\alpha r)^2} + \frac{1}{\alpha r} \frac{d}{d(\alpha r)} - \left(\frac{n^2}{(\alpha r)^2} - 1 \right) \right] \Phi = 0, \quad (2.14)$$

$$\left[\frac{d^2}{\partial(\beta r)^2} + \frac{1}{\beta r} \frac{d}{d(\beta r)} - \left(\frac{n^2}{(\beta r)^2} - 1 \right) \right] \Psi_z = 0, \quad (2.15)$$

$$\left[\frac{\partial^2}{d(\beta r)^2} + \frac{1}{\beta r} \frac{d}{d(\beta r)} - \left(\frac{(n+1)^2}{(\beta r)^2} - 1 \right) \right] (\Psi_r - \Psi_\theta) = 0, \quad (2.16)$$

$$\left[\frac{d^2}{d(\beta r)^2} + \frac{1}{\beta r} \frac{d}{d(\beta r)} - \left(\frac{(n-1)^2}{(\beta r)^2} - 1 \right) \right] (\Psi_r + \Psi_\theta) = 0, \quad (2.17)$$

where

$$\alpha = \sqrt{\frac{\omega^2}{c_L^2} - k^2}, \quad \beta = \sqrt{\frac{\omega^2}{c_T^2} - k^2}. \quad (2.18)$$

The general solutions to equations (2.9) – (2.10) can be as follows,

$$\begin{aligned} \Phi &= AZ_n(\alpha_1 r) + BW_n(\alpha_1 r), \\ \Psi_z &\triangleq G_3 = A_3 Z_n(\beta_1 r) + B_3 W_n(\beta_1 r), \\ \frac{\Psi_r - \Psi_\theta}{2} &\triangleq G_1 = A_1 Z_{n+1}(\beta_1 r) + B_1 W_{n+1}(\beta_1 r), \\ \frac{\Psi_r + \Psi_\theta}{2} &\triangleq G_2 = A_2 Z_{n-1}(\beta_1 r) + B_2 W_{n-1}(\beta_1 r). \end{aligned} \quad (2.19)$$

In equation (2.14), the symbol Z denotes the Bessel function (J) and modified Bessel function (I) of the first kind and the symbol W , the Bessel function (Y) and modified Bessel function (K) of the second kind. Depending on the range of ω , different functions should be taken. Table 1 summarizes the functions to be used depending on the range of ω . Among the Bessel functions shown in table 1, J and Y are oscillatory while I and K are non-oscillatory.

Equations (2.13) show that 4 potential functions are used to represent three displacement field u_r , u_θ and u_z . To eliminate redundancy, one may choose require that $G_2 = 0$, which still satisfies the gage condition (2.4). Accordingly, $A_\theta = -A_r = -G_1$. Substituting this result yields,

$$\begin{aligned}
 U_r &= \frac{\partial \Phi}{\partial r} + \frac{n}{r} \Psi_z + k \Psi_r, \\
 U_\theta &= -\frac{n}{r} \Phi + k \Psi_r - \frac{\partial \Psi_z}{\partial r}, \\
 U_z &= -k \Phi - \frac{\partial \Psi_r}{\partial r} - (n+1) \frac{\Psi_r}{r}.
 \end{aligned} \tag{2.20}$$

Calculating the stress from equation (2.20) and imposing the traction-free boundary condition which is equation (2.6), the following equation must hold for a nontrivial

solution.

Since the equation for the displacement field is obtained, 6 characteristic equations can be obtained by substituting this into the boundary condition of equation (2.6) as in the case of the plate. The following equations can be obtained through the determinant consisting of A , B , A_1 , B_1 , A_3 and B_3 .

$$|c_{ij}| = 0, \quad (i, j = 1, 2, 3, 4, 5, 6). \quad (2.21)$$

In order to obtain an exact matrix, all 36 elements need to be known. However, if the axisymmetric mode is considered only, the θ direction is independent and $n = 0$ is satisfying, so equation (2.21) is separated into subdeterminants as.

$$D_1 \cdot D_2 = 0, \quad (2.22)$$

$$D_1 = \begin{vmatrix} c_{11} & c_{12} & c_{14} & c_{15} \\ c_{31} & c_{32} & c_{34} & c_{35} \\ c_{41} & c_{42} & c_{44} & c_{45} \\ c_{61} & c_{62} & c_{64} & c_{65} \end{vmatrix}, \quad (2.23)$$

$$D_2 = \begin{vmatrix} c_{23} & c_{26} \\ c_{53} & c_{56} \end{vmatrix}. \quad (2.24)$$

Thus, matrix elements in equations (2.22) - (2.24) can be summarized as,

$$\begin{aligned}
c_{11} &= \left[2n(n-1) - (\beta^2 - k^2)\alpha^2 \right] Z_n(\alpha_1 a) + 2\lambda_1 \alpha_1 a Z_{n+1}(\alpha_1 a), \\
c_{12} &= 2k\beta_1 a^2 Z_n(\beta_1 a) - 2ka(n+1)Z_{n+1}(\beta_1 a), \\
c_{14} &= \left[2n(n-1) - (\beta^2 - k^2)a^2 \right] W_n(\alpha_1 a) + 2\alpha_1 a W_{n+1}(\alpha_1 a), \\
c_{15} &= 2\lambda_2 k\beta_1 a^2 W_n(\beta_1 a) - 2(n+1)ka W_{n+1}(\beta_1 a), \\
c_{23} &= -\left[2n(n-1) - \beta^2 a^2 \right] Z_n(\beta_1 a) - 2\lambda_2 \beta_1 a Z_{n+1}(\beta_1 a), \\
c_{26} &= -\left[2n(n-1) - \beta^2 a^2 \right] W_n(\beta_1 a) - 2\beta_1 a W_{n+1}(\beta_1 a), \\
c_{31} &= 2nk\alpha_1 Z_n(\alpha_1 a) - 2\lambda_1 k\alpha_1 a^2 Z_{n+1}(\alpha_1 a), \\
c_{32} &= n\beta_1 a Z_n(\beta_1 a) - (\beta^2 - k^2)a^2 Z_{n+1}(\beta_1 a), \\
c_{34} &= 2nka W_n(\alpha_1 a) - 2k\alpha_1 a^2 W_{n+1}(\alpha_1 a), \\
c_{35} &= \lambda_2 n\beta_1 a W_n(\beta_1 a) - (\beta^2 - k^2)a^2 W_{n+1}(\beta_1 a), \\
c_{41} &= \left[2n(n-1) - (\beta^2 - k^2)\alpha^2 \right] Z_n(\alpha_1 b) + 2\lambda_1 \alpha_1 b Z_{n+1}(\alpha_1 b), \\
c_{42} &= 2k\beta_1 b^2 Z_n(\beta_1 b) - 2kb(n+1)Z_{n+1}(\beta_1 b), \\
c_{44} &= \left[2n(n-1) - (\beta^2 - k^2)b^2 \right] W_n(\alpha_1 b) + 2\alpha_1 b W_{n+1}(\alpha_1 b), \\
c_{45} &= 2\lambda_2 k\beta_1 b^2 W_n(\beta_1 b) - 2(n+1)kb W_{n+1}(\beta_1 b), \\
c_{53} &= -\left[2n(n-1) - \beta^2 b^2 \right] Z_n(\beta_1 b) - 2\lambda_2 \beta_1 b Z_{n+1}(\beta_1 b),
\end{aligned} \tag{2.25}$$

$$\begin{aligned}
c_{56} &= -[2n(n-1) - \beta^2 b^2] W_n(\beta_1 b) - 2\beta_1 b W_{n+1}(\beta_1 b), \\
c_{61} &= 2nk\alpha_1 Z_n(\alpha_1 b) - 2\lambda_1 k\alpha_1 b^2 Z_{n+1}(\alpha_1 b), \\
c_{62} &= n\beta_1 b Z_n(\beta_1 b) - (\beta^2 - k^2) b^2 Z_{n+1}(\beta_1 b), \\
c_{64} &= 2nkb W_n(\alpha_1 b) - 2k\alpha_1 b^2 W_{n+1}(\alpha_1 b), \\
c_{65} &= \lambda_2 n\beta_1 b W_n(\beta_1 b) - (\beta^2 - k^2) b^2 W_{n+1}(\beta_1 b).
\end{aligned}
\tag{2.25}$$

cont'd

In case of λ , the value should be selected according to the condition which is written in table 2.

In the case of equation (2.23), it is independent of θ and has only components u_r and u_z , so it corresponds to the longitudinal wave, and thus can be called the dispersion equation of the longitudinal wave. However, equation (2.24) corresponds to a torsional wave because only u_θ component exists and can also be referred to as a dispersion equation of a torsional wave.

In the developed equations, these dispersion equations can also be solved numerically, and the numerical dispersion of the dispersion curves is shown in figure 2.8 and 2.9 respectively.

2.3 Circumferential Shear-Horizontal (SH) mode in a hollow cylinder

In hollow cylinders, we first consider the circumferential waves that propagate along the circumferential direction in a hollow cylinder. In this case, it is certainly convenient to use the cylindrical coordinates (r, θ, z) .

To find the dispersion relation for the circumferential waves, one may assume the following displacement field,

$$u_r = u_r(r, \theta), \quad u_\theta = u_\theta(r, \theta), \quad u_z = 0. \quad (2.26)$$

where u_r and u_θ denote the radial and circumferential displacement components.

To impose the traction-free conditions at its inner and outer radii such that

$$\sigma_{rr} = \sigma_{r\theta} = 0 \quad \text{at } r = r_{in} \quad \text{and } r = r_{out}, \quad (2.27)$$

we need to express the stress components in terms of the displacement by using linear constitutive relations as

$$\sigma_{rr} = \lambda \left(\frac{\partial u_r}{\partial r} + \frac{u_r}{r} + \frac{1}{r} \frac{\partial u_\theta}{\partial \theta} \right) + 2\mu \frac{\partial u_r}{\partial r}, \quad (2.28)$$

$$\sigma_{\theta\theta} = \lambda \left(\frac{\partial u_r}{\partial r} + \frac{u_r}{r} + \frac{1}{r} \frac{\partial u_\theta}{\partial \theta} \right) + 2\mu \left(\frac{u_r}{r} + \frac{1}{r} \frac{\partial u_\theta}{\partial \theta} \right), \quad (2.29)$$

$$\sigma_{r\theta} = \mu \left(\frac{\partial u_\theta}{\partial r} + \frac{u_\theta}{r} + \frac{1}{r} \frac{\partial u_r}{\partial \theta} \right) \quad (2.30)$$

To facilitate the derivation of the dispersion relation, two potentials ϕ and ψ as in the Lamb wave case can be introduced:

$$\begin{aligned} u_r &= \frac{\partial \phi}{\partial r} + \frac{1}{r} \frac{\partial \psi}{\partial \theta} \\ u_\theta &= \frac{1}{r} \frac{\partial \phi}{\partial \theta} - \frac{\partial \psi}{\partial r} \end{aligned} \quad (2.31)$$

Substituting equation (2.27) into equation (2.1) yields the governing equations for ϕ and ψ :

$$\begin{aligned} \left(\frac{\partial^2}{\partial r^2} + \frac{1}{r} \frac{\partial}{\partial r} + \frac{1}{r^2} \frac{\partial^2}{\partial \theta^2} \right) \phi + \frac{\omega^2}{c_L^2} \phi &= 0 \\ \left(\frac{\partial^2}{\partial r^2} + \frac{1}{r} \frac{\partial}{\partial r} + \frac{1}{r^2} \frac{\partial^2}{\partial \theta^2} \right) \psi + \frac{\omega^2}{c_T^2} \psi &= 0 \end{aligned} \quad (2.32)$$

The general time-harmonic solutions to equation (2.32) can be put into the following

form as,

$$\begin{aligned}\phi &= \Phi(r)e^{i(k_\theta r_{out}\theta - \omega t)} \\ \psi &= \Psi(r)e^{i(k_\theta r_{out}\theta - \omega t)}\end{aligned}\tag{2.33}$$

In equation (2.33), it is assumed that the wave propagates along the circumferential direction as $e^{ik_\theta r_{out}\theta}$ where k_θ is the angular wavenumber and r_{out} is introduced to make the dimension of the angular wavenumber be 1/length. Substituting equation (2.33) into equation (2.32) yields ordinary differential equations for Φ and Ψ such that

$$\begin{aligned}\frac{\partial^2 \Phi}{\partial r^2} + \frac{1}{r} \frac{\partial \Phi}{\partial r} + \left[\left(\frac{\omega}{c_L} \right)^2 - \left(\frac{k_\theta r_{out}}{r} \right)^2 \right] \Phi &= 0, \\ \frac{\partial^2 \Psi}{\partial r^2} + \frac{1}{r} \frac{\partial \Psi}{\partial r} + \left[\left(\frac{\omega}{c_T} \right)^2 - \left(\frac{k_\theta r_{out}}{r} \right)^2 \right] \Psi &= 0.\end{aligned}\tag{2.34}$$

The general solutions to equation (2.34) can be expressed as

$$\Phi(r) = A_1 J_{k_\theta r_{out}} \left(\frac{\omega r}{c_L} \right) + A_2 Y_{k_\theta r_{out}} \left(\frac{\omega r}{c_L} \right),\tag{2.35}$$

$$\Psi(r) = B_1 J_{k_\theta r_{out}} \left(\frac{\omega r}{c_T} \right) + B_2 Y_{k_\theta r_{out}} \left(\frac{\omega r}{c_T} \right).$$

where $J_M(z)$ and $Y_M(z)$ are the Bessel functions of the first and second kinds, respectively and M denotes the order of the Bessel function. The symbols A_1 , A_2 , B_1 and B_2 are unknown constants. If equation (2.33) is substituted into equation (2.28) and (2.30) through equation (2.31), one can find the following expressions for Φ and Ψ can be obtained:

$$\begin{aligned} \sigma_{rr}(r, \theta) &= \frac{\mu e^{ik_\theta r_{out} \theta}}{r^2} \left[\chi^2 r^2 \frac{\partial^2 \Phi}{\partial r^2} + (\chi^2 - 2)r \frac{\partial \Phi}{\partial r} \right. \\ &\quad \left. - (\chi^2 - 2)k_\theta^2 r_{out}^2 \Phi + 2ik_\theta r_{out} \left(r \frac{\partial \Psi}{\partial r} - \Psi \right) \right], \\ \sigma_{r\theta}(r, \theta) &= \frac{\mu e^{ik_\theta r_{out} \theta}}{r^2} \left[-r^2 \frac{\partial^2 \Psi}{\partial r^2} + r \frac{\partial \Psi}{\partial r} \right. \\ &\quad \left. - k_\theta^2 r_{out}^2 \Psi + 2ik_\theta r_{out} \left(r \frac{\partial \Phi}{\partial r} - \Phi \right) \right]. \end{aligned} \tag{2.36}$$

where χ is defined as $\chi = c_L / c_T$. Substituting equation (2.35) into equation (2.36) and imposing the boundary conditions, which is equation (2.26) yields 4 homogeneous equations for 4 unknowns A_1 , A_2 , B_1 , and B_2 . Nontrivial solutions to these equations are possible if the determinant of the system matrix D_{ij}

$(i, j = 1, 2, 3, 4)$ of the linear homogeneous equation is set to be zero:

$$\text{Det } |D_{ij}| = 0. \quad (2.37)$$

Each term of D_{ij} is given as [31].

$$\begin{aligned} D_{11} &= \left[J_{M-2} \left(\frac{\xi}{\chi} \right) + J_{M+2} \left(\frac{\xi}{\chi} \right) - 2(\chi^2 - 1) J_M \left(\frac{\xi}{\chi} \right) \right] \chi^{-2}, \\ D_{12} &= i \left[J_{M-2}(\xi) - J_{M+2}(\xi) \right], \\ D_{13} &= \left[Y_{M-2} \left(\frac{\xi}{\chi} \right) + Y_{M+2} \left(\frac{\xi}{\chi} \right) - 2(\chi^2 - 1) Y_M \left(\frac{\xi}{\chi} \right) \right] \chi^{-2}, \\ D_{14} &= i \left[Y_{M-2}(\xi) - Y_{M+2}(\xi) \right], \\ D_{21} &= i \left[J_{M-2} \left(\frac{\xi}{\chi} \right) - J_{M+2} \left(\frac{\xi}{\chi} \right) \right] \chi^{-2}, \\ D_{22} &= - \left[J_{M-2}(\xi) + J_{M+2}(\xi) \right], \\ D_{23} &= i \left[Y_{M-2} \left(\frac{\xi}{\chi} \right) - Y_{M+2} \left(\frac{\xi}{\chi} \right) \right] \chi^{-2}, \\ D_{24} &= - \left[Y_{M-2}(\xi) + Y_{M+2}(\xi) \right], \end{aligned} \quad (2.38)$$

$$\begin{aligned}
D_{31} &= \left[J_{M-2} \left(\frac{\gamma \xi}{\chi} \right) - J_{M+2} \left(\frac{\gamma \xi}{\chi} \right) - 2(\chi^2 - 1) J_M \left(\frac{\gamma \xi}{\chi} \right) \right] \gamma^2 \chi^{-2}, \\
D_{32} &= i \left[J_{M-2}(\gamma \xi) - J_{M+2}(\gamma \xi) \right] \gamma^2, \\
D_{33} &= \left[Y_{M-2} \left(\frac{\gamma \xi}{\chi} \right) + Y_{M+2} \left(\frac{\gamma \xi}{\chi} \right) - 2(\chi^2 - 1) Y_M \left(\frac{\gamma \xi}{\chi} \right) \right] \gamma^2 \chi^{-2}, \\
D_{34} &= i \left[Y_{M-2}(\gamma \xi) - Y_{M+2}(\gamma \xi) \right] \gamma^2, \\
D_{41} &= i \left[J_{M-2} \left(\frac{\gamma \xi}{\chi} \right) - J_{M+2} \left(\frac{\gamma \xi}{\chi} \right) \right] \gamma^2 \chi^{-2}, \\
D_{42} &= - \left[J_{M-2}(\gamma \xi) + J_{M+2}(\gamma \xi) \right] \gamma^2, \\
D_{43} &= i \left[Y_{M-2} \left(\frac{\gamma \xi}{\chi} \right) - Y_{M+2} \left(\frac{\gamma \xi}{\chi} \right) \right] \gamma^2 \chi^{-2}, \\
D_{44} &= - \left[Y_{M-2}(\gamma \xi) + Y_{M+2}(\gamma \xi) \right] \gamma^2.
\end{aligned} \tag{2.38}$$

cont'd

where $\xi = \frac{\omega h}{c_T(1-\gamma)}$, $M = \frac{k_\theta h}{1-\gamma}$, $h = r_{out} - r_{in}$, and $\gamma = \frac{r_{in}}{r_{out}}$.

The dispersion relation is plotted in figure 2.10 for a 2mm-thick aluminum plate while the behaviors of the phase and group velocities as a function of frequency are shown in figure 2.11.

Table 2.1 Selected Bessel functions depending on the range of ω

Range of ω	Functions
$c_L k < \omega$	$J(\alpha r), Y(\alpha r), J(\beta r), Y(\beta r)$
$c_T k < \omega < c_L k$	$I(\alpha_1 r), K(\alpha_1 r), J(\beta r), Y(\beta r)$
$\omega < c_T k$	$I(\alpha_1 r), K(\alpha_1 r), I(\beta_1 r), K(\beta_1 r)$

Table 2.2 λ value selection criterion according to the range of each frequency

Interval	Values
$c_L k < \omega$	$\lambda_1 = 1, \lambda_2 = 1$
$c_T k < \omega < c_L k$	$\lambda_1 = -1, \lambda_2 = 1$
$\omega < c_T k$	$\lambda_1 = -1, \lambda_2 = -1$

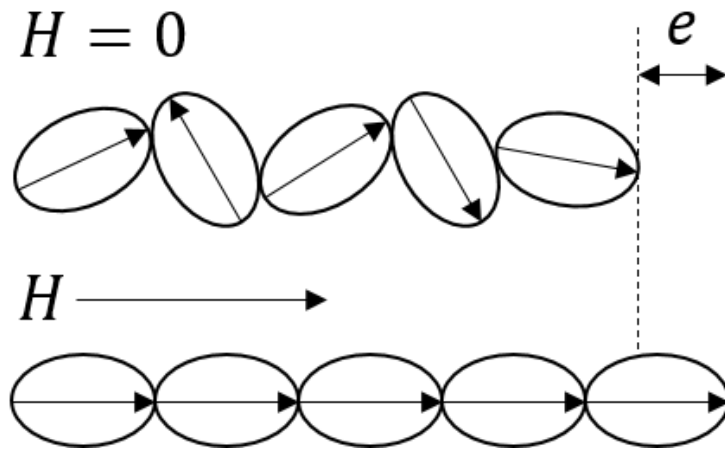


Fig. 2.1 The inside of a ferromagnetic body rearranged by a magnetic field.

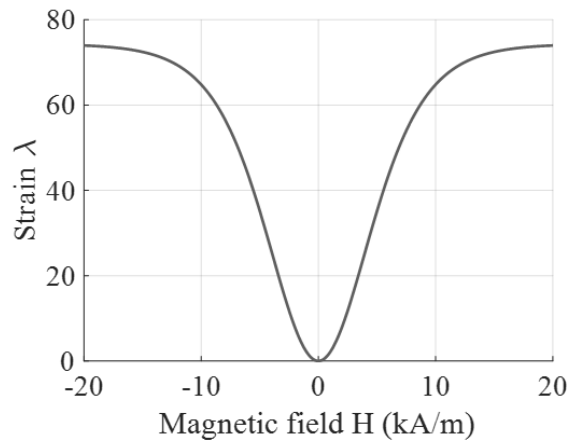


Fig. 2.2 Nonlinear magnetostriction curve of a magnetostrictive material (HiperCo 50A).

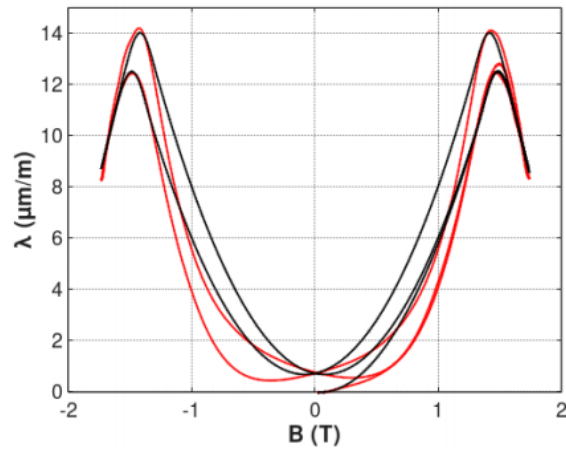


Fig. 2.3 magnetization curve of a magnetostrictive material (pure nickel) with a hysteresis property [24]. The red line denotes experimental results and black line denotes simulation results.

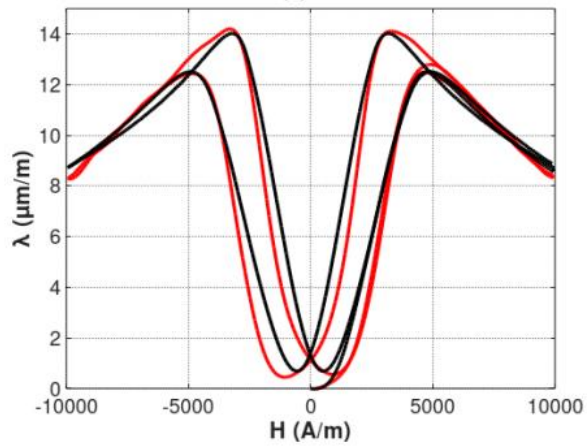


Fig. 2.4 magnetostriction curve of a magnetostrictive material (pure nickel) with a hysteresis property [24]. The red line denotes experimental results and black line denotes simulation results.

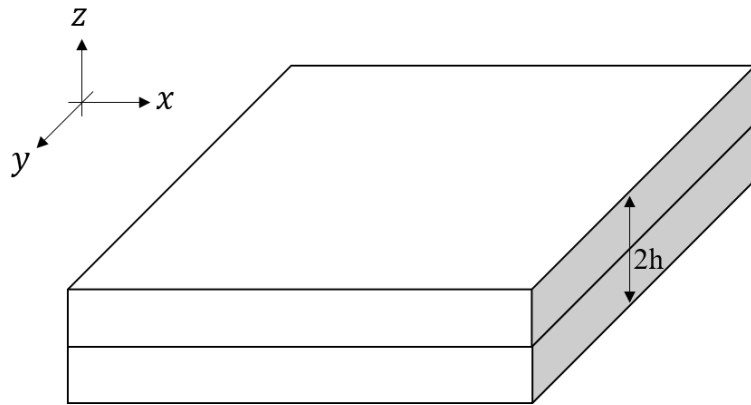


Fig. 2.5 A plate of thickness $2h$. It is assumed to be infinitely long in the y direction.

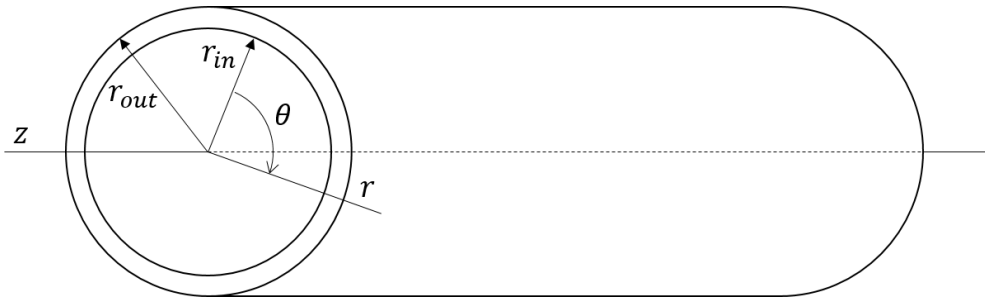


Fig. 2.6 Coordinates for an infinitely long hollow circular cylinder.

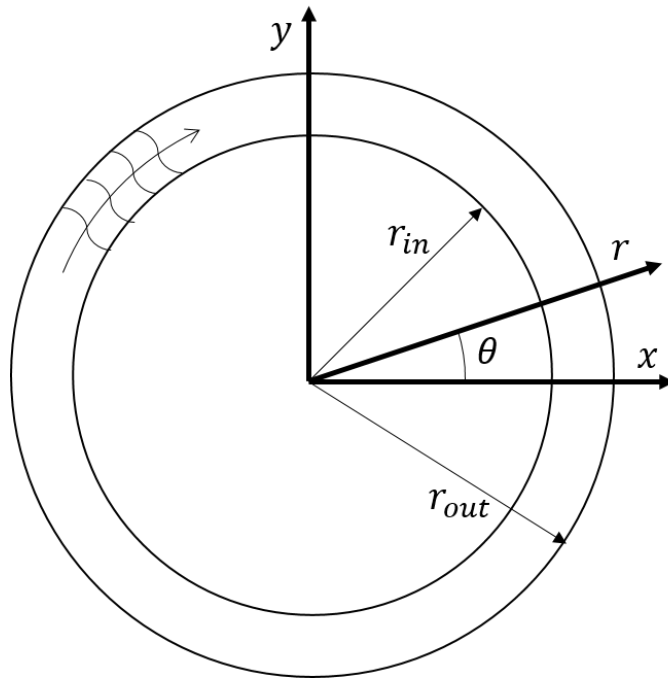


Fig. 2.7 The geometry of a hollow cylinder with inner and outer radii, r_{in} and r_{out} .

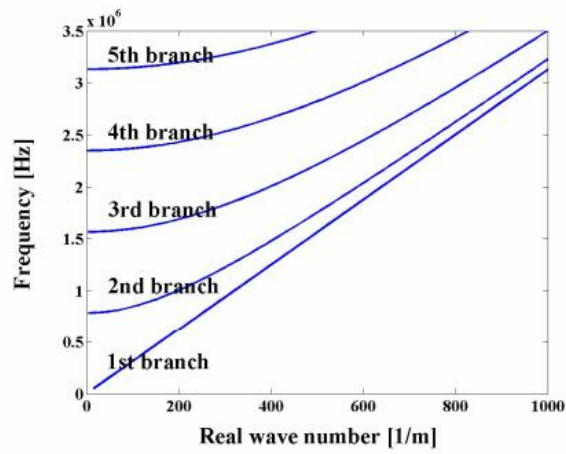


Fig. 2.8 Dispersion curve (Relation between frequency and wave number) for torsional waves in a hollow aluminum cylinder with an outer diameter of 25 mm and a thickness of 2 mm.

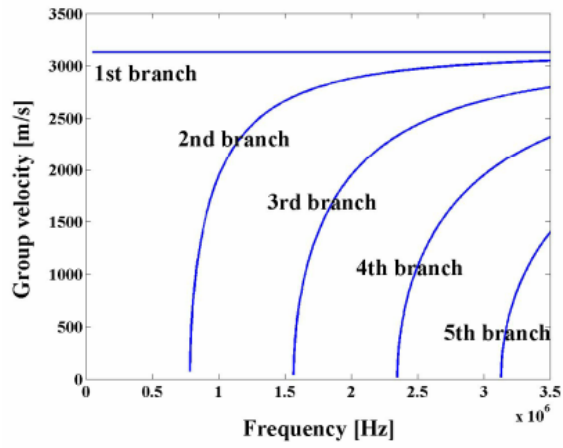


Fig. 2.9 Dispersion curve (Relation between group velocity and frequency) for torsional waves in a hollow aluminum cylinder with an outer diameter of 25 mm and a thickness of 2 mm.

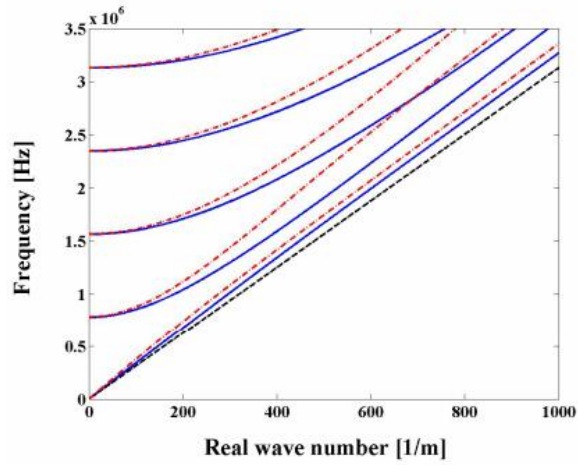


Fig. 2.10 Dispersion curve (Relation between frequency and wave number) for circumferential SH waves in a hollow aluminum cylinder with a different outer diameters 12 mm and 25 mm which have same thickness of 2 mm.

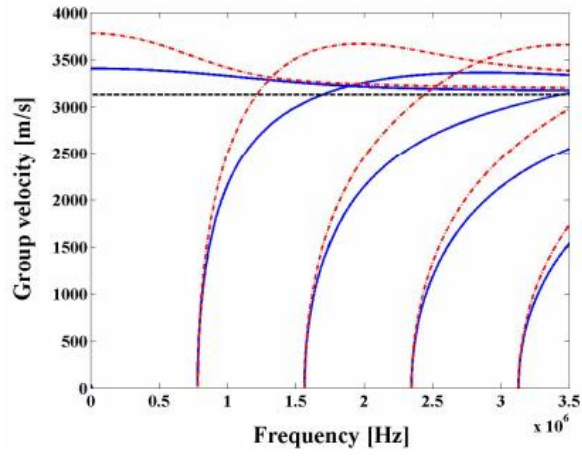


Fig. 2.11 Dispersion curve (Relation between group velocity and frequency) for circumferential SH waves in a hollow aluminum cylinder with a different outer diameters 12 mm and 25 mm which have same thickness of 2 mm.

CHAPTER 3.

MAGNETOSTRICTIVE PATCH TRANSDUCER FOR TORSIONAL ELASTIC WAVES

As mentioned in Chapter 1, there were efforts to express the magnetostriction phenomenon in various ways. The simplest of all models is the linear equation and the magnetostriction equation is also linearly expressed through several assumptions.

In this chapter, we introduce the linear equations for these magnetostriction phenomenon. Numerous studies [36-42] have used this equations, and although some conditions are required, they quite well represent the tendency of magnetostriction phenomenon. Although accurate physical quantities can not be obtained, it is possible to analyze trends, so we try to optimize some design parameters of magnetostrictive patch transducers through the corresponding equations. Furthermore, we will make relative comparisons with previously validated strain gages with optimized magnetostrictive patch transducers. Although the approach through linear equations allows a trend comparable to frequency or intensity only, the results will show the potential for quantification of magnetostrictive patch transducers.

In addition, the magnetostrictive patch transducer used in this study is described in detail before the magnetostriction equations.

3.1 Configuration of the magnetostrictive patch transducer

In this section, the fundamentals of the proposed magnetostrictive patch transducer will be presented. Then a finite element model of the magnetostrictive patch transducer that is installed on a solid shaft will be developed and used for a series of numerical studies. Based on the studies, the optimal number and size of patches will be determined for the proposed magnetostrictive patch transducer.

Figure. 3.2 schematically shows the configuration of the proposed magnetostrictive patch transducer installed on a solid shaft. Magnetostrictive patches are segmented and they are tightly bonded onto the shaft surface along the circumference. The cross sectional view of the magnetostrictive patch transducer can be found in figure 3.3. Here, the number of patches (N_p) is temporarily chosen to be 6. In the space between the two adjacent patches, permanent magnets are placed to magnetize the patches. In the magnetostrictive patch transducer configuration in figure 3.2, the magnets provide a bias static magnetic field in the patches along the circumferential direction. A solenoid coil is wound around the system of patches and magnets

to detect the radial dynamic magnetic field induced by torsional vibrations of the shaft. (The detection mechanism will be explained later). Because there is no physical contact between the coil and the magnets, the magnetostrictive patch transducer's can be used to measure torsional vibrations of a rotating shaft without direct wiring.

3.2 Simplified analysis of magnetoelastic effect using magnetostriction equation

In this section, the fundamentals of the proposed magnetostrictive patch transducer will be presented. Then a finite element model of the magnetostrictive patch transducer that is installed on a solid shaft will be developed and used for a series of numerical studies. Based on the studies, the optimal number and size of patches will be determined for the proposed magnetostrictive patch transducer.

3.2.1 Linear magnetostriction equation

The magnetostriction phenomenon can be interpreted formally through the magnetostriction constitutive equations. In general, the magnetostrictive constitutive

equations are nonlinear and can be expressed as [31].

$$\varepsilon = f(\sigma, \mathbf{H}) \quad (3.1)$$

$$\mathbf{B} = g(\sigma, \mathbf{H}) \quad (3.2)$$

Where ε and σ are the strain and stress tensor, respectively, and \mathbf{B} and \mathbf{H} are the magnetic flux density and the magnetic field tensor, respectively. Equation (3.1) expresses the strain change due to the magnetic field, that is, the Joule effect described above, and equation (3.2) means the Villari effect, which is the inverse of the Joule effect.

The major reason that equations (3.1) and (3.2) have nonlinearity is that the magnetostriction phenomenon has hysteresis. Although the degree of hysteresis is different for each material and various studies have been carried out to define it, it is common to denote the magnetostriction phenomenon by ignoring the influence of hysteresis through several assumptions. Hysteresis will be discussed later.

Magnetostrictive phenomenon exhibit similar behavior to piezoelectric phenomenon, and macroscopically, they can be seen as the difference between magnetic and electrical elements. Therefore, the constitutive equation for the magnetostrictive phenomenon can be approximated to the constitutive equation in the piezoelectric

phenomenon.

$$\boldsymbol{\varepsilon} = \mathbf{E}\boldsymbol{\sigma} + \mathbf{d}^T\mathbf{H} \quad (3.3)$$

$$\mathbf{B} = \mathbf{d}\boldsymbol{\sigma} + \mu\mathbf{H} \quad (3.4)$$

In equations (3.3) and (3.4), \mathbf{E} represents the elastic compliance matrix (6x6), and \mathbf{d} and μ represent the magneto-mechanical coupling matrix (6x3) and the magnetic permeability matrix (3x3), respectively. Equation (3.3) and (3.4) come from the linear constitutive equation of piezoelectric phenomenon and are satisfactory when the magnetostriction phenomenon is linear. The magnitude of the static magnetic field $\bar{\mathbf{H}}$ must be very large compared to the dynamic magnetic field $\tilde{\mathbf{H}}$ applied for the magnetostriction phenomenon to be linear ($\bar{\mathbf{H}} \gg \tilde{\mathbf{H}}$). In this case, it oscillates about the $\tilde{\mathbf{H}}$ region around the $\bar{\mathbf{H}}$ section in the magnetostriction curve, which is a partly linear position in the nonlinear magnetostriction curve. In the case of a transducer, the linear characteristic is very important, and the transducer using the magnetostriction phenomenon is mainly designed to have a linear characteristic as described above.

If the dynamic magnetic field is smaller than that of the static magnetic field as in the above assumption, the strain can be divided into the strain $\bar{\boldsymbol{\varepsilon}}$ due to the static field and the strain $\tilde{\boldsymbol{\varepsilon}}$ due to the dynamic field. This applies equally to stress $\boldsymbol{\sigma}$

and magnetic flux density \mathbf{B} .

$$\begin{aligned}\mathbf{H} &= \bar{\mathbf{H}} + \tilde{\mathbf{H}} \\ \boldsymbol{\varepsilon} &= \bar{\boldsymbol{\varepsilon}} + \tilde{\boldsymbol{\varepsilon}}\end{aligned}\tag{3.5}$$

First, the magnetostriction by the static magnetic field can be expressed as follows.

$$(3.6)$$

$$\bar{\mathbf{B}} = \mathbf{d}\bar{\boldsymbol{\sigma}} + \mu\bar{\mathbf{H}}\tag{3.7}$$

Considering the above-mentioned linear assumption, assuming that the material is elastically isotropic, the $\bar{\boldsymbol{\varepsilon}} = \mathbf{E}\bar{\boldsymbol{\sigma}} + \mathbf{d}^T\bar{\mathbf{H}}$ change of the magnetization direction strain due to the magnetostriction phenomenon is proportional to the product of the applied field magnitude and the magnetization direction component of the magneto-mechanical coupling matrix \mathbf{d} . If the magnetization direction component is d_{11} when satisfying continuity ($\varepsilon_1 + \varepsilon_2 + \varepsilon_3 = 0$) and volume conservation, the magneto-mechanical coupling matrix can be defined as

$$\mathbf{d} = \begin{bmatrix} d_{11} & -\frac{1}{2}d_{11} & -\frac{1}{2}d_{11} \\ -\frac{1}{2}d_{11} & d_{11} & -\frac{1}{2}d_{11} \\ -\frac{1}{2}d_{11} & -\frac{1}{2}d_{11} & d_{11} \\ 0 & 0 & 0 \\ 0 & 0 & 0 \\ 0 & 0 & 0 \end{bmatrix} \quad (3.8)$$

However, as mentioned above, the change due to the static magnetic field is affected by the non-linearity of the magnetostriction phenomenon due to the large variation. Therefore, the effectiveness of the linear equations (3.6) and (3.7) is generally low. The constitutive equations of the dynamic magnetic field can be expressed as follows,

$$\tilde{\boldsymbol{\varepsilon}} = \mathbf{E}\tilde{\boldsymbol{\sigma}} + \mathbf{d}^T\tilde{\mathbf{H}} \quad (3.9)$$

$$\tilde{\mathbf{B}} = \mathbf{d}\tilde{\boldsymbol{\sigma}} + \mu\tilde{\mathbf{H}} \quad (3.10)$$

Generally, in order to establish a linear equation, a static magnetic field and a dynamic magnetic field exist at the same time and $\bar{\mathbf{H}} \gg \tilde{\mathbf{H}}$ must be satisfied. In dynamic, the composition of the magneto-mechanical coupling matrix is different from that of static, and when the magnetization direction is x_1 direction in

$\{x_1, x_2, x_3\}$ coordinate, it can be expressed as [43],

$$\mathbf{d} = \begin{bmatrix} d_{11} & 0 & 0 \\ -\frac{1}{2}d_{11} & 0 & 0 \\ -\frac{1}{2}d_{11} & 0 & 0 \\ 0 & 0 & 0 \\ 0 & 0 & d_{35} \\ 0 & d_{35} & 0 \end{bmatrix} \quad (3.11)$$

Unlike static, the magneto-mechanical coupling matrix is different because the isotropic material influenced by the dynamic magnetic field shows anisotropic behavior due to the applied static magnetic field. Equation (3.11) implies that the material is transverse isotropic and the isotropic surface is perpendicular to the magnetization axis. The \mathbf{d} matrix is represented by two terms, d_{11} and d_{35} , which express different physical phenomena. One of them, d_{11} represents a normal strain component due to a dynamic magnetic field generated in the direction of magnetization by a static magnetic field.

$$d_{11} = \left(\frac{\partial \varepsilon_1}{\partial H_1} \right) \Big|_{\bar{H}_1} \quad (3.12)$$

This means the instantaneous slope at the position corresponding to the static magnetic field \bar{H}_1 in the magnetostriction curve. In this case, the direction of the static and dynamic magnetic fields is parallel, and the intensity of the whole magnetic field changes in the same direction. As a result, d_{11} represents the modulation of the intensity of the bias magnetic field.

On the other hand, the case where the static magnetic field and the dynamic magnetic field are perpendicular can be considered. When the premise $\bar{\mathbf{H}} \gg \tilde{\mathbf{H}}$ is the same, $\mathbf{H} = \bar{\mathbf{H}} + \tilde{\mathbf{H}}$ is the same as the whole, but the direction is slightly inclined. In other words, d_{35} represents the dynamic change in the bias magnetic field direction, and *Ogi and Hirao* [44] define d_{35} as the total magnetostrictive strain ε by adapting the coordinate transformation in the oblique direction.

$$d_{35} = \frac{3\varepsilon}{\bar{H}_1} \quad (3.13)$$

And this is proportional to the mean slope in the static magnetic field applied in the magnetostriction curve.

As shown in figure. 3.1, when the magnetostriction curve is measured, all the magneto-mechanical coupling coefficients can be calculated. This means that the

magnetostrictive properties of materials used in the design of magnetostrictive transducers are important, and the performance of the transducers can be greatly changed by the applied static magnetic field.

3.2.2 Effect of static magnetic field on the performance of magnetostrictive patch transducer

To explain the measurement principle of magnetostrictive patch transducer the Villari effect [28] is considered in terms of a linear magnetostrictive equation as follows [43]:

$$B = \mu H + d_p \sigma \quad (3.14)$$

where B and H are the induced magnetic flux density and the magnetic field, respectively. In the magnetostrictive patch transducer case, H is regarded as an applied static (time-independent) bias magnetic field to the patch. The symbol σ denotes the mechanical stress and μ and d_p represent the permeability under constant stress and the shear component of the piezomagnetic coefficient of the patches, respectively. The value of d_p , which depends on H , critically affects the sensing performance of the magnetostrictive patch transducer. Therefore, N_p

should be optimized to provide optimal H to the patches.

Because the patches are bonded onto the surface of a shaft, shaft vibrations develop torsional shear stress in the patches. By the inversed Wiedemann effect [30], the dynamic shear stress developed in the patches under the circumferentially biased magnetic field induces the dynamic magnetic field along the axial direction. The inverse Wiedemann effect may be viewed as a special case of the Villari effect. The solenoid encircling the patches can detect the radial magnetic induction, which is finally measured as an electromotive force $V_{\text{MTVS}}(t)$ according to the well-known Faraday-Lenz [45] law as

$$V_{\text{MTVS}}(t) = -N \frac{\partial \Phi}{\partial t} = -N \frac{\partial \phi}{\partial t} = -N \frac{\partial}{\partial t} \int_A B dA \quad (3.15)$$

where Φ is the magnetic flux encircled by a single line coil and N is the number of turns. The symbols ϕ and t denote the total magnetic flux and time, respectively, while B and A , the magnetic flux by the induction and the cross-sectional area of all the patches, respectively. Substituting equation (3.14) into (3.15) yields the relation between the voltage output $V_{\text{MTVS}}(t)$ and the shear strain $\gamma(t)$ on the surface of a shaft where the strain distribution in the patches is assumed to be the same as the stress distribution on the surface of a shaft [46]:

$$V_{\text{MTVS}}(t) = -N \frac{\partial}{\partial t} \int_A d_p \sigma dA = -Nd_p G \int_A \frac{\partial \gamma(t)}{\partial t} dA \quad (3.16)$$

where G denotes the shear modulus. Equation (3.16) shows that the measured signal by the magnetostrictive patch transducer is proportional to the time derivative of strain.

Simulation for Selecting the Optimal Number of Patches

For the magnetostrictive patch transducer, N_p should carefully be determined based on numerical simulations for enhancing the sensing efficiency. As reported by the previous works [47-51], the applied static magnetic field strength highly affects the value of the shear component of piezomagnetic coefficient (d_p) which critically affects the sensitivity of the sensors. This phenomenon occurs due to nonlinearity in the magnetostriction curve of the magnetostrictive patch material, which relates the applied magnetic field strength and strain (magnetostriction). In case of the proposed magnetostrictive patch transducer, the length of each patch segment (L_p) varies with N_p because the diameter of a shaft is assumed to be fixed and also the size and strength of magnets are pre-selected. Accordingly, the applied static magnetic strength along the length of each patch, in turn, the value of d_p varies with N_p .

The procedure to calculate d_p for a specific distribution of static magnetic strength was discussed in [52-56]. As a result of the calculation, the value of d_p in equation 3.16 is defined as [43]:

$$d_p = 3 \frac{\varepsilon_{MS}}{H} \quad (3.17)$$

where H and ε_{MS} represent applied static magnetic strength and magnetostriction of the patch material, HiperCo 50A [26], in the present investigation. Although not explicitly shown here, the nonlinear magnetic properties of the patches [57] were included in the present analysis.

To determine H and d_p , the finite element simulation was performed by using COMSOL Multiphysics 4.3a [58] for the model shown in the left side of figure 3.3. Table 3.1 shows the specification of the used magnetostrictive patch transducer for the present simulations. The induced magnetic flux is shown in the right side of figure 3.3. Figure 3.4 plots the d_p distribution along the patch for the different N_p values ($R = 25$ mm). d_p^{Nom} represent the normalized mean values of d_p over the patch and they are defined as:

$$d_p^{\text{Norm}} = \frac{d_p|_{N_p=n}}{d_p|_{N_p=3}} \quad (n = 1, 2, \dots, 5). \quad (3.18)$$

These values are plotted in the figure 3.5 simulation result. For the case considered in figure 3.3, the largest d_p , equivalently, the highest sensitivity of the magnetostrictive patch transducer was obtained when $N_p = 3$.

3.3 Relative quantification with qualified strain gauge

As a preliminary study before applying the magnetostrictive patch transducer to measure vibrations of a rotating propulsion shaft in a ship, experiments were carried out first with stationary solid shafts. With the experiments, the validity of the simulation result in figure 3.5 is checked and how accurately torsional modal testing can be performed with the proposed sensor is also investigated.

3.3.1 Experimental setup

The experimental setup is shown in figure 3.6. Because the same magnetostrictive patch transducer configuration can also be used as a transmitter (due to the Widemann effect) [30]), two magnetostrictive patch transducer's were used for experiments, one as an exciter and the other as a sensor. The patches were tightly

bonded onto the surface of the 3 m long shaft by epoxy resin (DP460, 3M, St. Paul, MN) and the distance between two magnetostrictive patch transducer was 300 mm. The specifications of the magnetostrictive patch transducers are listed in Table 1. For instance, the patch is 50 mm (along the circumferential direction) \times 25 mm (along the axial direction). We employed the magnetostrictive patch transducer transmitter because it can effectively excite pure torsional vibrations of a shaft.

The followings are the detailed procedure of the experiment. The generated rectangular pulse of 120 μ s duration by a function generator (33250A, Agilent Technologies, Santa Clara, CA) was sent to a power amplifier (TECHRON 7560, AE Techron, IN). The input current to the solenoid of the exciter was shown in the top figure of figure 3.7. The torsional vibration was excited by the magnetostrictive patch transducer exciter and the sensing magnetostrictive patch transducer measured torsional vibration as a voltage output through the solenoid. The output signal was amplified by a preamplifier (SR560, Stanford Research Systems, Sunnyvale, CA) before recorded by an oscilloscope (WaveRunner 620Zi, LeCroy, Chestnut Ridge, NY). Because of the free boundaries of the shaft, the reflected signals were accumulated as shown in the bottom figure of figure 3.7. The peak-to-peak voltage value is denoted by V_{MTVS}^{PP} . The diameter of the coil was 70 mm, which was slightly larger than that ($2R = 50$ mm) of the shaft. The coil connector was specially fabricated to be directly installed on a shaft. In addition, the PCB circuit in the connector was designed for serial connection of the IDC cables considering AC

current flow. The value of V_{MTVS}^{PP} extracted from the measured voltage signals for different N_p values. The normalized V_{MTVS}^{PP} values are defined as V_{MTVS}^{Norm} and they can be represented as:

$$V_{MTVS}^{Norm} = \frac{V_{MTVS}^{PP} \Big|_{N_p=n}}{V_{MTVS}^{PP} \Big|_{N_p=3}} \quad (n = 1, 2, \dots, 5). \quad (3.19)$$

These values are compared with the simulation result in figure 3.5 as an experimental result. It verifies the validity of the simulation results performed in the previous section. It is clear that both the simulation and experiment results predict the same finding that the highest sensitivity is obtained if $N_p = 3$ for the shaft of the given diameter.

3.3.2 Experimental validation

As a means to demonstrate the sensor performance of magnetostrictive patch transducer's further, we performed experimental torsional modal testing for the same shaft used in the previous subsection. In order to minimize the influence of the patches to the modal testing, the patch was attached to only one position. After the end of each experiment, the patch and adhesive (epoxy) were removed to restore the

state of the shaft before experiment. Following the standard modal testing procedure (by using the same magnetostrictive patch transducer exciter and sensor used above with the excitation and sensing locations shown in figure. 3.9), the results in Fig. 8 and in table 3.2 are obtained for three shafts of different length (L_s) and compared with the theoretical results [59]. The extracted eigenfrequencies from figure 3.8, summarized in table 2, agree well with the theoretical eigenfrequencies. Figure 3.9 also confirms that the experimentally determined torsional strain eigenmodes by using magnetostrictive patch transducer are in good agreement with the theoretical ones.

Because the magnetostrictive patch transducer is aimed to be used as an alternative sensor to a commonly-used strain gauge system, the measured signals by the magnetostrictive patch transducer and a strain gauge system need to be compared quantitatively and qualitatively. To facilitate the comparison, a test system sketched in figure 3.12 was used. For the test, a shaft (radius = 25 mm) made of AISI 1045, which is the same material as that of the propulsion shaft of a ship to be tested, was used. It was excited by a hydraulic exciter (Xcite 1100-6-FT System, Xcite Systems Corporation, Cincinnati, OH) applied to the end of the moment arm illustrated in figure 3.12. The other end was fixed. With this excitation scheme, sufficiently large torsional vibrations which can be sensed by a commercial strain gauge system were generated. For the experiment, both an magnetostrictive patch transducer and the strain gauge system mentioned in Introduction and in [60-65] were installed and

torsional moments were applied by the exciter with a wide range of input voltages and excitation frequencies.

Figure 3.13 compares the time signals measured by the two sensors and their phases and FFT results where the input signals were 20 cycles of a sinusoidal wave centered at 20 Hz. Both results clearly show the sinusoidal behavior but the amplitude and, in particular, the phases of the two signals are different. The main reason for the difference is that the strain gauge measures strain directly while the magnetostrictive patch transducer measures the time derivative of strain, strain rate. To convert measured strain rate signals by the magnetostrictive patch transducer to strain gauge signals, we considered the followings. First, the measured voltage signal V_{SG} , which is proportional to strain, by the strain gauge may be simply written as

$$V_{SG} = \kappa\gamma(t) = \alpha e^{i2\pi ft} \quad (3.20)$$

where f , t and γ denote frequency, time and torsional strain with $i = \sqrt{-1}$ and κ , a calibration constant. The symbol α denotes the magnitude of the signal. On the other hand, from equation (3.14), the voltage by the magnetostrictive patch transducer (V_{MTVS}) can be written as, under the harmonic input in equation (3.20),

$$V_{\text{MTVS}} = \eta \frac{d}{dt} \gamma(t) = \frac{\eta}{\kappa} (i2\pi f) \alpha e^{i2\pi ft} \quad (3.21)$$

where η is a calibration constant. Comparing equation (3.20) and (3.21), the following relation is obtained

$$\tilde{V}_{\text{SG}}^{\text{Mag}} = c \tilde{V}_{\text{MTVS}}^{\text{Mag}} / f \quad (3.22)$$

where $\tilde{V}_{\text{SG}}^{\text{Mag}}$ and $\tilde{V}_{\text{MTVS}}^{\text{Mag}}$ denote the magnitudes of the measured signals by the strain gauge and the magnetostrictive patch transducer, respectively. c is a calibration constant. In equation (3.22), the tilde symbols are used to emphasize that the calibration is performed. Equation (3.22) shows that if the measured signal by the magnetostrictive patch transducer is divided by f in the frequency domain, the strain signal, as measured by the strain gauge system, can be recovered. Figure 3.14(a) shows the first peak magnitude of the FFT results of the magnetostrictive patch transducer signals according to varying frequencies. The frequency-adjusted magnetostrictive patch transducer results by using equation (3.22) are compared in figure 3.14(b) with those directly measured by the strain gauge. By doing so, the measured signals by the magnetostrictive patch transducer are shown to be in good agreement with the strain gauge signals. In addition, the wiggly behavior of the measured signals is clearly observed for frequencies below about 20 Hz from figure

3.14(c), which is the detailed plot of the dotted rectangular area in figure 3.14(b). This is because the used hydraulic excitation system has some instability for frequencies below about 20 Hz. Nevertheless, the adjusted signal by the magnetostrictive patch transducer is almost the same with that of the strain gauge in this frequency range. Based on the results in figure 3.14, accordingly, it can be concluded that the magnetostrictive patch transducer can also cover wide frequency range as well including the low frequency range because the strain gauge system is regarded as a reference system in this study as mentioned in Introduction. This indicates that as long as the measured signal by the magnetostrictive patch transducer is frequency-adjusted by equation (3.22), the magnetostrictive patch transducer accurately predicts strain signals. Therefore, equation (3.22) can be used to find the strain spectrum from the measured signals by the magnetostrictive patch transducer when it is used for onsite applications.

Finally, the linearity of the magnetostrictive patch transducer sensor is also checked by increasing input voltage. The results in figure 3.15 show that as the input voltage increases linearly, the magnetostrictive patch transducer signal also increases linearly except at the excitation frequency (f) equal to 10 Hz. The slight nonlinear behavior for 10 Hz is due to the difficulty in low-frequency excitation as mentioned above. Table 3.3 lists some specifications of the magnetostrictive patch transducer found from the results in figure 3.15. The signal-to-noise ratio of the magnetostrictive patch transducer is compared with that of the strain gauge and the

sensitivity of the magnetostrictive patch transducer is also calculated using the measured mechanical strain as an input parameter.

Table 3.1 Material property and geometry of magnetostrictive patch transducer

	Material	Dimension
Patch	Hiperco 50HS	$50 \times 25 \times 0.15 \text{ mm}^3$ (for $N_p = 3$)
Shaft	AISI 4140	$\phi \text{ 50 mm}$
Magnets	NdFeB	$25 \times 3 \times 3 \text{ mm}^3$

Table 3.2 Comparison between theoretical and experimental natural frequencies of torsional vibration

Mode	1 m			2 m			3 m		
	f_n^{TH} [Hz]	f_n^{EXP} [Hz]	Error [%]	f_n^{TH} [Hz]	f_n^{EXP} [Hz]	Error [%]	f_n^{TH} [Hz]	f_n^{EXP} [Hz]	Error [%]
1	1541	1552	0.71	770	776	0.78	513	521	1.56
2	3082	3039	0.36	1541	1552	0.71	1027	1042	1.46
3	4623	4623	0.00	2311	2317	0.26	1541	1563	1.43
4	6164	6175	0.18	3082	3093	0.36	2055	2084	1.41
5	7705	7738	0.43	3852	3869	0.44	2568	2583	0.58
6	9246	9268	0.24	4623	4634	0.24	3082	3104	0.74

Table 3.3 Specifications of the magnetostrictive patch transducer system

f [Hz]	SNR [dB]		Sensitivity [V/strain] Strain gauge
	MTVS		
10	20.45	22.04	1.56
20	19.10	19.28	3.31
30	15.14	17.33	4.89

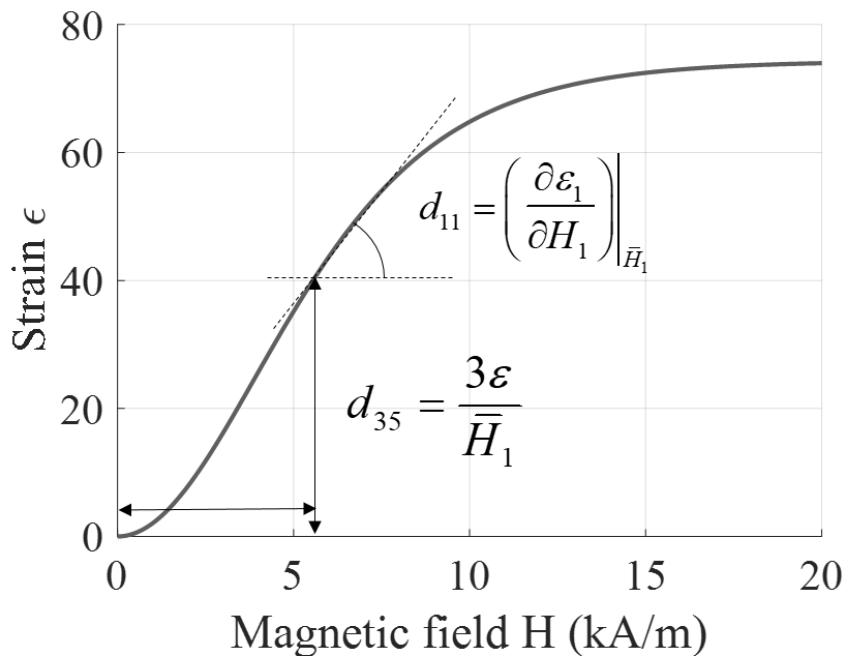


Fig. 3.1 Coupling constants d_{11} , d_{35} calculated by the magnetostriction curve

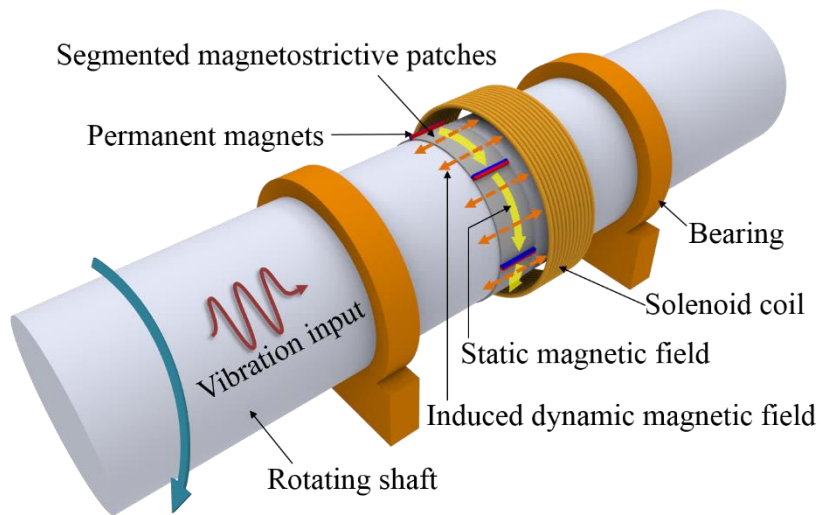


Fig. 3.2 Schematic configuration of the proposed torsional magnetostrictive patch transducer for measuring torsional vibrations in a rotating shaft.

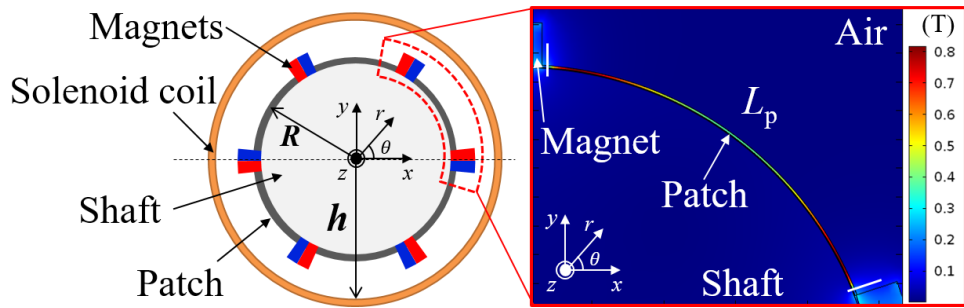


Fig. 3.3 A cross sectional view of the magnetostrictive patch transducer (left figure) and the magnetic induction in the patch (right figure) for $N_p = 6$ and $R = 25$ mm, calculated by the two-dimensional magnetostatic finite element model.

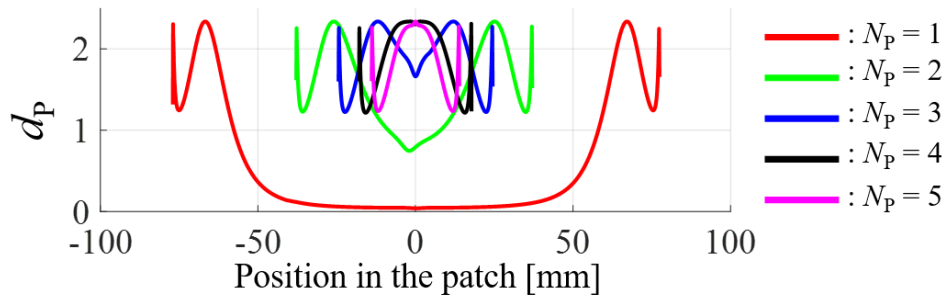


Fig. 3.4 The d_p distribution in the patch for varying N_p values. (The abscissa presents the position in a single patch where 0 represents the patch center.)

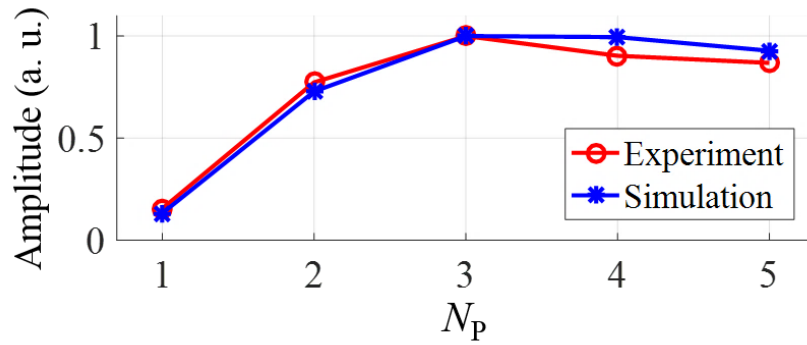


Fig. 3.5 The normalized mean values of d_p in the patch (d_p^{Norm}) (blue line) and the normalized peak-to-peak voltages of the transducer signals ($V_{\text{MTVS}}^{\text{Norm}}$) (red line) for varying N_p values.

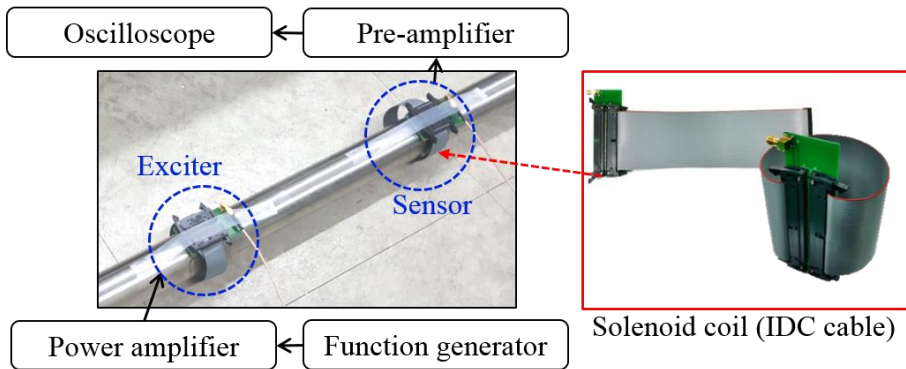


Fig. 3.6 Experimental setup for torsional vibration transduction in a stationary solid shaft of $R = 25$ mm. Magnetostrictive patch transducers are used both for vibration excitation and measurement. IDC cables (64 turns) are used as the solenoid coils of the transducer.

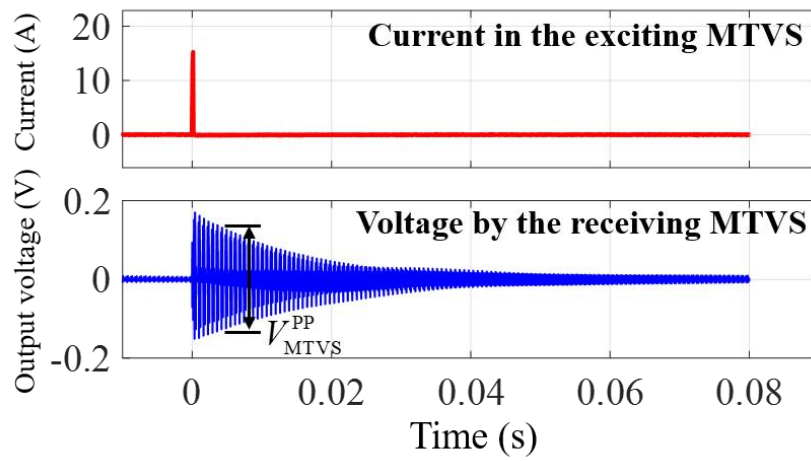


Fig. 3.7 The time signals of the input current in the exciting magnetostrictive patch transducer and the induced voltage by the receiving magnetostrictive patch transducer.

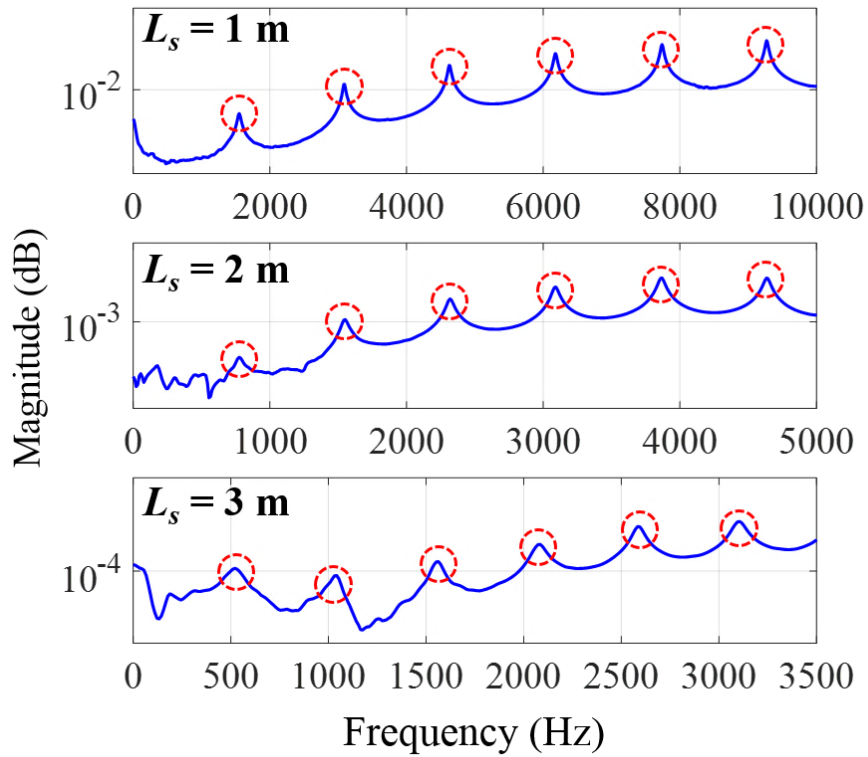


Fig. 3.8 Experimentally obtained torsional frequency response functions of the shafts of different lengths (L_s) by using the proposed transducer both as an exciter and a sensor. (The red dotted circles are used to indicate the peaks corresponding the eigenfrequencies.)

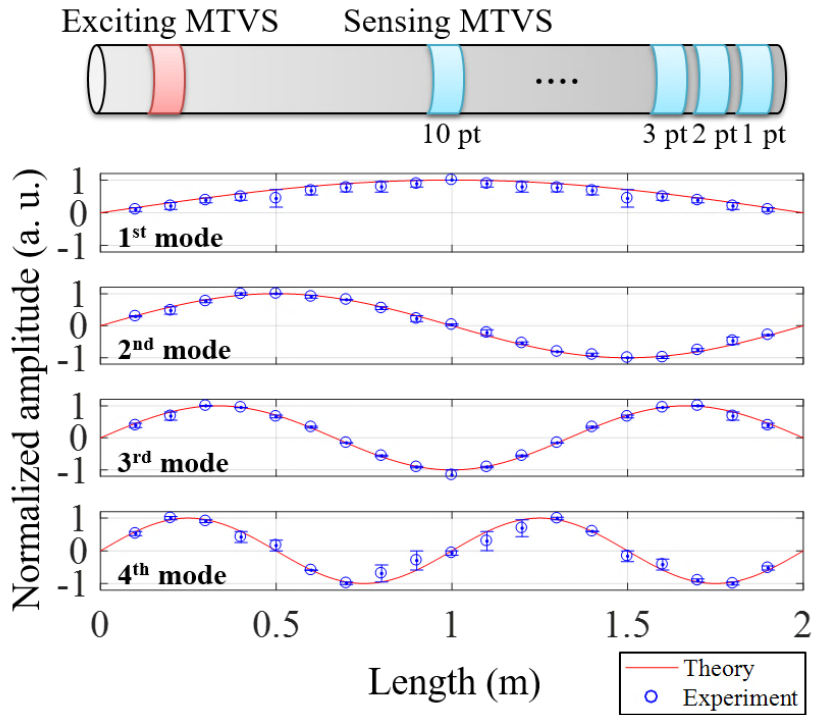


Fig. 3.9 Comparison of experimentally obtained torsional strain eigenmodes by using the transducers and the theoretical ones for a shaft of $L_s=2$ m. The error rates on the node points of each mode are about less 5%.

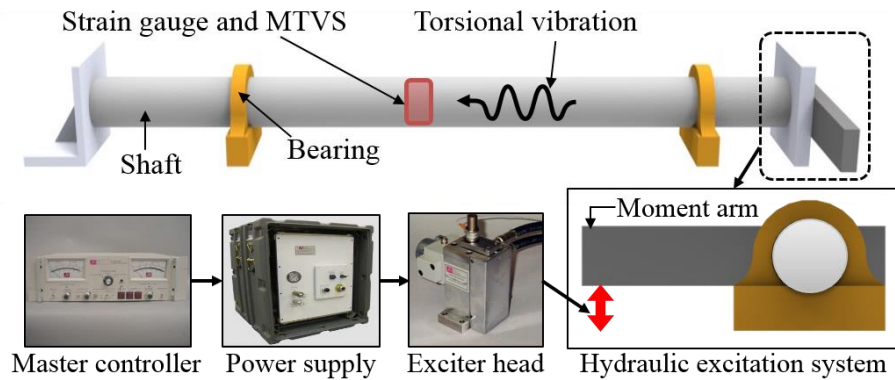


Fig. 3.10 The experimental setup used to compare the signals measured by the MTVS and the strain gauge system with a telemetry unit. The hydraulic exciting system was used to generate torsional vibrations.

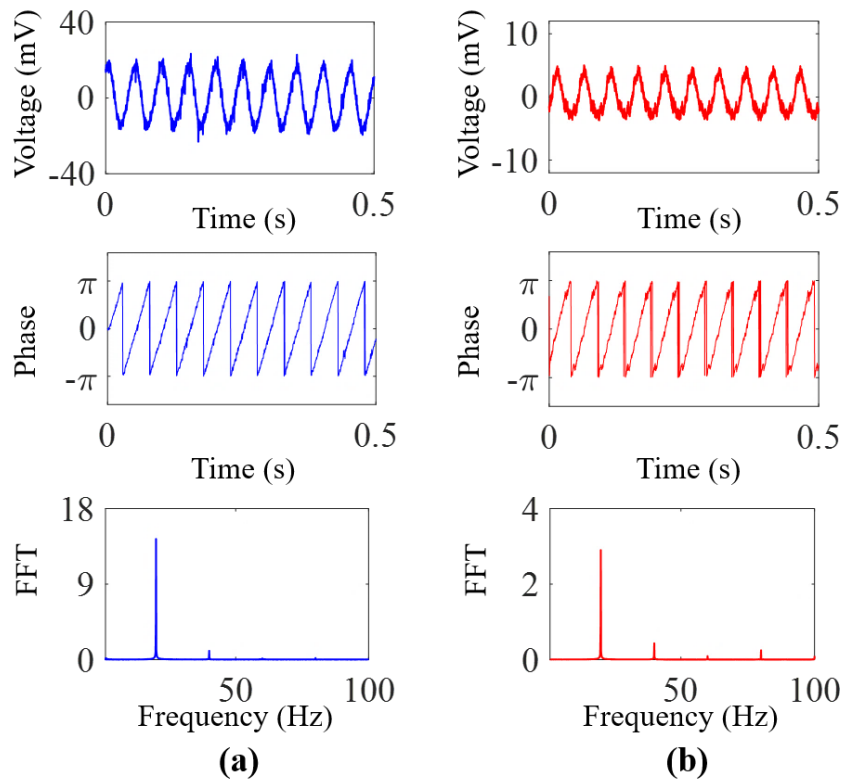


Fig. 3.11 The measured time signals, phases and their FFT results by (a) the strain gauge and (b) the magnetostrictive patch transducer installed on a stationary shaft excited at 20 Hz.

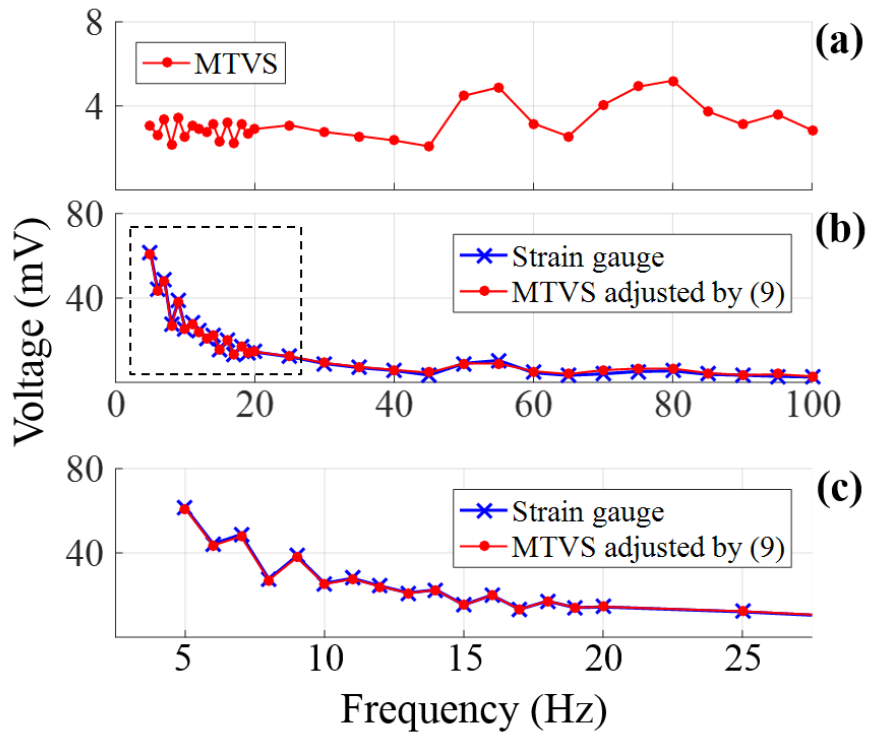


Fig. 3.12 (a) The amplitudes of the measured signals by the magnetostrictive patch transducer at different excitation frequencies. (b) The comparison of the frequency-adjusted signals measured by the magnetostrictive patch transducer through (9) and the signals measured by the strain gauge. (c) The detailed plot of the dotted rectangular area in (b).

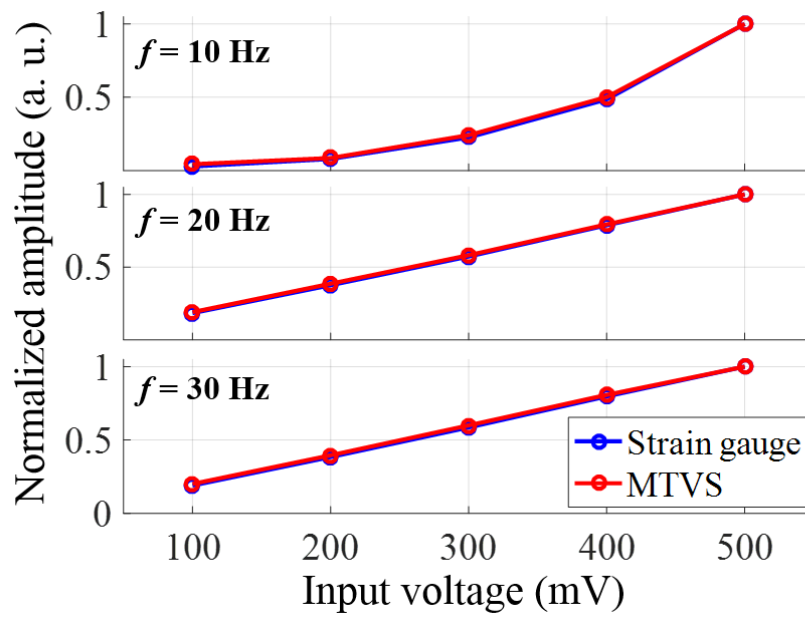


Fig. 3.13 The measured signal amplitudes according to varying input voltages for three different excitation frequencies of 10, 20 and 30 Hz.

CHAPTER 4.

STRUCTURAL IMPEDANCE MODEL OF SPECIMEN AND MAGNETOSTRICTIVE PATCH TRANSDUCER

The magnetostrictive patch transducer can be designed in various structures according to the specimen structure. For the quantification of magnetostrictive patch transducers, the structural and physical characteristics of these transducers and specimens should be considered. The structural characteristics are the dimensions of the specimen and the patch, and the physical characteristics are the material properties of the two materials. Ultimately, the model will be constructed and quantified by an equivalent circuit, so these characteristics will be considered in the form of impedance so that they can be applied to the circuit.

In addition, the influence of the adhesive layer between the specimen and the patch will be considered. When the wave propagates from the specimen to the patch and vice versa, the boundary condition can be simple to calculate in perfect bonding, but the actual behavior is different because there is an adhesive layer between them. Considering the change in behavior due to the adhesive layer is called the shear lag effect, the effective length of the actual patch will be obtained.

4.1 Structural impedance model

For quantification of a magnetostrictive patch transducer, the configuration of the specimen where the transducer is installed and the transducer itself must be considered, as it is impossible to calculate the physical quantity of signal coming through the actual transducer with the magnetostriction phenomenon alone. The structural impedance is suitable to consider both the material properties of the specimen and the configuration of the transducer. As frequency increases, second or other modes may occur in the transducer. However, in this study, design was performed considering only the lowest order torsional mode T(0,1).

4.1.1 Structural impedance configuration of specimen and magnetostrictive patch transducer

Assuming a planar wave propagating through the specimen, the configuration of the transducer can be treated as a one-dimensional impedance transmission line [45]. Therefore, the structures of the specimen and the transducer described above can be expressed as a transmission line in figure 4.1. The impedance of the specimen and the attached patch can be defined as $Z_s = \rho_s v_s A_s$, $Z_m = \rho_m v_m A_m$ where ρ , v , and A denote density, velocity, and area of the cross-section perpendicular to the z-axis, respectively.

If the loss is not taken into consideration in energy conversion, it can be assumed to be $A_m \Gamma_m^2 / (Z_m^B / A_m) = A_s \Gamma_s^2 / (Z_s / A_s)$ when an amplitude of the elastic wave is referred to as Γ where $Z_m^B = Z_m \sqrt{1 + K^2}$. K is the magnetomechanical coupling coefficient of the magnetostrictive material and the value of K is 0.14 for HiperCo 50A used in this study [66]. From here, the amplitude ratio due to the impedance difference between the specimen and the patch can be obtained.

I_3 , $\dot{\phi}_3$, and V_3 denote the current flowing through the coil, the rate of magnetic flux change applied to the magnetostrictive patch over time and the voltage applied to the coil. F_1 and F_2 are the forces applied to both ends of the patch, respectively. The particle velocities at both ends of the transducer are \dot{u}_1 , \dot{u}_2 and U_3 is the magnetic potential. Since both the structure and the behavior of the patch are symmetric, we assume that F_1 , F_2 and \dot{u}_1 , \dot{u}_2 are equal to each other [22]. The effective impedance of the specimen can be obtained by using the above-mentioned impedance values.

$$Z_s^{eff} = Z_m^B Z_s / (Z_m^B + Z_s). \quad (4.1)$$

I_3 and V_3 values can be measured experimentally and the relationship can be expressed as follows

$$V_3 = N\dot{\phi}_3 \quad U_3 = NI_3. \quad (4.2)$$

Figure 4.2 shows the structural impedance of a specimen and the magnetostrictive patch transducer in terms of an equivalent circuit configuration. Z_{ib} is the input impedance at the center of the circuit and it will be introduced in next section as follows by transmission line theory [67-69].

4.1.2 Input impedance by transmission line theory

Figure. 4.3 shows a lossless transmission line terminated in a load impedance Z_s^{eff} . Assume that an incident wave of the form $V_0^+ e^{-j\beta z}$ is generated at $z < 0$. The ratio of voltage to current for such a traveling wave is Z_m^B . However, when the line is ended in a load Z_s^{eff} , the ratio of voltage to current at the load must be Z_s^{eff} . Thus, from the perspective of wave propagation, a reflection wave must be excited with the appropriate amplitude to satisfy this condition. The total voltage and current on the line can be calculated in equations (4.3) and (4.4).

$$V(z) = V_0^+ e^{-j\beta z} + V_0^- e^{j\beta z}. \quad (4.3)$$

$$I(z) = \frac{V_0^+}{Z_m^B} e^{-j\beta z} - \frac{V_0^-}{Z_m^B} e^{j\beta z} \quad (4.4)$$

In addition, the total voltage and current at the load are related by the load impedance Z_s^{eff} , so load impedance can be expressed as follows at $z = 0$,

$$Z_s^{eff} = \frac{V(0)}{I(0)} = \frac{V_0^+ + V_0^-}{V_0^+ - V_0^-} Z_m^B. \quad (4.5)$$

Solving for V_0^- ,

$$V_0^- = \frac{Z_s^{eff} - Z_m^B}{Z_s^{eff} + Z_m^B} V_0^+. \quad (4.6)$$

The amplitude of the reflected voltage wave normalized to the amplitude of the incident voltage wave is Γ which is treated as the voltage reflection coefficient, generally.

$$\Gamma = \frac{V_0^-}{V_0^+} = \frac{Z_s^{eff} - Z_m^B}{Z_s^{eff} + Z_m^B}. \quad (4.7)$$

Using equation (4.7), the total voltage and current on the line can be obtained as,

$$V(z) = V_0^+ (e^{-j\beta z} + \Gamma e^{j\beta z}) . \quad (4.8)$$

$$I(z) = \frac{V_0^+}{Z_m^B} (e^{-j\beta z} - \Gamma e^{j\beta z}) \quad (4.9)$$

The voltage and current on the line consist of a super-position of an incident and a reflected wave. Intuitively, only when $\Gamma = 0$ is there no reflected wave and to obtain this condition, the load impedance Z_s^{eff} must be equal to Z_m^B .

The reflection coefficient Γ was defined as the ratio of the reflected to the incident voltage wave amplitudes at the load impedance, but this quantity can be generalized to any point l along the line as follows. From equation (4.3), with $z = -l$, the ratio of the reflected component to the incident component is,

$$\Gamma(l) = \frac{V_0^- e^{-j\beta l}}{V_0^+ e^{j\beta l}} = \Gamma(0) e^{-2j\beta l} . \quad (4.10)$$

The real power flow on the line is a constant because a lossless line is assumed. However, the voltage amplitude, at least for a mismatched line, is oscillatory with position on the line. Therefore, the input impedance which means parallel impedance at the center of the transmission line when looking toward the load on the back face of the transducer is,

$$Z_{ib} = \frac{V(-l)}{I(-l)} = \frac{V_0^+ (e^{j\beta l} + \Gamma e^{-j\beta l})}{V_0^+ (e^{j\beta l} - \Gamma e^{-j\beta l})} Z_m^B = \frac{1 + \Gamma e^{-2j\beta l}}{1 - \Gamma e^{-2j\beta l}} Z_m^B. \quad (4.11)$$

A more usable form may be obtained by using equation (4.7),

$$\begin{aligned} Z_{ib} &= Z_m^B \frac{(Z_s^{eff} + Z_m^B)e^{j\beta l} + (Z_s^{eff} - Z_m^B)e^{-j\beta l}}{(Z_s^{eff} + Z_m^B)e^{j\beta l} - (Z_s^{eff} - Z_m^B)e^{-j\beta l}} \\ &= Z_m^B \frac{Z_s^{eff} \cos(\beta l) + jZ_m^B \sin(\beta l)}{Z_m^B \cos(\beta l) + jZ_s^{eff} \sin(\beta l)} \\ &= Z_m^B \frac{Z_s^{eff} + jZ_m^B \tan(\beta l)}{Z_m^B + jZ_s^{eff} \tan(\beta l)} \end{aligned} \quad (4.12)$$

In here, if $\Omega = \pi\omega / 2\omega_0 = \beta l$ is used, finally the input impedance is obtained by transmission line theory as follows,

$$Z_{ib} = Z_m^B \frac{Z_s^{eff} + jZ_m^B \tan \Omega}{Z_m^B + jZ_s^{eff} \tan \Omega}. \quad (4.13)$$

Therefore, it is possible to express the structural impedance of the specimen and the patch due to the impedances thus obtained. The configuration similar to the actual experiment can be realized by considering the structure of the specimen and the patch with the impedance values of various equipment (These values are shown in table 4.1)

4.2 Effective patch width by the shear lag phenomenon

In the previous section, the model is designed assuming that the specimen and the patch are in perfect bonding. However, they are not perfectly coupled due to the adhesive bonding layer. This phenomenon is called the shear lag effect [70-76] and when the width of the actual patch is l_m , the effective patch width l_m^{eff} involved in actual bonding can be calculated.

The typical configuration of the system is shown in figure 4.3. The patch has length l and thickness h_m while the bonding layer has a thickness h_a . The specimen has depth h_s and width w_s . Let σ_m be the axial stress in the patch and τ be the interfacial shear stress. Let u_m be the displacement at the interface between the patch and the bonding layer, and u_a be the corresponding displacement at the interface between the bonding layer and the specimen.

Considering static equilibrium of the differential element of the patch in the x direction, as shown in figure 4.3.

$$\tau = \frac{\partial \sigma_m}{\partial x} h_m. \quad (4.14)$$

The bending moment is given by,

$$M = \sigma_m w_m h_m (0.5h_s + h_a + 0.5h_m). \quad (4.15)$$

Using Euler-Bernoulli's beam theory and assuming $h_m + 2h_a \ll h_s$, equation (4.15) can be,

$$\sigma_s + \left(\frac{3\sigma_m w_m h_m}{w_s h_s} \right) = 0, \quad (4.16)$$

where σ_s denotes the bending stress on the specimen. Differentiating with respect to x , equation (4.16) can be written as,

$$\frac{\partial \sigma_s}{\partial x} + \left(\frac{3w_m}{w_s h_s} \right) \tau = 0, \quad (4.17)$$

The stress terms in equations (4.14), (4.16) can be replaced in stain terms as follows,

$$\frac{\partial^2 \varepsilon_s}{\partial x^2} = \left(\frac{G_a \varepsilon_s}{E_m h_a h_m} \right) \xi, \quad (4.18)$$

$$\frac{\partial^2 \varepsilon_s}{\partial x^2} = - \left(\frac{3w_m G_a \varepsilon_s}{E_s w_s h_s h_m} \right) \xi \quad (\xi = \varepsilon_m / \varepsilon_s - 1), \quad (4.19)$$

where G_a is the shear modulus of the bonding layer, E_m and E_s are Young's modulus of elasticity of the patch and the specimen. Subtracting equation (4.18) from equation (4.19), the following equation can be obtained.

$$\frac{\partial^2 \xi}{\partial x^2} - H^2 \xi = 0, \quad (4.20)$$

where

$$H^2 = \left(\frac{G_a}{E_m h_a h_m} + \frac{3G_a w_m}{E_s w_s h_s h_m} \right), \quad (4.21)$$

The parameter H is called the shear lag parameter. The general solution of equation (4.20) is,

$$\xi = A \cosh Hx + B \sinh Hx, \quad (4.22)$$

Applying boundary condition, equation (4.22) can be transformed as,

$$\xi = -\frac{\cosh Hx}{\cosh Hl}, \quad (4.23)$$

In order to quantify the effect of shear lag, effective length l_{eff} can be computed as defined by *Sirohi and Chopra* [77];

$$l_{eff} = \int_{x=0}^{x=l} \frac{\varepsilon_m}{\varepsilon_s} dx = \left(1 - \frac{\tanh(Hl)}{Hl}\right)l, \quad (4.24)$$

The obtained value of the effective patch width l_m^{eff} is used in the structural impedance model instead of the width of the actual patch.

The influence of the adhesive bonding layer causes the peak frequency of the actual transducer to move finely, which is shown in the figure 4.4. The fact that it is similar to the actual experimental value due to the frequency shift has been confirmed in the relevant study [71], and the result is also close to the actual experimental value in this study.

Table 4.1 List of frequency-specific equipment used in the experiments for verifying the proposed model.

Equipment	Low freq. range	Impedance	High freq. range	Impedance
Function generator	33220A (Agilent)	50 Ω	33220A (Agilent)	50 Ω
Power amp	B&K2718 (B&K)	15 k Ω	AG1017 (AD)	50 Ω
Pre-amp	SR560 (SRS)	100 M Ω +25 pF	SR560 (SRS)	100 M Ω +25 pF
Oscilloscope	Waverunner 520i (Lecroy)	50 Ω	Waverunner 520i (Lecroy)	50 Ω

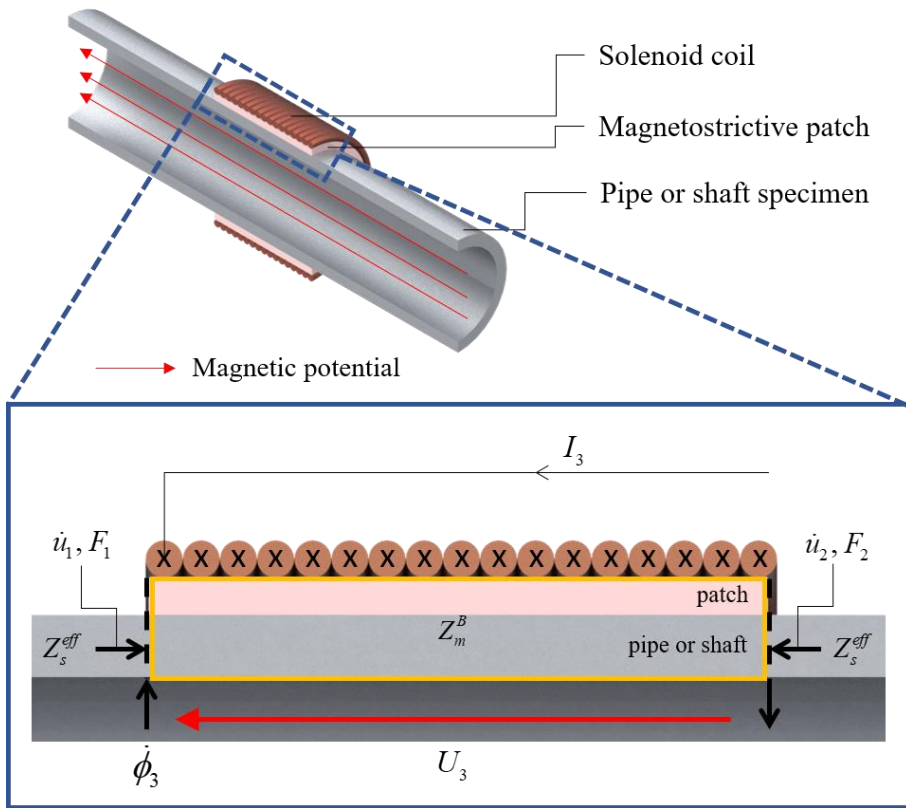


Fig. 4.1 Cross section of the specimen and the magnetostrictive patch transducer. the structural impedance configuration of these is shown in the blue box.

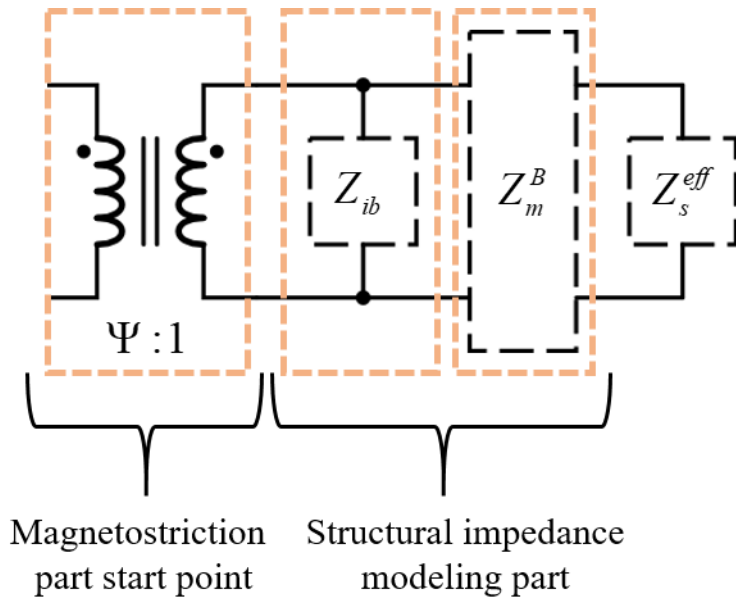


Fig. 4.2 Equivalent circuit model representing the structural impedance of the specimen and the magnetostrictive patch transducer.

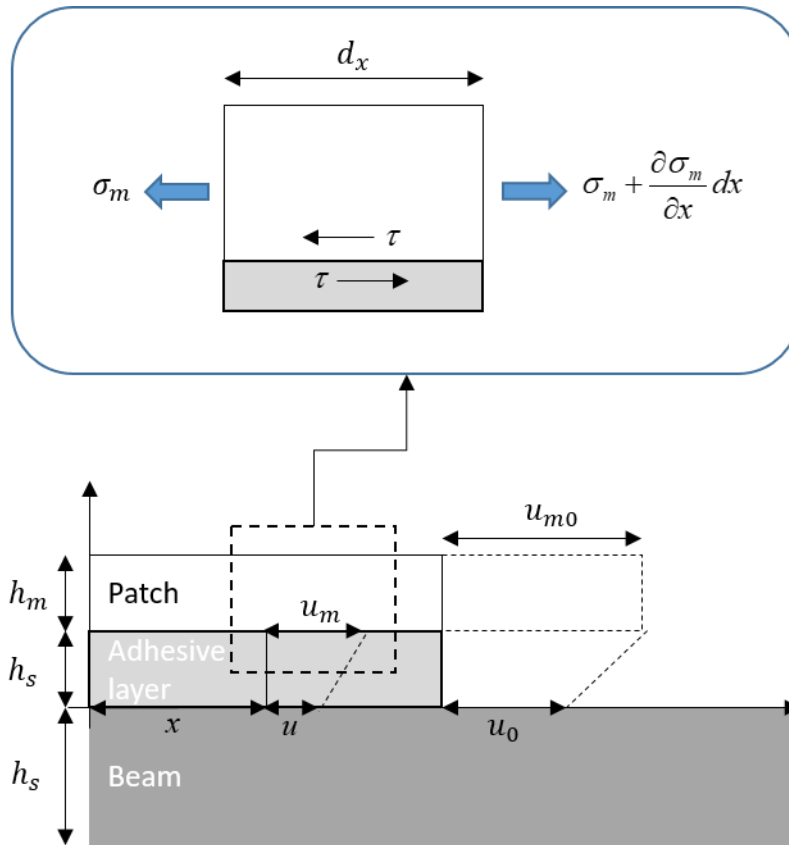


Fig. 4.3 Deformation profile of the patch, the specimen and the adhesive layer.

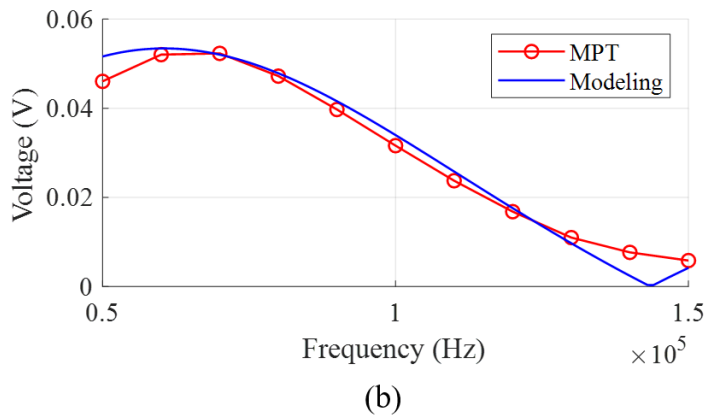
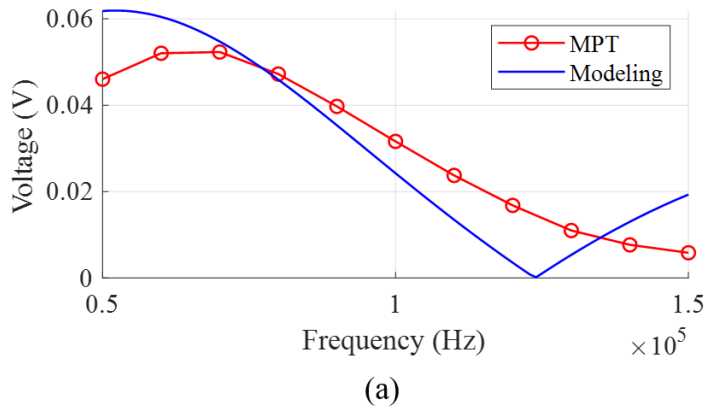


Fig. 4.4 Model results according to shear lag effect.

CHAPTER 5.

FULLY COUPLED CIRCUIT MODEL FOR MAGNETOSTRICTION IN MAGNETOSTRICTIVE PATCH TRANSDUCER

The linear equations for the magnetostriction phenomenon were examined. As mentioned in chapter 3, linear equations [78-80] are difficult to obtain accurate physical quantities and only tendencies of magnetostriction phenomenon can be obtained. In order to quantify the transducers, which are the object of this study, we try to construct a model in which both mechanical and magnetic variables are fully coupled and consider a nonlinearity of the phenomenon resulting from the material properties of magnetostrictive material.

Before the model, we first introduce fully coupled magnetostriction equations which are improved from linear magnetostriction equations. The nonlinear properties of the material are considered in this equation, and these properties of the magnetostrictive material are obtained through experiments and expressed in an approximate expression.

These equations, obtained from a mechanical equation, will be transformed into a circuit equation [81-85] for application to an equivalent circuit. Finally, an equivalent

circuit representing the magnetostriction phenomenon in the magnetostrictive patch using these equations will be obtained, and the system for the transducer as a whole will be modeled.

5.1 Fully coupled magnetostriction equation

5.1.1 Approximate expressions for nonlinear properties of magnetostrictive material (HiperCo 50A)

In the case of magnetostrictive materials, as mentioned in chapter 2, the mutual conversion of mechanical energy and electromagnetic energy occurs in the material. The curve showing the relationship between the magnetic field and the physical field is called the magnetostriction curve. Therefore, the experiment as shown in figure 5.1 is constructed to directly obtain the magnetostriction curve of this material.

The two coils are used as a coil for applying a static magnetic field and a coil for obtaining a magnetic flux density generated inside, respectively. In the case of magnetostrictive materials, when a static magnetic field is applied, deformation is caused by the static magnetic field. In order to obtain this strain, laser measurement equipment (OFV-5000, OFV-551, Polytec, Waldbronn) is used. The gauss meter

inside the coil measures the internal magnetic field, and through this experiment, the magnetization of the material can be obtained as follows

$$V_{coil} = -N \frac{\Delta\Phi}{\Delta t}, \quad (5.1)$$

$$\Phi = B \cdot S, \quad (5.2)$$

$$M = B - \mu_0 H, \quad (5.3)$$

V_{coil} is the voltage applied to the coil to apply the static magnetic field and the magnetic flux density Φ in the pick-up coil can be obtained based on this voltage. The magnetic induction B inside the pick-up coil can be obtained from equation (5.2) and as the magnetic field H , the measured value of gauss meter is used. The experimental method is also used in various study [68, 71]. As a result, the magnetization M of the magnetostrictive material can be obtained through equation (5.3) and the result is the same as figure 5.2. In the same experimental setup, the strain according to the magnetic field measured by laser measurement equipment is the same as figure 5.3. The approximate formula from the experimental data is as follows [71]

$$M(\sigma, H) = \varphi'(z) = M_s \cdot \tanh(\alpha z)^2, \quad (5.4)$$

$$f(\sigma) = \beta(\sigma + \sigma_0), \quad (5.5)$$

$$z = \frac{H}{f(\sigma)} = \frac{H}{\beta(\sigma + \sigma_0)}, \quad (5.6)$$

M_s is the saturation magnetization value and σ_0 is the residual stress value in the material. The HiperCo 50A used in this study was subjected to annealing, and residual stress was removed. M_s , α and β are model parameters which can be obtained numerically from figure 5.2 and have values of 1.63, 0.0135 and 0.82, respectively.

5.1.2 Improvement of magnetostriction equation with consideration of nonlinear properties

Magnetic field H and stress σ are chosen to be the state variables, while strain $\varepsilon = \varepsilon(\sigma, H)$ and magnetic induction $B = B(\sigma, H)$ are the state functions. Consider a process $(H(t), \sigma(t))$ in a time interval $t \in [0, T]$. The work $W(t_1, t_2)$ done by the magnetic and mechanical forces in an arbitrary interval $[t_1, t_2] \subset [0, T]$ is given by the integral,

$$W(t_1, t_2) = \int_{t_1}^{t_2} (\dot{\epsilon}(t)\sigma(t) + \dot{B}(t)H(t)) dt \quad (5.7)$$

The process is said to be reversible if there exists another state function, which means free energy, $F = F(\sigma, H)$ such that the work $W(t_1, t_2)$ is completely transformed into an energy increase with no energy losses, that is;

$$W(t_1, t_2) = F(\sigma(t_2), H(t_2)) - F(\sigma(t_1), H(t_1)) \quad (5.8)$$

If losses are present, part of the work is dissipated into heat. In isothermal processes, the dissipation

$$D(t_1, t_2) = W(t_1, t_2) - (F(\sigma(t_2), H(t_2)) - F(\sigma(t_1), H(t_1))) \quad (5.9)$$

is non-negative, in agreement with the second principle of thermodynamics [86-88].

In general, losses make the process irreversible. In differential form, the energy balance relations for reversible processes read;

$$\dot{\epsilon}(t)\sigma(t) + \dot{B}(t)H(t) = \frac{d}{dt} F(\sigma(t), H(t)) \quad (5.10)$$

and for irreversible processes;

$$\dot{\varepsilon}(t)\sigma(t) + \dot{B}(t)H(t) \geq \frac{d}{dt} F(\sigma(t), H(t)) \quad (5.11)$$

A constitutive law $\varepsilon = \varepsilon(\sigma, H)$, $B = B(\sigma, H)$ is said to be thermodynamically admissible, if equation (5.11) holds for every process $(\sigma(t), H(t))$.

In this study, the loss is basically ignored. First, since the transducer itself does not utilize a large energy, the heat is not generated much. Also, the material having almost no hysteresis is used to optimize the transducer configuration so as to avoid an irreversible reaction, that is, loss.

Therefore, when only the reversible reaction is considered, equation (5.10) can be written by the chain rule as,

$$\sigma \frac{\partial \varepsilon}{\partial \sigma} \dot{\sigma} + \sigma \frac{\partial \varepsilon}{\partial H} \dot{H} + H \frac{\partial B}{\partial \sigma} \dot{\sigma} + H \frac{\partial B}{\partial H} \dot{H} = \frac{\partial F}{\partial \sigma} \dot{\sigma} + \frac{\partial F}{\partial H} \dot{H} \quad (5.12)$$

Since equation (5.12) has to hold for every process, it can be transformed as,

$$\sigma \frac{\partial \varepsilon}{\partial \sigma} + H \frac{\partial B}{\partial \sigma} = \frac{\partial F}{\partial \sigma}, \quad \sigma \frac{\partial \varepsilon}{\partial H} + H \frac{\partial B}{\partial H} = \frac{\partial F}{\partial H} \quad (5.13)$$

Introducing the Gibbs energy,

$$G(\sigma, H) = F(\sigma, H) - \sigma \varepsilon(\sigma, H) - HB(\sigma, H), \quad (5.14)$$

Rewrite equation (5.13) in the form,

$$\varepsilon = -\frac{\partial G}{\partial \sigma}, \quad B = -\frac{\partial G}{\partial H}. \quad (5.15)$$

A necessary and sufficient condition for the existence of a Gibbs energy satisfying equation (5.15) is the potentiality condition,

$$\frac{\partial B}{\partial \sigma} = \frac{\partial \varepsilon}{\partial H}. \quad (5.16)$$

Consider first the linear magnetostriction equation which is mentioned at chapter 3,

$$\begin{aligned} \varepsilon &= \frac{1}{E} \sigma + dH, \\ B &= \mu H + d^* \sigma, \end{aligned} \quad (5.17)$$

where E is the elasticity modulus, and μ is the magnetic permeability. Equation (5.16) is compatible with equation (5.17) if and only if $d = d^*$. In this case, the Gibbs energy is quadratic in the form

$$G = \frac{1}{2E} \sigma^2 + \frac{\mu}{2} H^2 + d\sigma H. \quad (5.18)$$

Prior to analysing the magnetostrictive characteristics of the material, it is necessary to know the material property data like magnetostriction curves. The experimental process to obtain the non-linear magnetic properties of HiperCo 50A used in this study are discussed in previous subsection. In the case of HiperCo 50A, deformation by the magnetostriction is large and hysteresis for the magnetic field is relatively small such as Galfenol or Tefenol-D, which is widely used as magnetostrictive alloy material. Therefore, the effect of hysteresis can be neglected. Considering that the magnetostriction phenomenon is the mutual conversion between mechanical energy and electromagnetic energy, the following Gibbs free energy approach can be used [89,90].

$$G = \frac{1}{2E} \sigma^2 + \frac{\mu}{2} H^2 + f(\sigma)\varphi(z), \quad (5.19)$$

where E is the modulus of elasticity of the material, μ_0 is the permeability at vacuum, $f(\sigma)$, $\varphi(z)$ and $u(\sigma, H)$ are functions determined by the material properties. The first two terms in the right side of equation (5.19) are pure elastic and magnetic contributions, respectively. The third term refers to the contribution of coupling between the deformation and the magnetic field in the magnetostrictive material. Based on equation (5.19), the equations for strain and magnetic field are as follows

$$\begin{aligned}
\varepsilon &= \left. \frac{\partial G}{\partial \sigma} \right|_H \\
&= \frac{\sigma}{E} + f'(\sigma) \cdot \varphi(z) + f(\sigma) \cdot \varphi'(z) \cdot \frac{\partial z}{\partial \sigma}, \\
&= \frac{\sigma}{E} + f'(\sigma) \cdot [z \cdot \varphi'(z) - \varphi(z)]
\end{aligned} \tag{5.20}$$

$$\begin{aligned}
B &= \left. \frac{\partial G}{\partial H} \right|_\sigma \\
&= \mu H + f(\sigma) \cdot \varphi'(z) \cdot \frac{\partial z}{\partial H}. \\
&= \mu H + \varphi'(z)
\end{aligned} \tag{5.21}$$

Using the approximate values obtained from the experiment in previous subsection, equation (5.20) and (5.21) can be rearranged as follows

$$\varepsilon = \left. \frac{\partial G}{\partial \sigma} \right|_H = \frac{\sigma}{E} + \beta \cdot \left\{ z \cdot [M_s \cdot \tanh^2(\alpha z)] - \left[z - \frac{\tanh(\alpha z)}{\alpha} \right] \right\}. \tag{5.22}$$

$$B = \left. \frac{\partial G}{\partial H} \right|_{\sigma} = \mu H + M_s \tanh^2(\alpha z). \quad (5.23)$$

Equations (5.22) and (5.23) is the fully coupled analysis result of the phenomenon itself, taking into account the non-linear properties of the magnetostrictive material obtained experimentally. This will be applied to the equivalent circuit design for the magnetostriction phenomenon later.

5.2 Circuit model of torsional magnetostrictive patch transducer

Once the structural model of the specimen and the magnetostrictive patch have been constructed, we will now try to design the model of the magnetostriction phenomenon that occurs inside the patch. In order to express the magnetostriction phenomenon, mechanical, magnetic, and electrical characteristics should be considered separately. Since it deals with the phenomenon occurring in the patch itself, it works independently of the structure of the transducer and the influence on the structure is considered as the previous impedance model.

5.2.1 Circuit equations converted from the mechanical

equations

Once the structural model of the specimen and the magnetostrictive patch have been constructed, we will now try to design the model of the magnetostriction phenomenon that occurs inside the patch. In order to express the magnetostriction phenomenon, mechanical, magnetic, and electrical characteristics should be considered separately. To represent equation (5.16) more appropriately for the model, the following modification is performed.

$$x = \frac{F_1}{\xi} + l_m \cdot g(F_1, H_m), \quad (5.23)$$

$$\phi_m = \mu_0 H_m A_m + A_m \cdot m(F_1, H_m).$$

where $\xi = EA_m / l_m$, and this means mechanical stiffness. ϕ_m , H_m are magnetic flux and magnetic field in the patch, respectively and $g(F_1, H_m) = -f'(\sigma) \cdot [z \cdot \varphi'(z) - \varphi(z)]$, $m(F_1, H_m) = \varphi'(z)$. In the second equation of equation (9), the first term of the right side, $\mu_0 H_m A_m$, can be expressed as $\mathfrak{R}_m = l_m / \mu_0 A_m$ where \mathfrak{R}_m is the reluctance value of the linear contribution of the magnetostrictive material. Therefore, the non-linear contribution by the magnetostriction model and the linear contribution due to the property of the patch itself are as follows

$$\begin{aligned}
F_1 &= \xi x - l_m \xi \cdot g(F_1, H_m), \\
H_m l_m &= \mathfrak{R}_m \phi_m - \mathfrak{R}_m A_m \cdot m(F_1, H_m).
\end{aligned} \tag{5.24}$$

In the first equation of equation (5.24), the mechanical variables can be replaced by the electrical equivalent variables which are $F_1(t) = V_1$ and $\dot{x}(t) = I_1$. These are applied to equation (5.24) and it can be rearranged as,

$$\begin{aligned}
V_1 &= \xi \int_t I_1 dt - l_m \xi \cdot g(V_1, H_m), \\
H_m l_m &= \mathfrak{R}_m \phi_m - \mathfrak{R}_m A_m \cdot m(V_1, H_m).
\end{aligned} \tag{5.25}$$

The second equation in equation (5.25) represents the magnetic component, which can also be expressed as a magnetic voltage $H_m l_m = V_m$ by magnetic circuit theory [91, 92]. The reluctance \mathfrak{R}_m is the resistance R_m in the electrical circuit and the flux ϕ_m in \mathfrak{R}_m can be denoted by I_m .

$$\begin{aligned}
V_1 &= \xi \int_t I_1 dt - l_m \xi \cdot g(V_1, \frac{V_m}{l_m}), \\
V_m &= R_m I_m - R_m A_m \cdot m(V_1, \frac{V_m}{l_m}).
\end{aligned} \tag{5.26}$$

Though equation (5.26) consists of equivalent elements of the electric circuit, the first equation expresses the mechanical component and the second equation expresses the magnetic component. Therefore, if it is realized by the equivalent circuit as shown in figure 5.4, it can be seen that the mechanical and magnetic parts are expressed by each equation, respectively.

To explain equation (5.26) in terms of an equivalent circuit, the first equation is about the equation that expresses the voltage source by the series capacitance $C = 1 / \xi = l_m / EA_m$ and the voltage source representing a non-linear mechanical behavior of the magnetostrictive material. In the case of the second equation, the equation expresses the voltage across the series resistance R_m , which implies linear reluctance, and the non-linear voltage implying non-linear reluctance.

To check the electrical energy conversion, Faraday's law reads

$$V_2(t) = -\frac{d}{dt} \Phi_m(t), \quad (5.27)$$

where $\Phi_m(t) = N_2 \phi_m$ and this means flux linkage in the pick-up coil. When a current flow into the coil, this current affects the total magnetic flux flowing in the magnetostrictive patch. Thus, the voltage source corresponding to $N_2 I_2$ is added in figure 5.4. Finally, the circuit such as figure 5.5 can be constructed considering

the electric part which represents the electric transfer energy by the coil. The circuit shown in figure 5.5 is a model for the magnetostrictive patch and the coil. If the permanent magnets for the static magnetic field in magnetostrictive patch transducer is considered, a new circuit can be constructed by adding new lumped elements based on the model.

5.2.2 Equivalent circuit model based on torsional magnetostrictive patch transducer

In this study, the target transducer has the same structure as figure 5.6 and the circuit is newly constructed as figure 5.7 in consideration of the permanent magnets located on both sides besides the patch. Since the influence of the external static magnetic field always coupled when the magnetostrictive material deforms, the magnetostrictive phenomenon and the magnet should be formed as an integrated port in order to have both excitation and measurement process directions. In the case of

R_{leak} , it represents the value for leakage flux [93] and can be calculated as

$$R_{leak} = l_s / \mu_s S_s \quad (\mu_s \text{ is permeability of HiperCo 50A [26]). } V_{mag}, R_{mag} \text{ are}$$

elements for expressing an additional static magnetic field by the permanent magnet.

The overall equation for the circuit is as follows

$$\begin{aligned}
V_1 &= \xi \int I_1 dt - l_m \xi \cdot g(V_1, \frac{V_m}{l_m}) - I_{mag} R_{mag} - V_{mag} + N_2 I_2, \\
V_m &= R_m I_m - R_m A_m \cdot m(V_1, \frac{V_m}{l_m}) - V_1 + N_2 I_2 \\
I_1 &= I_{leak} + I_{mag}, \\
V_{mag} &= I_{leak} R_{leak} - I_{mag} R_{mag}, \\
V_2 &= -\frac{d}{dt}(N_2 \cdot I_2), \\
V_{out} &= R_{coil} I_2 - V_2.
\end{aligned} \tag{5.28}$$

Therefore, the magnetostrictive patch, the permanent magnet and the electric circuit for the solenoid coil are represented, and the non-linear property of the magnetostrictive material is also implied in the model described in figure 5.7.

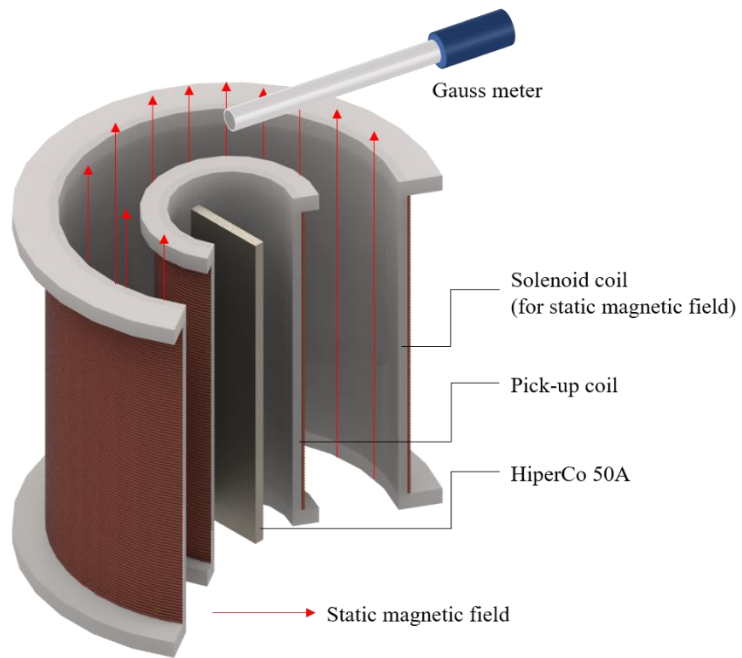


Fig. 5.1 Experimental configuration for HiperCo 50A magnetostriction analysis.

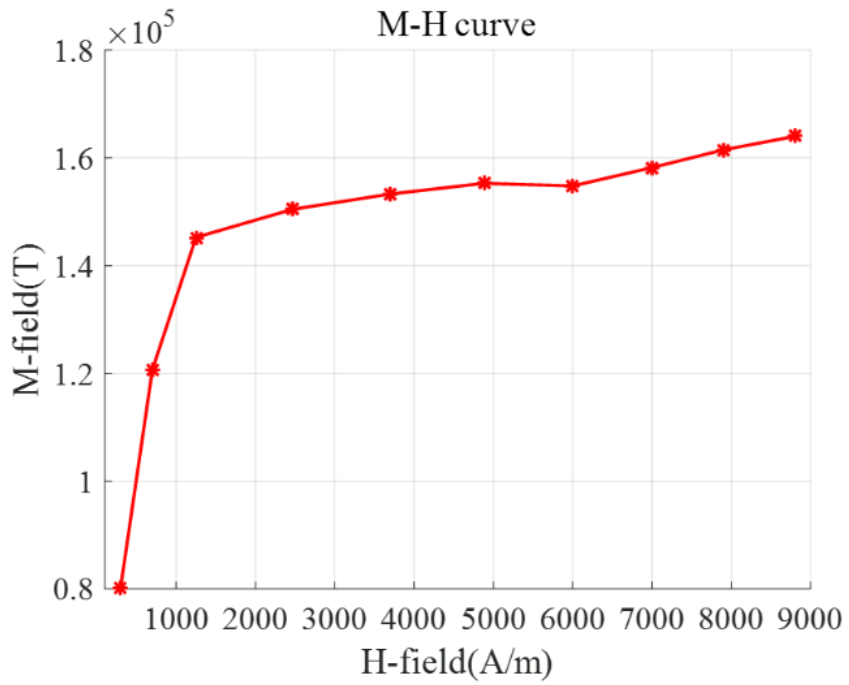


Fig. 5.2 Graphs of magnetic properties of HiperCo 50A. Experimentally obtained $M - H$ curve.

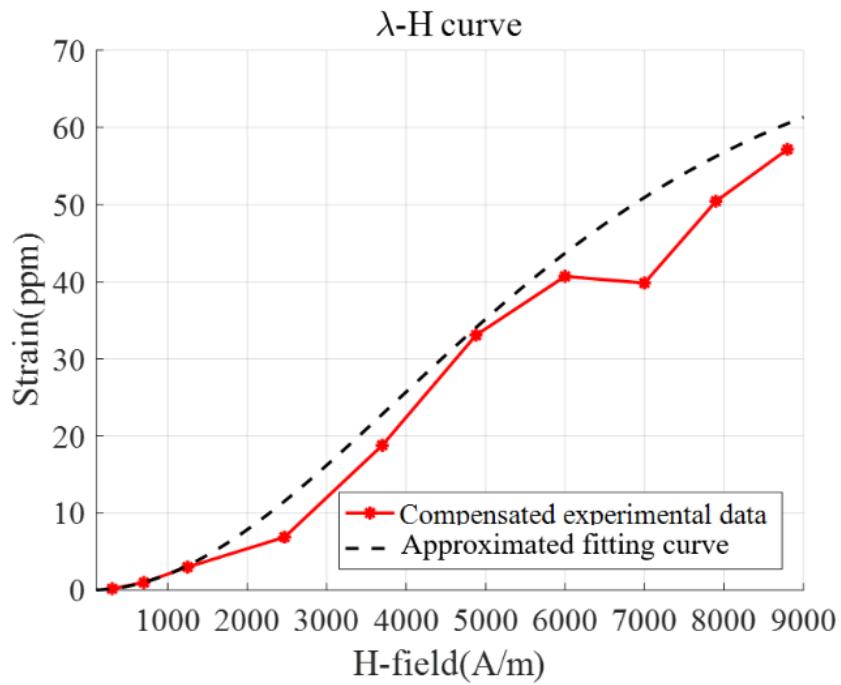


Fig. 5.3 Graphs of magnetic properties of HiperCo 50A. Experimentally obtained $\lambda - H$ curve and reference data.

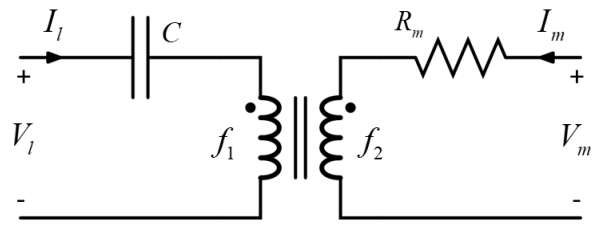


Fig. 5.4 Fundamental equivalent circuit model for magnetostriction. Basic model of the magnetostriction phenomenon

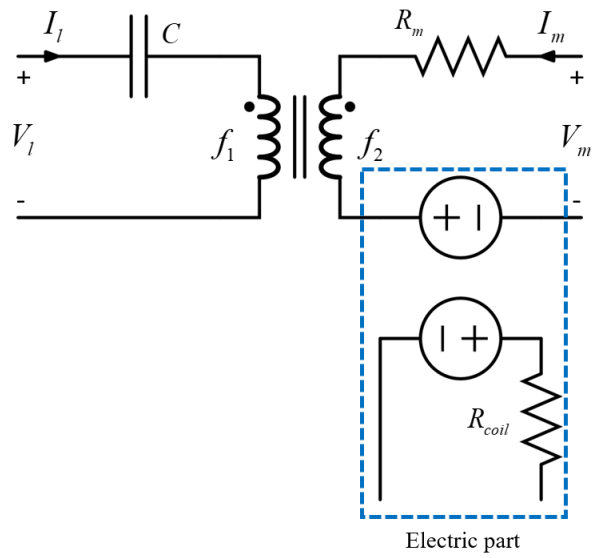


Fig. 5.5 Fundamental equivalent circuit model for magnetostriction. The model with additional coil parts for electric transfer energy.

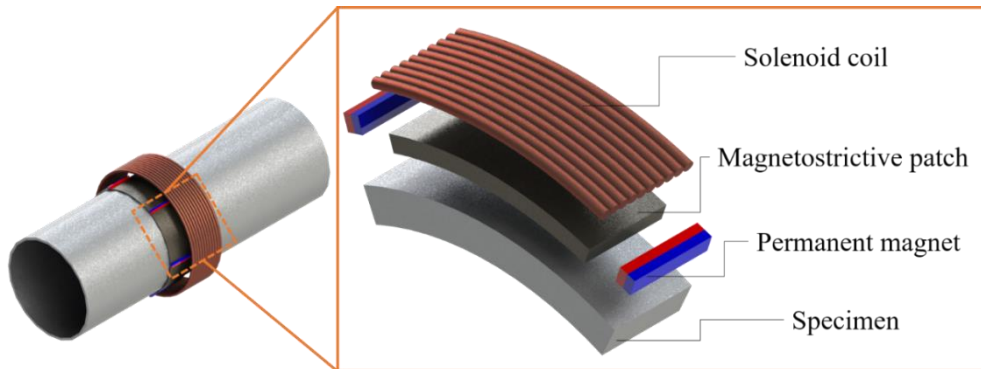


Fig. 5.6 The configuration of the magnetostrictive patch transducer used in this study.

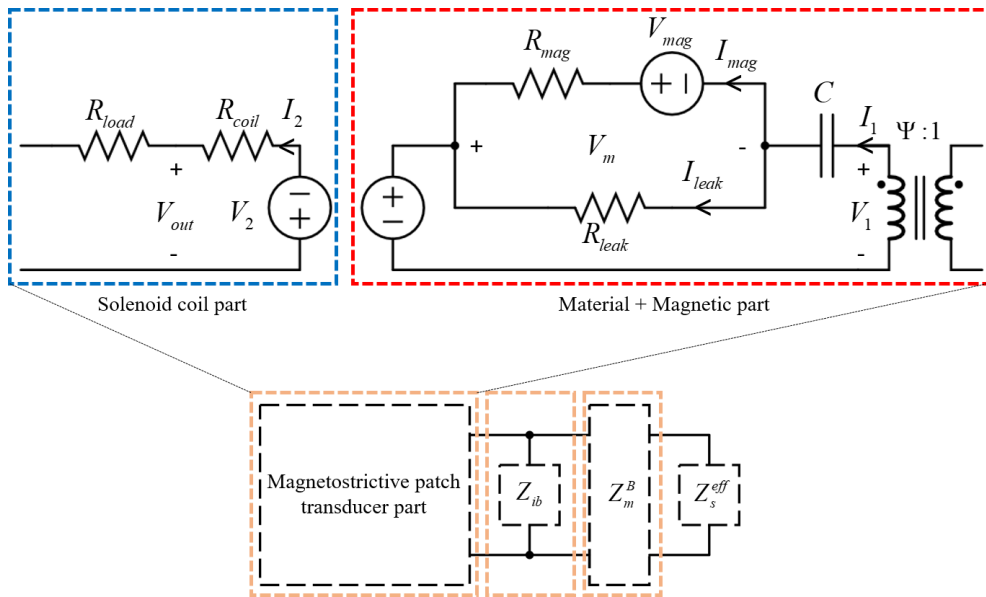


Fig. 5.7 Equivalent circuit model for non-linear magnetostriction phenomenon considering solenoid coils for dynamic magnetic field and magnet for the static magnetic field.

CHAPTER 6.

EXPERIMENTAL VERIFICATION FOR QUALIFICATION OF MAGNETOSTRICTIVE PATCH TRANSDUCER WITH FULLY COUPLED CIRCUIT MODEL

In this chapter, the contents of verification by quantitatively comparing with the value obtained from the actual experiment with the model described above will be included. The final quantities to be obtained through the model are strain in excitation case, and voltage in measurement case. In the case of the strain, the strain gauge will be used to obtain the experimental value and the voltage will be obtained from the oscilloscope measured value.

In order to verify the versatility of the model, various design variables are changed and a comparison between the model value and the experimental value are performed. Since the structure and material properties of the specimen and the transducer were considered through the structural impedance model, the dimensions of the patch and the material of the specimen will be varied. The static magnetic field, which has the greatest influence on the performance of the magnetostrictive patch transducer, will also be changed to change the strength of the permanent magnet used to verify that the model follows the behavior of the actual transducer.

6.1 Experimental setup

To verify the validity of the model, we compared the values obtained from the model and experiments. The configurations used in the experiments are shown in figure 6.1. For an excitation performance, vibration or ultrasonic wave generated by the magnetostrictive patch transducer was measured with a strain gauge at a distance of 300 mm in order to minimize the effect of damping. Especially, in the vibration region, since the wave do not propagate and form a mode distribution, the distance between the transducers is irrelevant even if the wavelength is long. At a low frequency (vibration) region, the vibration is generated by the input signal which has a 20-cycles sine waveform and at a high frequency (ultrasonic) region, a Gabor waveform [94] having a relatively short wavelength is used as an input signal to minimize an influence of the reflected wave. In the model, a signal generated by the function generator obtained from an oscilloscope was used as an input source. For a measurement performance, the same waveforms as those of the case of excitation were used and the magnetostrictive patch transducer and the strain gauge at the same distance from the shaker exciting the specimen received signals. The signal obtained from the strain gauge was calibrated to strain and used for the model as an input signal to the magnetostrictive patch transducer. Since the equipment used in the experiments varies according to the frequency range, the signals were compared in two regions, low-frequency range (vibration) and high-frequency range (ultrasonic

wave). The low-frequency range is 20 to 55 Hz and the high-frequency range is 50 to 150 kHz. In the case of the high-frequency range, the range is set around the 1st peak frequency, and it is actually the frequency at which the transducer is used. Table 3.1 shows the impedance values of the equipment used in each experiment.

6.2 Comparison of field variables from the circuit model and those of the experimental results

The physical quantities of the final outputs differ depending on the excitation and the measurement. In the case of the excitation, the strain value generated in the specimen caused by a deformation of the magnetostrictive patch is regarded as the final output. On the other hand, in case of measurement, a voltage value generated in the patch caused by the deformation from the specimen is regarded as the final output. The result of these two final outputs is obtained according to the frequencies, and these compared with the experimental data are shown in figure 6.2 and 6.3. Here, the strain in y-axis refers to the strain generated in the specimen and the voltage in y-axis refers to the voltage output from the oscilloscope.

Figure 6.2 shows the model values and the experimental values according to the frequencies of excitation and measurement at low-frequency range, respectively.

Figure 6.4 shows the time signal corresponding to 50 Hz in the previous results. The

reconstructed signal based on the model has a waveform and an amplitude similar to the time signal obtained from the actual strain gauge and the magnetostrictive patch transducer. In the case of excitation, the maximum error rate is about 13.3 % at 46 Hz and in the case of measurement, the maximum error rate is about 10 % at 50 Hz. This result confirms that the model implements the experimental data well.

Figure 6.3 and 6.5 shows the result at the high-frequency range described above, and the frequency range includes a peak frequency of 60 kHz, which corresponds to the first mode resonance frequency of the patch having the width of 25 mm. It can be seen that the tendency according to the frequency agrees well with the experimental results in both excitation and measurement. The maximum error rate in the case of excitation is about 12.1 % at 50 kHz and the maximum error rate in the case of measurement is about 9.8 % at 50 kHz. In the proposed model, since structural physical quantities of the patch such as the width are considered, a relatively large error rate occurs due to the influence of the first mode resonance of the patch. Although the influence is negligible outside the resonance frequency range, the error is relatively large in the vicinity of the resonance frequency due to a sudden change of the signal amplitude depending on the patch width.

6.3 Database on measurement performance based on various variables

In this section, various design variables are changed and a comparison between the model value and the experimental value are performed in order to verify the versatility of the model. In chapter 4, structural impedance model is constructed considering the structure and physical properties of specimen and transducer. Therefore, in order to verify this, we first changed the material properties of the specimen, ie, from steel to aluminum, and the width of the patch that affects the intensity and peak frequency of the transducer also changed.

The static magnetic field, which has the greatest influence on the performance of the magnetostrictive patch transducer, will also be changed to change the strength of the permanent magnet used to verify that the model follows the behavior of the actual transducer. Here, the dimension of the magnet is not changed because only the static field is considered in the variable.

6.3.1 Changes in measurement performance due to the structural variables

When a magnetostrictive patch transducer is used as a sensor to measure a signal, a database of various parameters in the model should be built and it is verified to increase the reliability of the model. Using equipment according to a frequency range, the strain values quantified through the model and the experiments are measured. The constructed database based on the distance L (magnitude) and a frequency of the strain values is shown in figures 6.6 and 6.7. The error rates between the model and the experimental result are shown to be approximately 10 % and this result confirms that the model has shown robust performance as these error rates have been derived even without changing the correction values in both the low-frequency range and the high-frequency range.

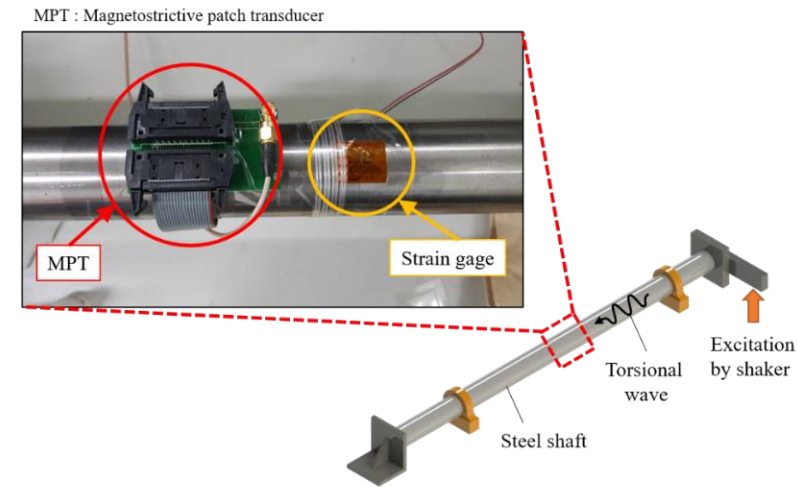
In addition to a magnitude of the strain and a frequency, structural parameters are changed to examine the responses to the specimen expressed as structural impedance and the structure variables of the patch. For the specimen, the material properties are changed from steel to aluminum. In case of the patch, further experimental and modeling analysis are performed for the patch widths of 10 mm and 15 mm, which are factors affecting the resonance frequency. The result of the change in aluminum properties is shown in figures 6.8 and 6.9. It confirms that the model well follows the variation of the measurement signal amplitude in the experiment caused by the change of the material properties. Furthermore, when the width of the patch is 10 mm or 15 mm, the resonance frequencies of the first mode are 150 kHz or 100 kHz, respectively. As shown in figures 6.10 and 6.11, the model results are well aligned

with the experimental results. It verifies that the proposed model coordinates well with the behavior of the actual transducer for structural variables.

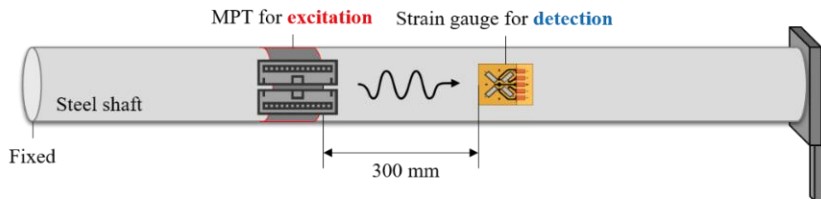
6.3.2 Influence of static magnetic field by the permanent magnet

To examine the influence of the magnets, which are part of the model, we used the magnets of different intensities and examined the measured outputs of the model and the experiment. Generally, the static field applied to the transducer is used to measure the most suitable intensity experimentally, but in this experiment, the tendency is analyzed to see the influence. The signal amplitudes around the resonance frequency where the output of the transducer is strongest are compared to see the proper variation because the performance of the transducer is considerably sensitive to the intensity of the applied static magnetic field. If a static magnetic field of sufficient intensity is not applied in the weak frequency region, the amplitude of the signal will be too small. Figure 12 shows the result of changing the intensity of a magnetic field on a surface of the magnet to 0.1 T, 0.2 T, and 0.3 T in the same dimension. Since the magnetic properties within the material are not linear, the amplitudes of the signals also tend to be non-linear. The model and the experimental result have an error rate up to 10.9 %, and it appears that the difference is caused by the approximation process of the material property curve obtained experimentally, as

shown in figure 6.12. The model follows quite well the trends in the magnetic properties of magnetostrictive material, which means that the suitable intensity of the magnet can be easily selected by the model simulation to enhance the performance of the transducer.



[MPT Excitation]



[MPT Detection]

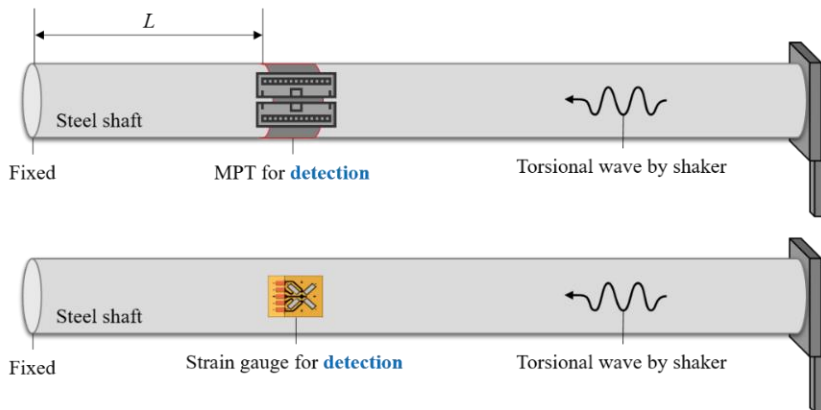


Fig. 6.1 Experimental configuration for comparison between the model and the actual magnetostrictive patch transducer. For excitation performance, the signal generated from the magnetostrictive patch transducer is converted to

a strain value through the strain gauge. For measurement performance, the signal from the shaker is measured simultaneously with the magnetostrictive patch transducer and the strain gauge to perform a quantitative comparison.

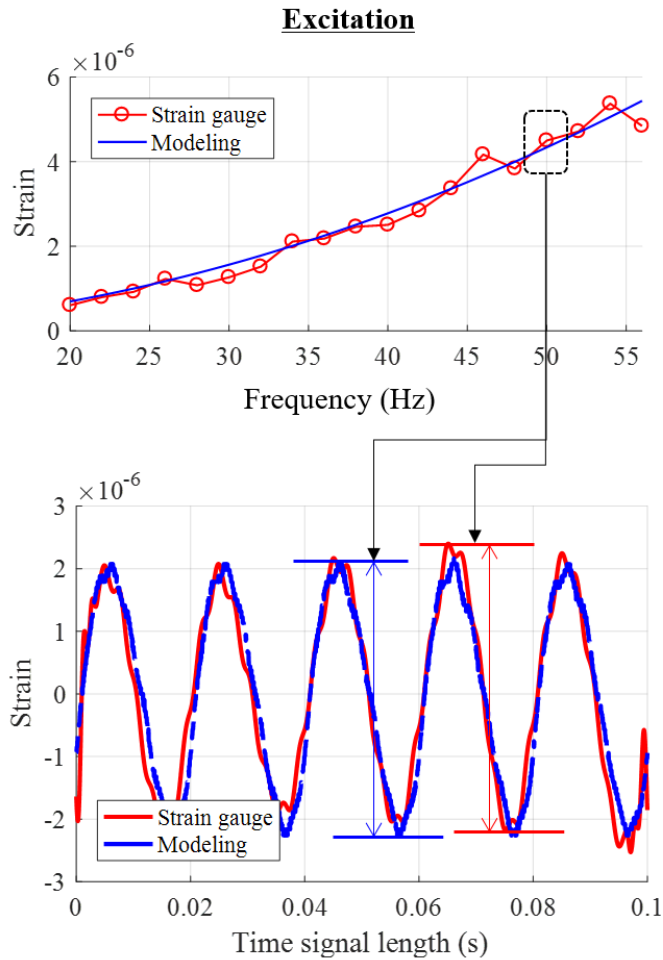


Fig. 6.2 Comparison of excitation performance in low-frequency range (20 ~ 55 Hz). The top graph shows the peak to peak values (red dots) of the measured signals and the value obtained from the model simulation (blue solid line) according to the frequencies, and the graph at the bottom compares the time signals at 50 Hz.

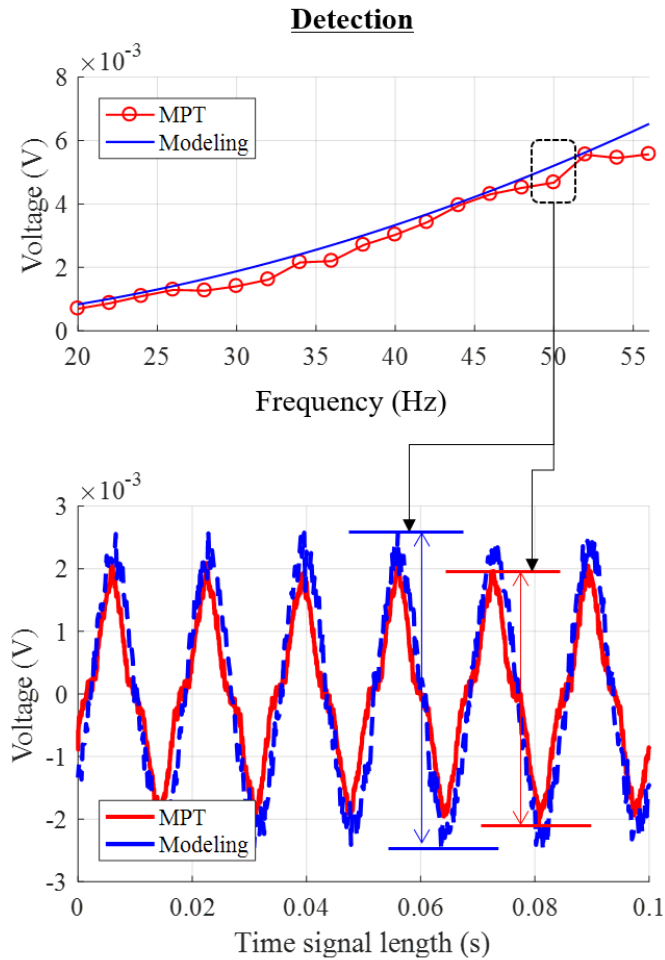


Fig. 6.3 Comparison of measurement performance in low-frequency range (20 ~ 55 Hz). The top graph shows the peak to peak values (red dots) of the measured signals and the value obtained from the model simulation (blue solid line) according to the frequencies, and the graph at the bottom compares the time signals at 50 Hz.

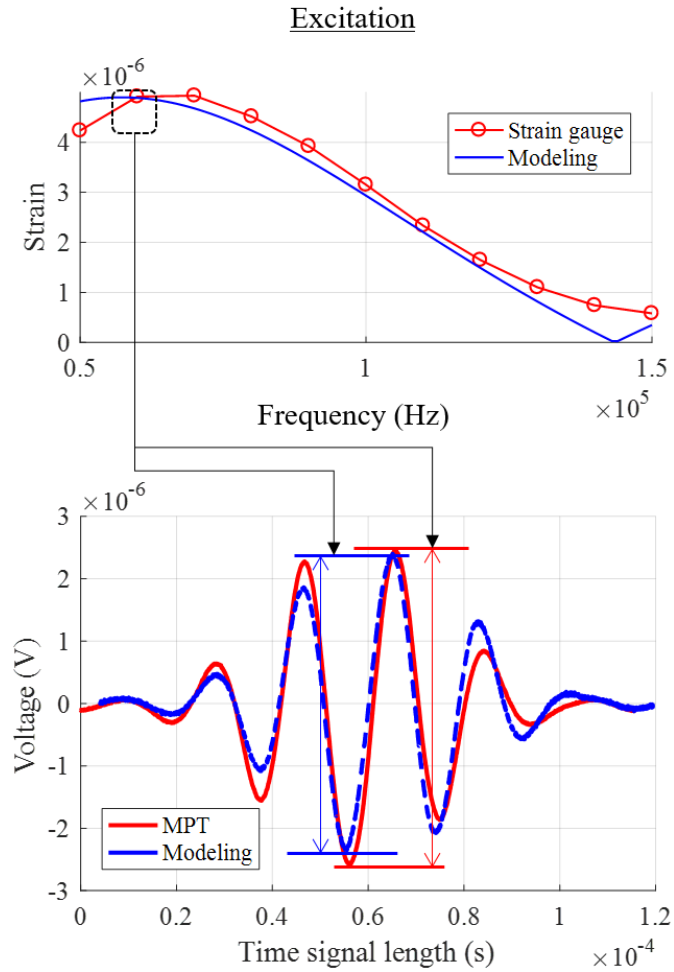


Fig. 6.4 Comparison of excitation performance in high-frequency range (50 ~ 150 kHz). The top graph shows the peak to peak values (red dots) of the measured signals and the value obtained from the model simulation (blue solid line) according to the frequencies, and the graph at the bottom compares the time signals at 60 kHz.

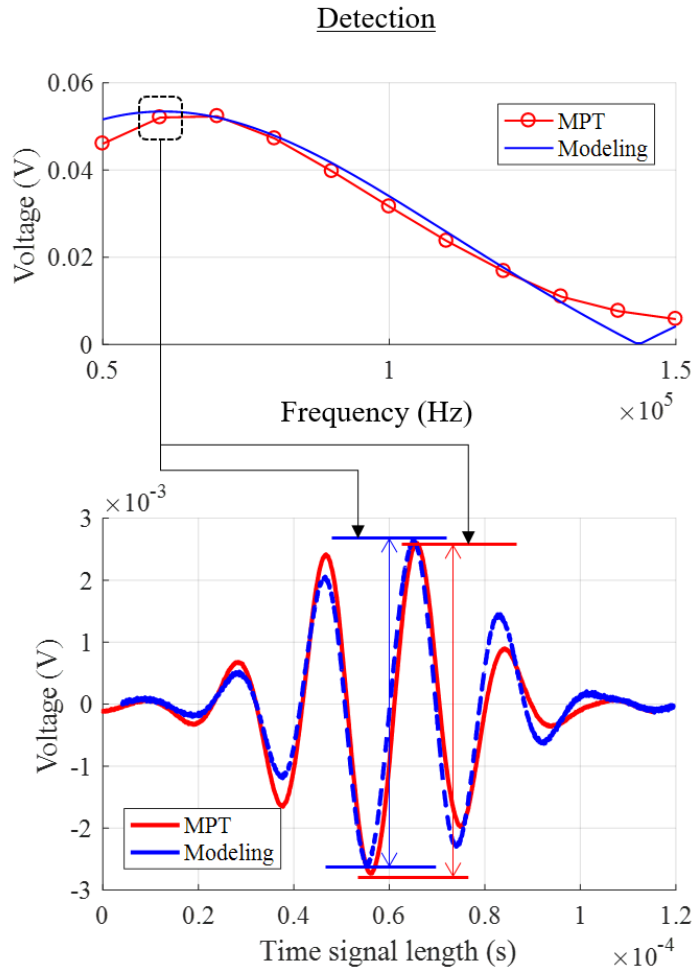


Fig. 6.5 Comparison of measurement performance in high-frequency range (50 ~ 150 kHz). The top graph shows the peak to peak values (red dots) of the measured signals and the value obtained from the model simulation (blue solid line) according to the frequencies, and the graph at the bottom compares the time signals at 60 kHz.

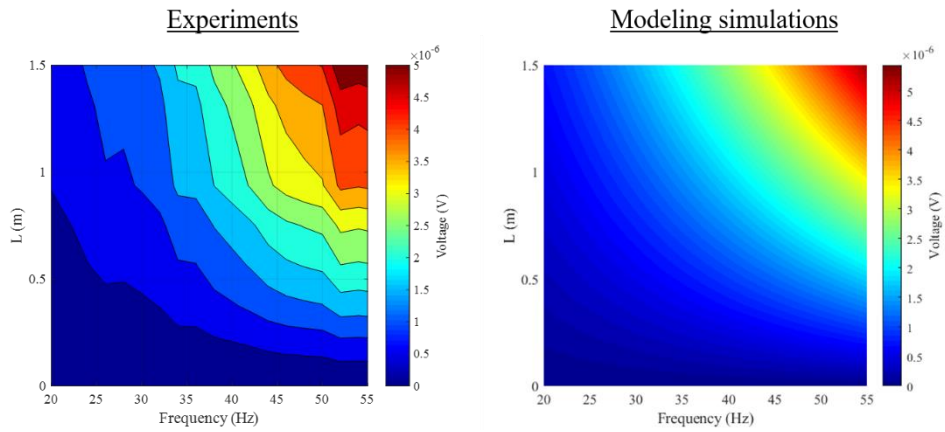


Fig. 6.6 Results for measured voltage values with distance from a shaker and frequency of a magnetostrictive patch transducer using a 25 mm wide patch attached to a steel solid shaft. (left) Low-frequency range measurement experiment, (right) low-frequency range model simulation.

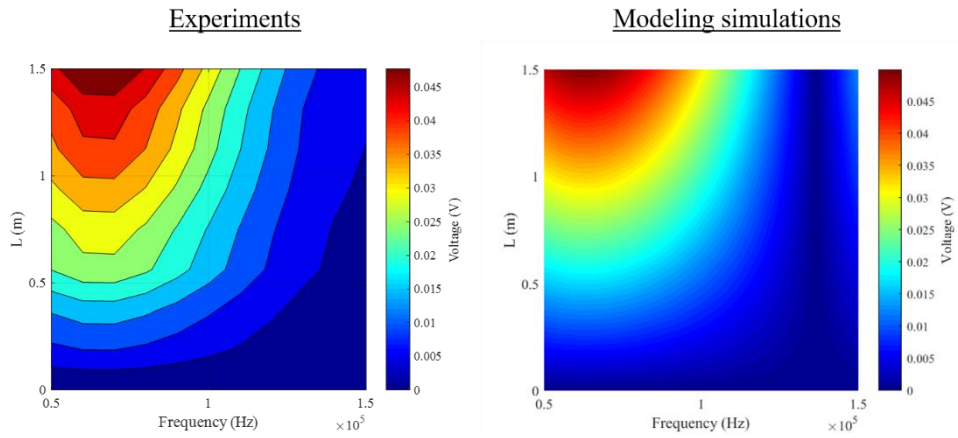


Fig. 6.7 Results for measured voltage values with distance from a shaker and frequency of a magnetostrictive patch transducer using a 25 mm wide patch attached to a steel solid shaft. (left) High-frequency range measurement experiment, (right) high-frequency range model simulation.

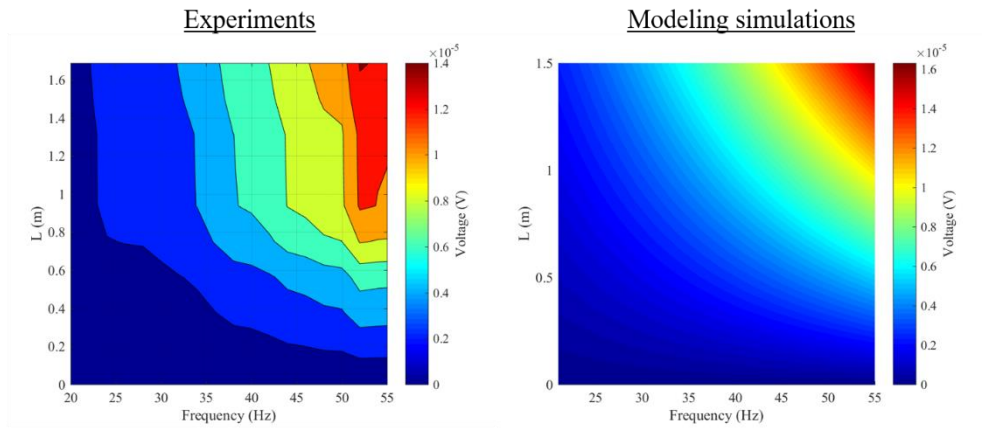


Fig. 6.8 Results for measured voltage values with distance from a shaker and frequency of a magnetostrictive patch transducer using a 25 mm wide patch attached to an aluminum solid shaft. (left) Low-frequency range measurement experiment, (right) low-frequency range model simulation.

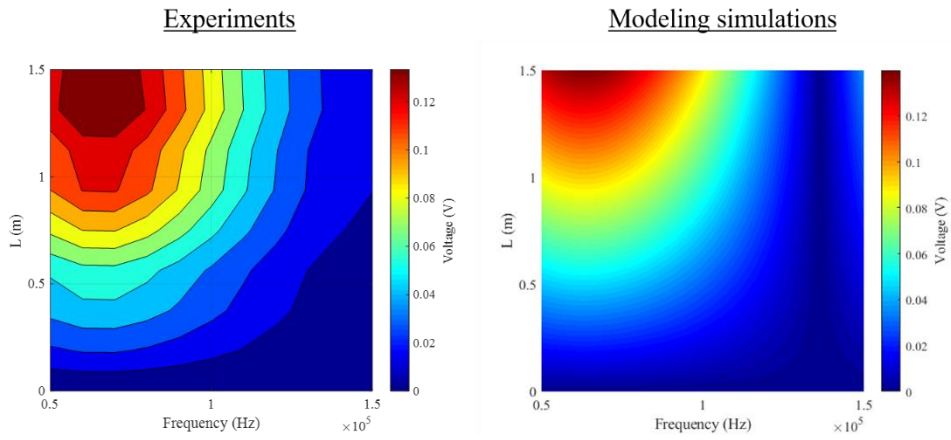


Fig. 6.9 Results for measured voltage values with distance from a shaker and frequency of a magnetostrictive patch transducer using a 25 mm wide patch attached to an aluminum solid shaft. (left) High-frequency range measurement experiment, (right) high-frequency range model simulation.

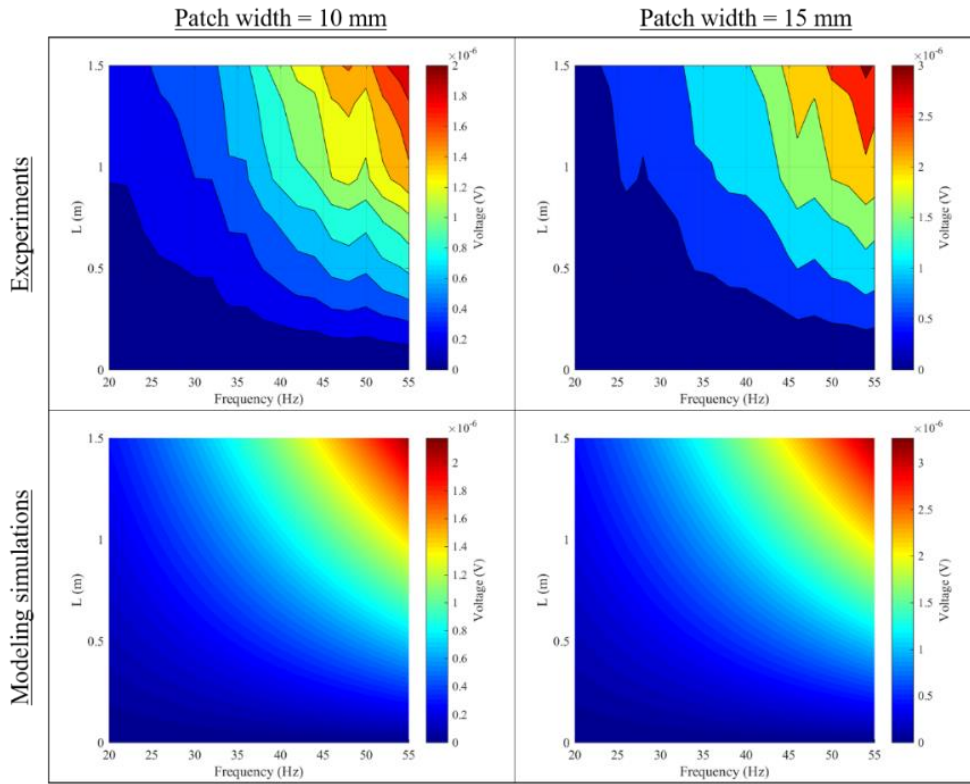


Fig. 6.10 Measurement results of the magnetostrictive patch transducer with 10 mm and 15 mm patch widths at low frequency range.

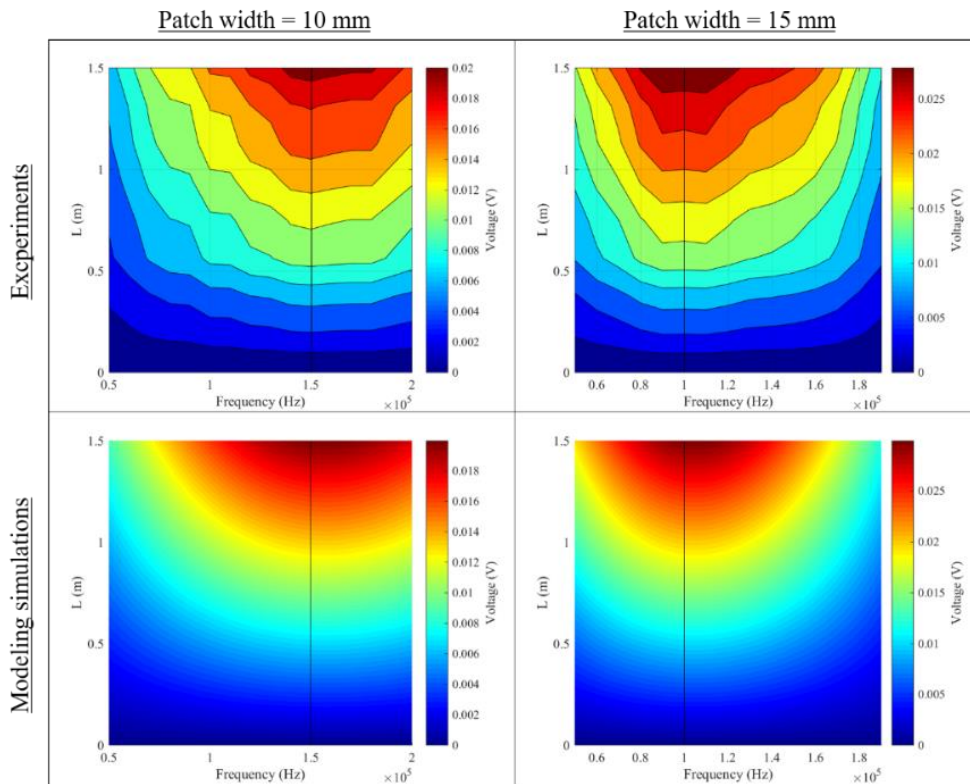


Fig. 6.11 Measurement results of the magnetostrictive patch transducer with 10 mm and 15mm patch widths and the first mode resonant frequency (black solid line) of patches at high frequency range.

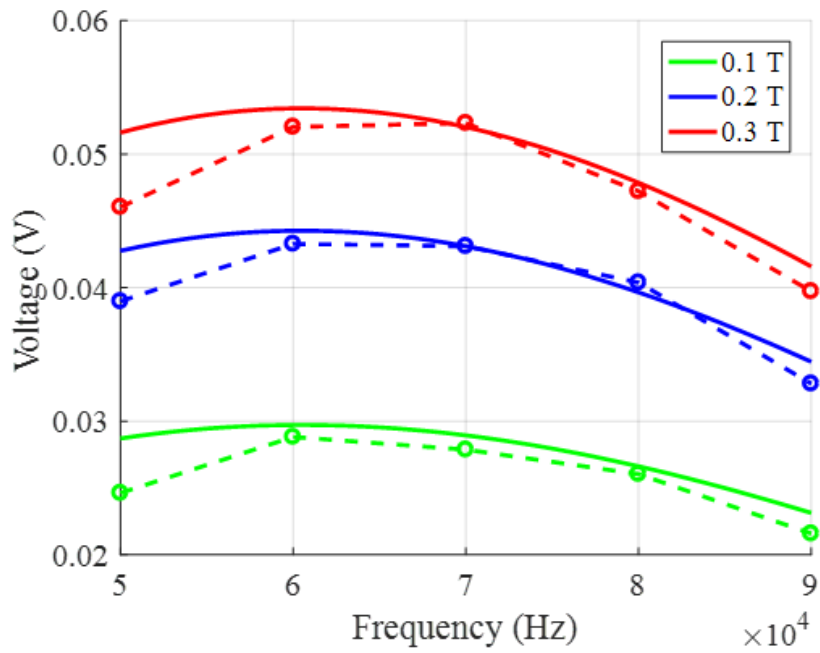


Fig. 6.12 Comparison of signal amplitude results from the model (solid line) and the experiment (dash-dotted line) according to the intensity of the permanent magnet.

CHAPTER 7.

CONCLUSIONS

Based on the aforementioned research, we could verify the reversible and quantified performance about both excitation and measurement of the magnetostrictive patch transducer through the improved model.

Before that, the linear equations for these magnetostriction phenomenon were introduced. And attempts to optimize some design parameters of magnetostrictive patch transducers through the corresponding equations were conducted. Furthermore, relative comparisons with previously validated strain gages with optimized magnetostrictive patch transducers were also done. Although the approach through linear equations allows a trend comparable to frequency or intensity only, the results show the potential for quantification of magnetostrictive patch transducers.

The fully coupled model is constructed considering the impedance of the specimen and the equipment very similar to the actual experiment configuration. In the case of the magnetostriction phenomenon model, the reversible response has been checked to be able to use in both excitation and measurement. By comparing the magnetostrictive patch transducer and the already quantified strain gauge, we could verify the performance of the proposed model, and the results of the proposed model show reasonable accuracy with the response value obtained by the experiments with

the error rates around 10 %.

On the other hand, during quantification, the electromagnetic characteristics such as hysteresis that are judged not to have a significant effect on the performance are omitted by the assumption. Furthermore, although the maximum error rate is measured to be approximately 10 %, in order to substitute the existing transducers used in the actual industrial field, the error rate should be reduced to within 10 % for absolute quantification. Therefore, for the model to have a higher level of perfection precision, these parts should be improved and will be complemented by further studies.

As mentioned above, we have dealt with the torsional magnetostrictive patch transducers used in cylindrical specimens. However, the proposed model can be applied to various types of magnetostrictive patch transducers as it has considered a structure of a specimen and that of a transducer. This verified model will facilitate the theoretical simulation for the experimental design using the magnetostrictive patch transducer and the quantification through the model is expected to be the solution in the industrial field where the magnetostrictive patch transducer's advantages can be maximized.

APPENDIX A.

MAGNETIC INTERFERENCES IN ULTRASONIC MAGNETOSTRICTIVE PATCH TRANSDUCERS

A.1 Overview

Magnetostriction is a phenomenon operated by coupling between magnetic and elastic fields. A transducer that can generate and measure ultrasonic waves using magnetostriction is called a magnetostrictive transducer [95]. Because magnetostrictive transducers are cost-effective and have simple structures, they have been widely used in non-destructive testing (NDT) [96-98] and structural health monitoring (SHM) applications [99, 100]. For generating and measuring ultrasonic waves, a magnetostrictive transducer uses magnetic fields. Thus, interferences among the magnetic fields generated by each transducer are unavoidable when multiple magnetostrictive transducers are used in close proximity. Similar issues exist in piezoelectric and electromagnetic acoustic transducers; some studies on the mutual interferences among these transducers have therefore been reported [101, 102]. However, mutual interferences among magnetostrictive transducers have not yet been researched. Because the mutual interferences cause difficulty in obtaining the desired data in experiments, research to minimize the effects of the interferences needs to be carried out. In this paper, omni-directional Lamb waves magnetostrictive

patch transducers (OL-MPTs) that can generate Lamb waves omni-directionally in a plate are used for investigating the mutual interferences among magnetostrictive transducers.

A.2 Analysis of the dynamic magnetic interference in a receiver

When an alternating current is sent into a circular coil in a transmitter, the dynamic magnetic field produced around the coil in the transmitter induces an electromotive force to a coil in a receiver. To investigate how much a cross-talk signal is affected by the value of L_{TR} due to the electromotive force, we performed a set of experiments on a paramagnetic aluminum plate and also on a non-ferromagnetic acrylic plate.

As illustrated in figure 2(a), two OL-MPTs were used as a transmitter and a receiver respectively, on a 1 mm thick aluminum plate. A printed circuit board (PCB) based OL-MPT was fabricated for the experiments and the photo of it is shown in figure 5(a). A circular nickel patch of 20 mm in diameter and 0.15 mm in thickness was used as a magnetostrictive patch and coupled by a shear couplant onto the plate. The permanent NdFeB magnet of 6 mm diameter and 3 mm height was located on the patch. The circular coil of 25 turns has an outer radius R_{out} of 10 mm which is the

same as the radius of the patch and an inner radius R_{in} of 6.5 mm.

From equation (1) and $D = 20$ mm, the wavelength λ is obtained as 13.3 mm. Considering the wavelength-frequency relation, this wavelength corresponds to the frequency of 400 kHz for a 1 mm thick aluminum plate. Thus, a Gabor pulse (see, e.g. [94]) centered at 400 kHz, shown in figure 6, was generated by a function generator (33250A, Agilent Technologies Inc., Santa Clara, Ca), amplified by a power amplifier (AG1017L, T&C Power Conversion, Rochester, NY), and transferred to the transmitter. The Gabor pulse, the modulated Gaussian pulse, is used because it has the best energy concentration both in time and in frequency. The signals measured by the receiver were then amplified by a pre-amplifier (SR560, Stanford Research Systems, Sunnyvale, CA) and saved by an oscilloscope (WaveRunner 620Zi, LeCroy, Chestnut Ridge, NY).

Varying the value of L_{TR} from 40 mm to 150 mm at intervals of 10 mm, the peak to peak voltages (V_{p-p}) of cross-talk signals were obtained and are denoted as the blue diamonds in figure 5(c). The result shows that the magnitude of a cross-talk signal decreases rapidly as L_{TR} increases. On an acryl plate, the same experiments were conducted and V_{p-p} of cross-talk signals were obtained. At $L_{TR} = 40$ mm, the V_{p-p} of the cross-talk signal in the acryl plate is 11.6 V, which is about 7.3 times

larger than the value in the aluminum plate. The difference in the cross-talk signals in acryl and aluminum plates under the same input pulse is due to the induced eddy current in aluminum, a conductive material. In case of the aluminum plate, the dynamic field induces an eddy current in it which in turn generates a magnetic field that opposes the incident the magnetic field. Consequently, the net magnetic field is decreased in the aluminum plate. Therefore, the cross-talk signal in the aluminum plate becomes smaller than that in the acryl plate.

In the previous experimental results, the magnitude of the cross-talk signal decreases as L_{TR} is increased. If possible, therefore, the magnitude of the cross-talk signal can be reduced efficiently by placing an appropriate distance between the transmitter and the receiver in an experimental setup. A semi-analytic analysis was thus conducted to qualitatively calculate the magnitude of a cross-talk signal by L_{TR} . Assuming that a test plate is non-ferromagnetic, a magnetic flux in the z -direction (B_z) generated by the receiver, when a current is sent to a circular coil in the transmitter, is given by [24]:

$$B_z = \int_{R_{in}}^{R_{out}} -\frac{\mu_0 I R^2}{4L_{TR}^3} \left(1 + \frac{3R^2}{L_{TR}^2} \right) dR \approx -\frac{\mu_0 I (R_{out}^3 - R_{in}^3)}{12L_{TR}^3} (\because R \ll L_{TR}) \quad (A.1)$$

Here, μ_0 denotes the air permeability, I denotes the current transmitted to a coil,

and R refers to the radius of a coil.

Because the current I is the only time-varying variable in equation (A.1), an induced electromotive force applied to a coil in a receiver can be derived from Faraday's Law [45] and written as:

$$v_{coil} = -\frac{\partial}{\partial t} \int_{R_{in}}^{R_{out}} B_z \pi R^2 dR \approx \frac{\alpha}{L_{TR}^3} \frac{\partial I}{\partial t} (\because R \ll L_{TR}), \quad (A.2)$$

where $\alpha = \mu_0 \pi (R_{out}^3 - R_{in}^3)^2 / 36$. Thus, an induced electromotive force (the magnitude of a cross-talk signal) is inversely proportional to $(L_{TR})^3$. To compare the experimental and the semi-analytical results, the fitted curve expressed as $y = c / x^3$ (c is a constant) is plotted in figure A.2. Although a paramagnetic plate absorbs a dynamic magnetic field in experiments, the measured cross-talk signals correspond well with equation (A.2).

While a cross-talk signal can be reduced by placing an appropriate distance between the transmitter and the receiver, this distance needs to be close if a specimen has a small area of inspection. In this case, we can consider the use of an electromagnetic shielding by placing a piece of thin aluminum foil on a circular coil in an OL-MPT to decrease the cross-talk; an eddy current induced in the aluminum foil by the

dynamic field of the transmitter helps decrease the net magnetic field applied to the receiver coil. The red circles in figure A.2(c) denote the magnitude of cross-talk signals measured by OL-MPTs with aluminum foil (the photo of which is also inserted in figure A.2(b)); we can observe here that the magnitude of the cross-talk signal decreases by a maximum of 81% at $L_{TR} = 40$ mm. Also, the magnitude of the cross-talk signal is still inversely proportional to $(L_{TR})^3$ even though with aluminum foil.

A.3 Analysis of the static magnetic interference between adjacent transmitters

When multiple transmitters are used in close proximity, static magnetic fields generated by magnets of adjacent transmitters interfere with the transmitter that generates Lamb waves, and the resulting interference affects the generated waves by the transmitter. To investigate the effect of the interference, an external magnet and a patch were located near the transmitter as shown in figure A.1(b). The experiment was then set up in order to measure the magnitude of Lamb waves depending on the center-to-center distance L_{TT} and the angle θ between the transmitter and the external magnet. The permanent NdFeB magnet (0.4 Tesla) with 6 mm in diameter and 10 mm in height which is larger than the magnet used in the transducer was utilized to increase the effect of the static magnetic interference for more pronounced

results.

Varying the values of L_{TT} from 25 mm to 35 mm at intervals of 5 mm and the values of θ from 0° to 180° at intervals of 10° , the magnitudes of Lamb waves were measured and normalized by the magnitude of Lamb waves measured without the external magnet. The results are shown in figure A.4(a). According to the radiation pattern at $L_{TT} = 25$ mm, the normalized magnitude is less than 1 at ranges of $0^\circ \sim 50^\circ$ while the normalized magnitude is larger than 1 at ranges of $60^\circ \sim 90^\circ$. Also, the radiation patterns converge to 1 as L_{TT} increases. This is because the effect of the static magnetic interferences had reduced.

The observations found out from the experiments can be explained analytically with the magnetostrictive equation, as mentioned in Chapter 3, as follows [71]:

$$\mathbf{S} = \mathbf{sT} + \mathbf{d}^T \mathbf{H}_D, \quad (\text{A.3})$$

$$\mathbf{B}_D = \mathbf{dT} + \mu \mathbf{H}_D, \quad (\text{A.4})$$

where \mathbf{S} , \mathbf{H}_D , \mathbf{T} , and \mathbf{B}_D denote the engineering strain defined as $\mathbf{S} = [S_{xx} \ S_{yy} \ S_{zz} \ S_{yz} \ S_{xz} \ S_{xy}]^T$, the dynamic magnetic field defined as $\mathbf{H}_D = [H_{D_x} \ H_{D_y} \ H_{D_z}]^T$, the stress, and the dynamic magnetic flux density,

respectively. Also, s is the compliance, \mathbf{d} is the piezomagnetic coupling matrix, and μ is the permeability. Equations (A.3) and (A.4) are coupled by \mathbf{d} . For very small magnetostriction, however, the values of components of \mathbf{d} are relatively smaller than the values of s and μ ; equations (A.3) and (A.4) can be treated as individual equations. Thus one can assume that Lamb waves are generated only by the second term of equation (A.3). Therefore, a strain due to magnetostriction can be considered as follows [71]:

$$\mathbf{S}_{MS} = \mathbf{d}^T \mathbf{H}_D. \quad (\text{A.5})$$

When the static magnetic field \mathbf{H}_S is induced in the x -direction, \mathbf{d} can be written in the following form [71]:

$$\mathbf{d} = \begin{bmatrix} d_{11} & d_{12} & d_{12} & 0 & 0 & 0 \\ 0 & 0 & 0 & 0 & 0 & d_{35} \\ 0 & 0 & 0 & 0 & d_{35} & 0 \end{bmatrix}. \quad (\text{A.6})$$

Here, the components of \mathbf{d} are defined as $d_{11} = \left. \frac{\partial f(H)}{\partial H} \right|_{H_S}$, $d_{12} = -0.5d_{11}$, and

$d_{35} = 3 \frac{f(H_s)}{H_s}$. The function $f(H)$ is a magnetostriction curve [28], which shows the relation between the magnetic field strength and the strain in a magnetostrictive material. The symbol H represents a magnetic field strength ($|\mathbf{H}|$).

Without the static magnetic interference by an external magnet, the static magnetic fields \mathbf{H}_s and \mathbf{H}_D applied to the patch are generated along the radial direction as shown in figure A.5(a). When an external magnet is placed near the transmitter, however, the strength and the direction of \mathbf{H}_s change and then the new static magnetic field \mathbf{H}_s is formed as shown in figure A.5(b). Using the harmonic analysis simulated by COMSOL Multiphysics [43], the strength of \mathbf{H}_s (H_s) distributed on the patch area covered with the coil were obtained. Substituting these values into equation (A.6), the components of \mathbf{d} in the local coordinate system (x', y', z') shown in figure A.5(b) can be calculated. We denote these values as $(d_{1'1'}, d_{2'2'}, d_{3'5'})$, respectively. Because the patch is only 0.15 mm thick, the z component of the static magnetic field in the patch is negligible and the distribution of the static magnetic field can be assumed to be a two-dimensional field in the x - y plane [109]. Then, \mathbf{S}_{MS} in the local coordinate system (x', y', z') expressed by the components of \mathbf{d} calculated above is written as follows:

$$\mathbf{S}_{MS'} = \begin{Bmatrix} S_{x'x'} \\ S_{y'y'} \\ S_{x'y'} \end{Bmatrix} = \begin{Bmatrix} d_{1'1'} H_D \cos \phi \\ d_{1'2'} H_D \cos \phi \\ d_{3'5'} H_D \sin \phi \end{Bmatrix}. \quad (\text{A.7})$$

The dominant Lamb wave which reaches the receiver can be assumed to be generated by the x -direction deformation because L_{TR} is much larger than the radius of the transducer. Therefore, by the coordinate transformation from the local coordinate system (x', y', z') to the global coordinate system (x, y, z) , S_{xx} (the normal strain component in the x -direction) is obtained from $\mathbf{S}_{MS'}$ as:

$$S_{xx} = d_{1'1'} H_D \cos^3 \phi + (d_{1'2'} + d_{3'5'}) H_D \sin^2 \phi \cos \phi \quad (\text{A.8})$$

where ϕ is the angle between the x and x' coordinates.

When an external magnet and a patch are located along the η -direction (see figure A.5(b)), the radiation pattern of S_{xx} is shown in figure A.6. The symbols S_{xx}^A and S_{xx}^B in figure 8 denote the strain S_{xx} values at points A and B, respectively, which are placed on the x -axis shown in figure A.5(b). The magnitude of the Lamb wave

measured by the receiver located on the x -axis is proportional to the averages of both S_{xx}^A and S_{xx}^B . Therefore, the variance ratios of Lamb waves by θ can be calculated by normalizing the averages of both S_{xx}^A and S_{xx}^B with the value of S_{xx} measured without an external magnet.

The normalized magnitudes of Lamb waves by θ at $L_{TT} = 25, 30, \text{ and } 35$ mm are shown in figure A.4(b). The results are in good agreement with the experimental results shown in figure A.4(a). Figure A.4(c) shows the experimental and the semi-analytical variance ratios of Lamb waves caused by the effect of the static magnetic interference. These results have only 3.53%, 0.95% and 0.97% maximum error rates for $L_{TT} = 25, 30, \text{ and } 35$ mm, respectively. Thus, the validity of the proposed semi-analytical method is successfully verified from the experimental results. There are two major causes of error in these results; the assumptions used to obtain the components of \mathbf{d} in equations (A.4) and (A.5), and the difference between the magnetostriction curve used in this research and the actual magnetostriction curve of the nickel patch.

As mentioned in section 1.2, an OL-MPT generates the largest Lamb waves when λ and D satisfy equation (1). Therefore, D should be calculated from equation (1) after calculating λ from the wavelength-frequency relation in a test plate. Accordingly, D needs to be changed depending on the desired frequency and the

effect of the static magnetic interference by L_{TT} also changes because the radius of a coil varies with D . For this reason, it is necessary to obtain the distance at which the static magnetic interference among transmitters is negligible when multiple OL-MPTs are used in various frequencies. To this end, standards with respect to the negligible variance ratio are needed; we determined two standards as follows:

- 1) The distance of limit L_{limit} between two adjacent transmitters is defined as the minimum distance at which the maximum variance ratio of Lamb waves is less than a certain ratio, here, 3%.
- 2) The outer and inner radii of the coil is proportional to D .

In the previous analysis, the external magnet was larger than the magnet of the transmitter to increase the effect of the interference. Here, the same magnet as the magnet of the transmitter is used for the external magnet to obtain L_{limit} . The range of D is chosen to be $17 \text{ mm} \leq D \leq 23 \text{ mm}$ because the magnet of the transmitter for the present study is optimized for the patch of 20 mm in diameter. The values of L_{limit} calculated from the simulation are marked by circles in figure A.7. The fitted curve which approximates L_{limit} and D in the linear relation can be obtained as:

$$L_{\text{limit}} = 0.8D + 6.5 \quad (17 \text{ mm} \leq D \leq 23 \text{ mm}). \quad (\text{A.9})$$

As a result, once the frequency of the Lamb wave is determined, L_{limit} can be estimated by using equations (1) and (9).

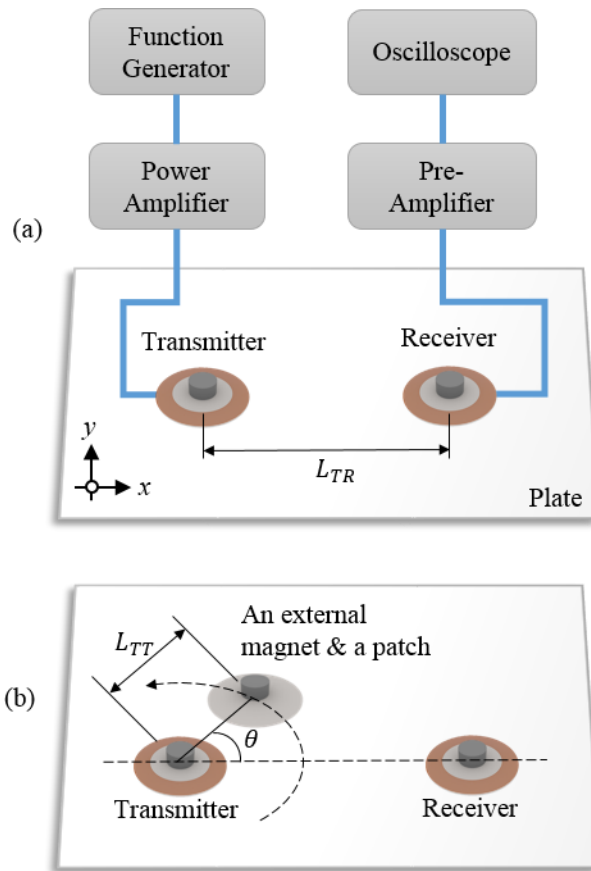


Fig. A.1 Experimental setups (a) for measurement of a cross-talk signal and (b) for investigation of the mutual interference caused by a static magnetic field.

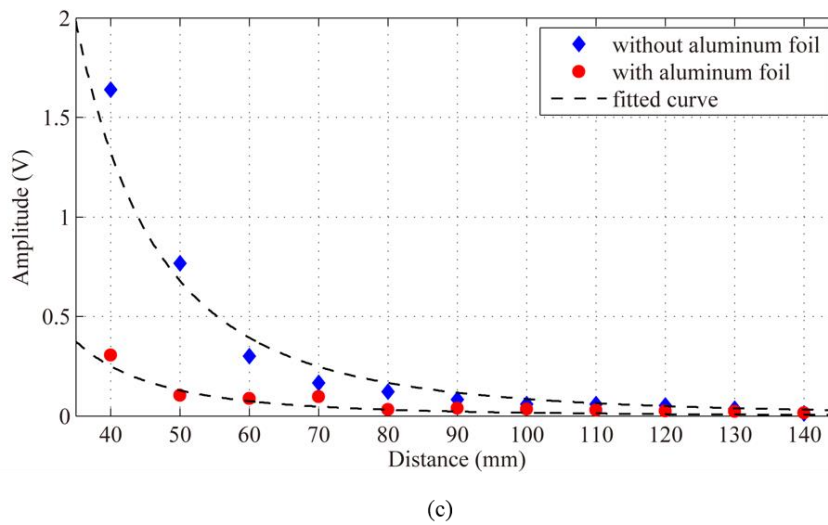
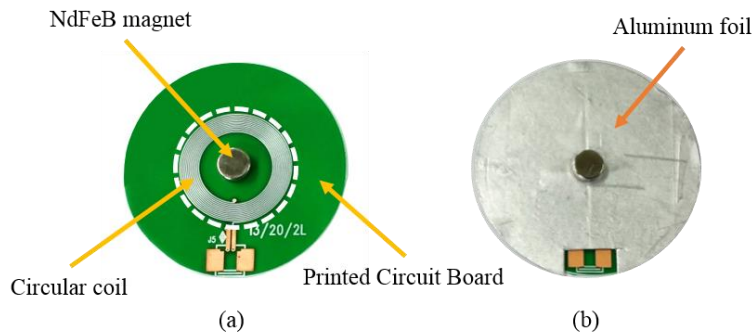


Fig. A.2 (a) Photo of the developed PCB based OL-MPT. The nickel patch (not shown) is located under the dashed circle. (b) The OL-MPT shielded by aluminum foil. (c) The cross-talk signals of the OL-MPT without aluminum foil (blue diamonds) and of the OL-MPT with aluminum foil (red circles) installed on an aluminum plate.

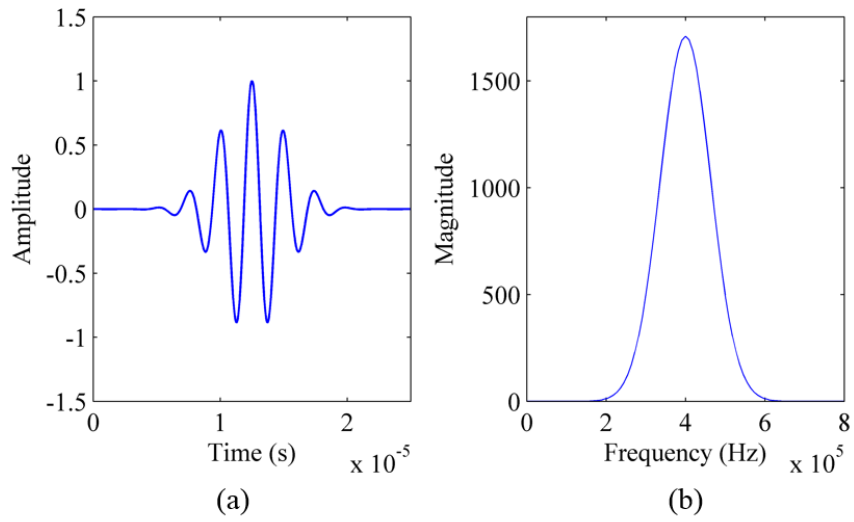


Fig. A.3 The Gabor pulse centered at 400 kHz used as the excitation signal, plotted in (a) the time and (b) frequency domains.

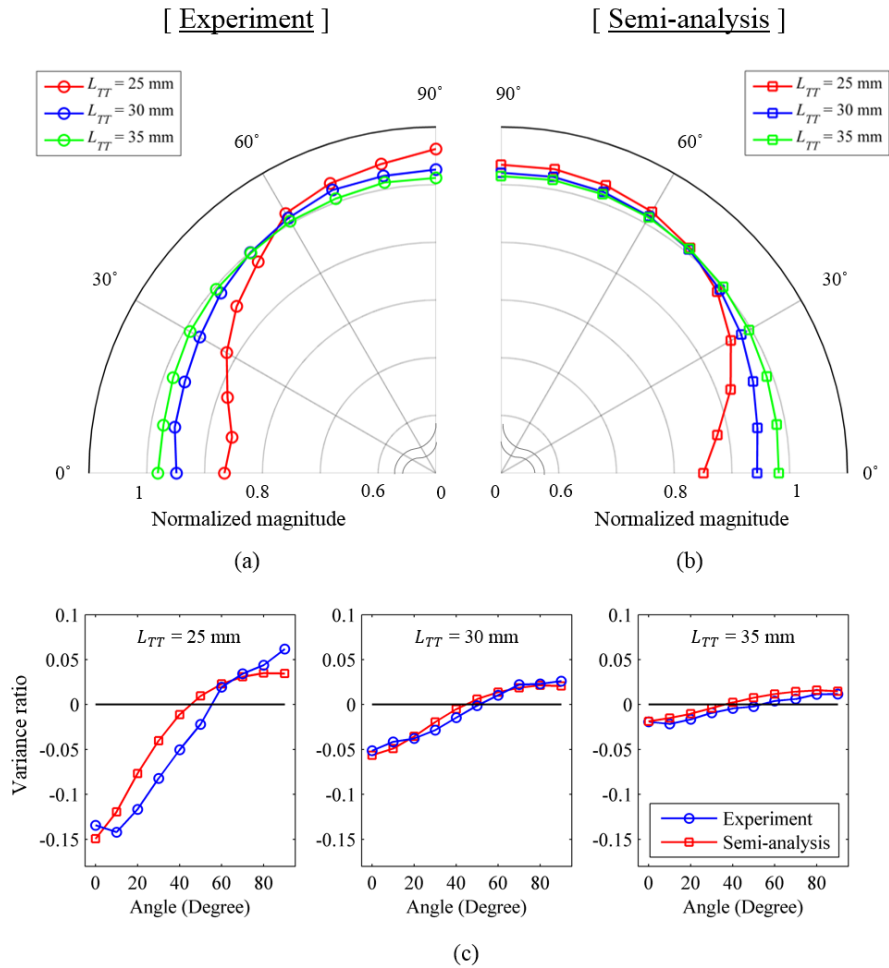


Fig. A.4 Radiation patterns of the normalized magnitudes of Lamb wave signals obtained (a) from the experiments, (b) from the semi-analytic analysis and (c) variance ratios of the normalized magnitudes of Lamb wave signals obtained from the experiments (blue line with circles) and the semi-analytic analysis (red line with rectangles).

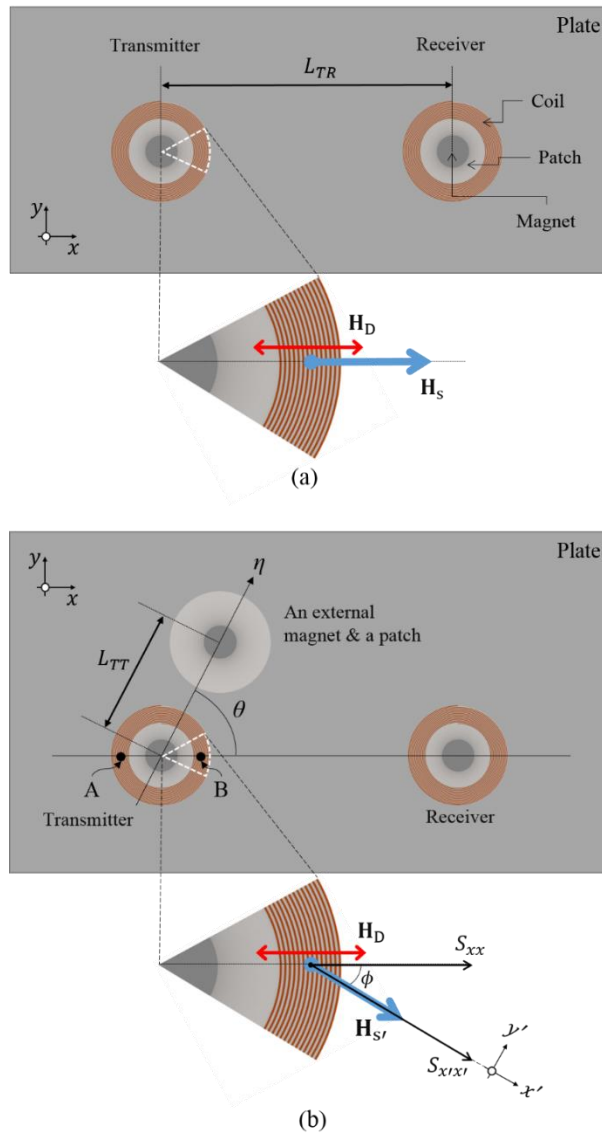


Fig. A.5 Schematic illustrations of magnetic fields distributions in the transmitter (a) without and (b) with an external magnet and a magnetostrictive patch for the magnetic interference.

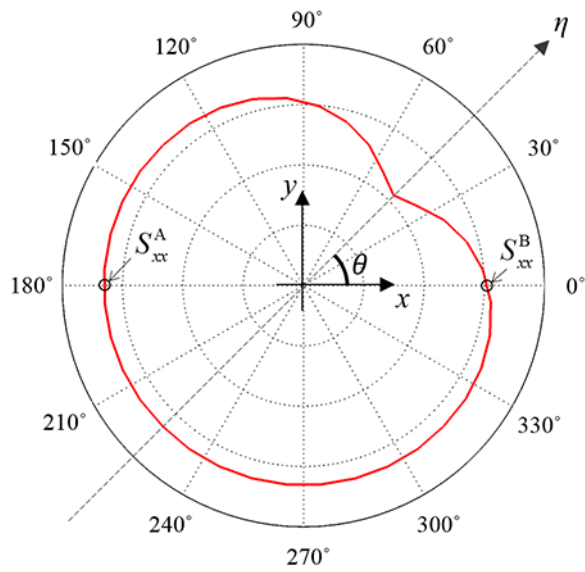


Fig. A.6 Radiation pattern of strain S_{xx} when a receiver is located on the x axis and an external magnet and a patch are located on the η direction.

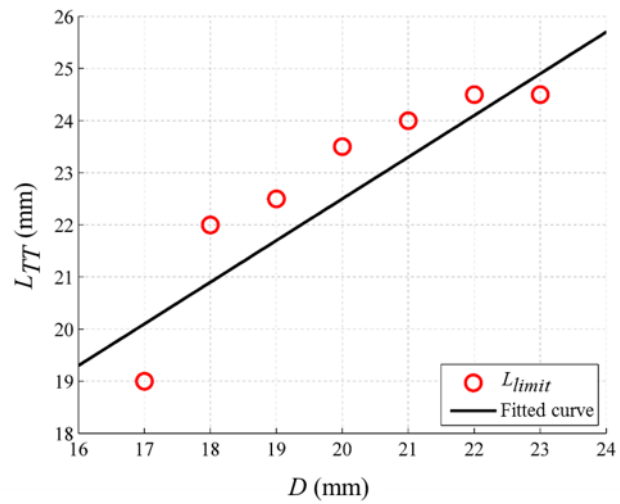


Fig. A.7 Relation of the distance of limit L_{limit} and the patch diameter D .

The fitted curve refers to the linear relation between them.

REFERENCES

- [1] H. Kwun and K.A. Bartels, Magnetostrictive sensor technology and its applications, *Ultrasonics* 36 (1998) 171-178.
- [2] E. Kannan, B.W. Maxfield and K. Balasubramaniam, SHM of pipes using torsional waves generated by in situ magnetostrictive tapes, *Smart Mater. Struct.* 16 (2007) 2505-2515.
- [3] J.S. Lee, H.W. Kim, B.C. Jeon, S.H. Cho and Y.Y. Kim, Damage Detection in a Plate Using Beam-Focused Shear-Horizontal Wave Magnetostrictive Patch Transducers, *AIAA J.* 48 (2010) 654-663.
- [4] Y. Y. Kim and Y. E. Kwon. Review of magnetostrictive patch transducers and applications in ultrasonic nondestructive testing of waveguides. *Ultrasonics* 62 (2015) 3-19.
- [5] H. M. Seung, H. W. Kim and Y. Y. Kim. Development of an omnidirectional shear-horizontal wave magnetostrictive patch transducer for plates. *Ultrasonics* 53 (2013) 1304-1308.
- [6] C. I. Park, S.H. Cho and Y.Y. Kim, Z-shaped magnetostrictive patch for efficient transduction of a torsional wave mode in a cylindrical waveguide, *Appl. Phys. Lett.* 87 (2005) 224105.
- [7] J.S. Lee, Y.Y. Kim and S.H. Cho, Beam-focused shear-horizontal wave

- generation in a plate by a circular magnetostrictive patch transducer employing a planar solenoid array, *Smart Mater. Struct.* 18 (2009) 015009.
- [8] H.W. Kim, Y.E. Kwon, J.K. Lee and Y.Y. Kim, Higher torsional mode suppression in a pipe for enhancing the first torsional mode by using magnetostrictive patch transducers, *IEEE Trans. Ultrason. Ferroelectr. Control* 60 (2013) 562-572.
- [9] J.K. Lee, H. M. Seung, C. I. Park, J.K. Lee, D. H. Lim and Y. Y. Kim. Magnetostrictive patch sensor system for battery-less real-time measurement of torsional vibrations of rotating shafts. *JSV* 414 (2018) 245-258.
- [10] S. W. Han, H. C. Lee and Y. Y. Kim, "Noncontact Damage Detection of a Rotating Shaft Using the Magnetostrictive Effect," *Journal of Nondestructive Evaluation* 22 (2003) 141-150
- [11] S. H. Cho, S. W. Han, C. I. Park, and Y. Y. Kim, "Noncontact Torsional Wave Transduction in a Rotating Shaft Using Oblique Magnetostrictive Strips," *J. App. Phys.* 100 (2006) 104903
- [12] H. A. Tilmans. Equivalent circuit representation of electromechanical transducers: I. Lumped-parameter systems. *J. Micromech. Microeng.* 6

(1996) 157.

- [13] A. Raghavan and C. Cesnik. Finite-dimensional piezoelectric transducer modeling for guided wave based structural health monitoring. *Smart Mater. Struct.* 14 (2005) 1448.
- [14] F. Qian, W Zhou, S Kaluvan, H Zhang and L. Zuo. Theoretical modeling and experimental validation of a torsional piezoelectric vibration energy harvesting system. *Smart Mater. Struct.* 27 (2018) 045018.
- [15] M. Irfan and T. Uchimura. Development and performance evaluation of disk-type piezoelectric transducer for measurement of shear and compression wave velocities in soil. *J. Earthq. Eng.* 22 (2018) 147-171.
- [16] T. Yan, P. Theobald and B. E. Jones. A self-calibrating piezoelectric transducer with integral sensor for in situ energy calibration of acoustic emission. *Ndt. & E. Inter.* 35 (2002) 459-464.
- [17] D. Davino, A. Giustiniani and C. Visone. A two-port nonlinear model for magnetoelastic energy-harvesting devices. *IEEE Trans. Ind. Elec.* 58 (2011) 2556.
- [18] D. Davino, P. Krejci and C. Visone. Fully coupled modeling of magneto-mechanical hysteresis through thermodynamic compatibility. *Smart Mater. Struct.* (2013) 095009.

- [19] A. Viola, V. Franzitta, V. Di Dio, F. M. Raimondi and M. Trapanese. A magnetostrictive electric power generator for energy harvesting from traffic: Design and experimental verification. *IEEE Trans. Mag.* (2015) 8208404.
- [20] S. Cao, P. Zhang, J. Zheng, Z. Zhao and B. Wang. Dynamic nonlinear model with eddy current effect for stress-driven galferol energy harvester. *IEEE Trans. Mag.* 51 (2015a) 1-4.
- [21] B. Yan, C. Zhang, and L. Li. Design and fabrication of a high-efficiency magnetostrictive energy harvester for high-impact vibration systems. *IEEE Trans. Mag.* 51 (2015) 1-4.
- [22] M. S. Choi, S. Y. Kim and H. Kwun. An equivalent circuit model of magnetostrictive transducers for guided wave applications. *J. Korean Phys. Soc.* 47 (2005) 454-462.
- [23] C. S. Clemente, A. Mahgoub, D. Davino, C. Visone. Multiphysics circuit of a magnetostrictive energy harvesting device. *JIMSS* 28 (2017) 2317-2330.
- [24] H. Han, K. Lee and S. Park. Estimate of the fatigue life of the propulsion shaft from torsional vibration measurement and the linear damage summation law in ships. *Ocean Eng.* 107 (2015) 212-221
- [25] H. S. Han, K. H. Lee and S. H. Park. Parametric study to identify the

causes of high torsional vibration of the propulsion shaft in the ship.

Engineering Failure Analysis 59 (2015) 334-346

- [26] <http://www.carttech.com>
- [27] J.P. Joule, XVII. On the effects of magnetism upon the dimensions of iron and steel bars, *Philos. Mag. Ser. 3* 30 (1847) 76–87.
- [28] E. Villari. Ueber die aenderungen des magnetischen moments, welche der zugund das hindurchleiten eines galvanischen stroms in einem stabe von stahloder eisen hervorbringen. *Ann. Phys.* 202 (1865) 87–122.
- [29] S. Roman. Matteucci effect: its interpretation and its use for the study of ferromagnetic matter. *J. App. Phys.* 35 (1964) 1213-1216.
- [30] G. Wiedemann. Magnetische Untersuchungen. *Ann. Phys.* 193 (1862) 193–217.
- [31] G. Engdahl and I. D. Mayergoz. Handbook of giant magnetostrictive materials. Vol. 107. San Diego: Academic press, 2000.
- [32] G. Ping and Musa Jouaneh. Generalized Preisach model for hysteresis nonlinearity of piezoceramic actuators. *Precis. Eng.* 20.2 (1997) 99-111.
- [33] Pry, R. H. and C. P. Bean. Calculation of the energy loss in magnetic sheet materials using a domain model. *J. App. Phys.* 29.3 (1958) 532-533.
- [34] D. C. Jiles. and L. A. David. Theory of ferromagnetic hysteresis. *J. Mag.*

- Mag. Mater. 61.1-2 (1986) 48-60.
- [35] K. F. Graff. Wave motion in elastic solids. Courier Corporation, 2012.
- [36] K.H. Sun, S.H. Cho and Y.Y. Kim, Topology design optimization of a magnetostrictive patch for maximizing elastic wave transduction in waveguides, IEEE Trans. Magn. 44 (2008) 2373–2380.
- [37] H.J. Kim, J.S. Lee, H.W. Kim, H.S. Lee and Y.Y. Kim, Numerical simulation of guided waves using equivalent source model of magnetostrictive patch transducers, Smart Mater. Struct. 24 (2015) 015006.
- [38] K.S. Kannan. A. Dasgupta. A nonlinear Galerkin finite-element theory for modeling magnetostrictive smart structures. Smart Mater. Struct. 6 (1997) 341–350.
- [39] M. J. Dapino, R. C. Smith, L. E. Faidley and A. B. Flatau. A coupled structuralmagnetic strain and stress model for magnetostrictive transducers, J. Intell. Mater. Syst. Struct. 11 (2000) 135–152.
- [40] J. Kim, E. Jung, Finite element analysis for acoustic characteristics of a magnetostrictive transducer, Smart Mater. Struct. 14 (2005) 1273–1280.
- [41] X.J. Zheng, X.E. Liu, A nonlinear constitutive model for Terfenol-D rods, J. Appl. Phys. 97 (2005) 053901.
- [42] S. Valadkhan, K. Morris, A. Khajepour, Review and comparison of

- hysteresis models for magnetostrictive materials, *J. Intell. Mater. Syst. Struct.* 20 (2009) 131–142.
- [43] R. Ribichini, F. Cegla, P.B. Nagy, P. Cawley, Quantitative modeling of the transduction of electromagnetic acoustic transducers operating on ferromagnetic media, *IEEE Trans. Ultrason. Ferroelectr. Freq. Control* 57 (2010) 2808–2817.
- [44] M. Hirao, H. Ogi, EMATs for science and industry: noncontacting ultrasonic measurements, Kluwer Academic Publishers, Boston, 2003.
- [45] D.K. Cheng. *Field and wave electromagnetics*. Pearson Education, India, 1989.
- [46] S. W. Han, H. C. Lee and Y. Y. Kim. Noncontact damage detection of a rotating shaft using the magnetostrictive effect *Journal of Nondestructive Evaluation* 22 (2003) 141-150.
- [47] R. B. Thompson. Generation of horizontally polarized shear waves in ferromagnetic materials using magnetostrictively coupled meander-coil electromagnetic *Appl. Phys. Lett.* 34 (1978) 175–177.
- [48] R. Murayama, Driving mechanism on magnetostrictive type electromagnetic acoustic transducer for symmetrical vertical-mode Lamb wave and for shear horizontal-mode plate wave. *Ultras.* 34 (1996) 729-736.

- [49] G. Srinivasan, E. T. Rasmussen, J. Gallegos, R. Srinivasan, Yu. I. Bokhan, and V. M. Laletin. Magnetolectric bilayer and multilayer structures of magnetostrictive and piezoelectric oxides. *Physical Review B* 64.21 (2001) 214408.
- [50] J. Mora, A. Diez, J.L. Cruz, M.V. Andres. A magnetostrictive sensor interrogated by fiber gratings for DC-current and temperature discrimination. *IEEE Photo. Tech. Lett.* 12.12 (2000) 1680-1682.
- [51] A. G. Jenner, R. J. E. Smith, A. J. Wilkinson, R. D. Greenough. Actuation and transduction by giant magnetostrictive alloys. *Mechatron.* 10.4-5 (2000) 457-466.
- [52] J. H. Oh, K. H. Sun and Y. Y. Kim. Time-harmonic finite element analysis of guided waves generated by magnetostrictive patch transducers. *Smart Mater. Struct.* 22 (2013) 085007.
- [53] H. J. Kim, J. S. Lee, H. W. Kim, H. S. Lee and Y. Y. Kim. Numerical simulation of guided waves using equivalent source model of magnetostrictive patch transducers. *Smart Mater. Struct.* 24 (2015) 015006.
- [54] J. K. Lee, J. K. Lee and Y. Y. Kim. Analysis of magnetic interferences in ultrasonic magnetostrictive patch transducers. *Smart Mater. Struct.* 24 (2016) 085026.

- [55] R. Z. Levitin, V. N. Milov, Yu. F. Popov, V. V. Snegirev. Magnetostriction measurements under high magnetic fields by a piezoelectric transducer glued on the sample. *Physica B*. 177.1-4 (1992) 59-62.
- [56] R. Ribichini, P. B. Nagy, and H. Ogi. The impact of magnetostriction on the transduction of normal bias field EMATs. *Ndt. & E. Inter.* 51 (2012) 8-15.
- [57] <https://magweb-website-magwebusa.netdna-ssl.com>
- [58] COMSOL Multiphysics, COMSOL Multiphysics User's Guide: Version 4.3, COMSOL AB, Stockholm, May 2012.
- [59] R. D. Blevins. *Formulas for natural frequency and mode shape*. Kreiger Publ. Comp. New York. 1979.
- [60] J. D. Turner. Development of a rotating-shaft torque sensor for automotive applications. *IEE Proceedings D. (Control Theory and Applications)*. IET Digital Library, (1988) 334-338.
- [61] M. H. Muftah, S. M. Haris. A strain gauge based system for measuring dynamic loading on a rotating shaft. *Int. J. Mech.* 5.1 (2011) 19-26.
- [62] S. L. Bill, W. A. Pittman, D. P. Swartz, A. A. Sweet. Telemetry based shaft torque measurement system for hollow shafts. U.S. Patent No. 5,837,909. 17 Nov. 1998.

- [63] N. Bachschmid and E. Tanzi. Deflections and strains in cracked shafts due to rotating loads: a numerical and experimental analysis. *Int. J. Rot. Mach.* 10.4 (2004) 283-291.
- [64] M. Suster, N. Chaimanonart, J. Guo, W.H. Ko, D.J. Young. Remote-powered high-performance strain sensing microsystem. 18th IEEE Int. Con. Mic. Electro. Mech. Sys. (2005).
- [65] A. A. Gubran, J. K. Sinha. Shaft instantaneous angular speed for blade vibration in rotating machine. *Mech. Sys. & Sig. Proc.* 44.1-2 (2014) 47-59.
- [66] H. Sussman and S. L. Ehrlich. Evaluation of the magnetostrictive properties of Hiperco. *JASA* 22 (1950) 4.
- [67] M. M. Radmanesh. *The Gateway to Understanding: Electrons to Waves and Beyond*. AuthorHouse. 2005.
- [68] C. Caloz and T. Itoh. *Electromagnetic metamaterials: transmission line theory and microwave applications*. John Wiley & Sons, 2005.
- [69] W. J. R. Hoefer. The transmission-line matrix method-theory and applications. *IEEE Trans. Micro. The. & Tech.* 33.10 (1985): 882-893.
- [70] G. Xiaodeng, F. Jinqiong and L. Zhenzheng. Analysis of shear lag effect in box girder bridges. *Civ. Eng. J.* 1 (1983).
- [71] S. Bhalla and M. Sumedha. A refined shear lag model for adhesively

- bonded piezo-impedance transducers. *J. Int. Mater. Sys. & Struc.* 24.1 (2013) 33-48.
- [72] S. Bhalla, P. Kumar, A. Gupta and T. K. Datta. Simplified impedance model for adhesively bonded piezo-impedance transducers. *J. Aero. Eng.* 22.4 (2009) 373-382.
- [73] G. Santoni-Bottai and V. Giurgiutiu. Exact shear-lag solution for guided waves tuning with piezoelectric-wafer active sensors. *AIAA J.* 50.11 (2012) 2285-2294.
- [74] M. M. Islam and H. Huang. Understanding the effects of adhesive layer on the electromechanical impedance (EMI) of bonded piezoelectric wafer transducer. *Smart Mater. Struc.* 23.12 (2014) 125037.
- [75] M. Sumedha and S. Bhalla. Numerical investigations of shear lag effect on PZT-structure interaction: review and application. *Cur. Sci. (Bangalore)* 103.6 (2012) 685-696.
- [76] M. Sumedha and S. Bhalla. A continuum based modelling approach for adhesively bonded piezo-transducers for EMI technique. *Int. J. Sol. Struc.* 51.6 (2014) 1299-1310.
- [77] J. Sirohi and I. Chopra. Design and development of a high pumping frequency piezoelectric-hydraulic hybrid actuator. *J. Int. Mater. Sys. Struc.* 14.3 (2003) 135-147.

- [78] H. M. Zhou, X. J. Zheng and Y. Zhou. Active vibration control of nonlinear giant magnetostrictive actuators. *Smart mater. Struc.* 15.3 (2006) 792.
- [79] M. E. H. Benbouzid, G. Reyne, G. Meunier, L. Kvarnsjo, G. Engdahl. Dynamic modelling of giant magnetostriction in Terfenol-D rods by the finite element method. *IEEE Trans. Mag.* 31.3 (1995) 1821-1824.
- [80] M. Besbes, Z. Ren and A. Razek. A generalized finite element model of magnetostriction phenomena. *IEEE Trans. Mag.* 37.5 (2001) 3324-3328.
- [81] E. Vassent, G. Meunier, A. Foggia and G. Reyne. Simulation of induction machine operation using a step by step finite element method coupled with circuits and mechanical equations. *IEEE Trans. Mag.* 27.6 (1991) 5232-5234.
- [82] N. G. Elvin, A. A. Elvin. A general equivalent circuit model for piezoelectric generators. *J. Int. Mater. Sys. Struc.* 20.1 (2009) 3-9.
- [83] H. A. Tilmans. Equivalent circuit representation of electromechanical transducers: I. Lumped-parameter systems. *J. Micromech. Microeng.* 6.1 (1996) 157.
- [84] H. Muramatsu, E. Tamiya and I. Karube. Computation of equivalent circuit parameters of quartz crystals in contact with liquids and study of

- liquid properties. *Anal. Chem.* 60.19 (1988) 2142-2146.
- [85] R. J. Marks, I. A. Gravagne, J. M. Davis and J. J. DaCunha. Nonregressivity in switched linear circuits and mechanical systems. *Math. Comp. Model.* 43.11-12 (2006) 1383-1392.
- [86] K. Dilip. *Introduction to modern thermodynamics*. Wiley, 2008.
- [87] H. Ozawa, A. Ohmura, R. D. Lorenz and T. Pujol. The second law of thermodynamics and the global climate system: A review of the maximum entropy production principle. *Rev. Geophys.* 41.4 (2003).
- [88] G. Altay, M. C. Dökmeci. Variational principles for piezoelectric, thermopiezoelectric, and hygrothermopiezoelectric continua revisited. *Mech. Adv. Mater. Struc.* 14.7 (2007) 549-562.
- [89] R. C. Smith, M. J. Dapino and S. Seelecke. Free energy model for hysteresis in magnetostrictive transducers. *J. App. Phys.* 93.1 (2003) 458-466.
- [90] Z. Xiaojing and L. Sun. A one-dimension coupled hysteresis model for giant magnetostrictive materials. *J. Mag. Mag. Mater.* 309.2 (2007): 263-271.
- [91] K. Mehdi and M. Ghovanloo. The circuit theory behind coupled-mode magnetic resonance-based wireless power transmission. *IEEE Trans. Circuits Syst. I, Reg. Papers* 59.9 (2012) 2065-2074.

- [92] L. Huang, G. Zhao, H. Nian and Y. He. Modeling and design of permanent magnet biased radial-axial magnetic bearing by extended circuit theory. 2007 ICEMS. IEEE, (2007).
- [93] D. L. Atherton and M. G. Daly. Finite element calculation of magnetic flux leakage detector signals. *NDT. Int.* 20.4 (1987) 235-238.
- [94] J.-C. Hong, K.H. Sun and Y.Y. Kim, The matching pursuit approach based on the modulated Gaussian pulse for efficient guided-wave damage inspection, *Smart Mater. Struct.* 14 (2005) 548–560.
- [95] R. B. Thompson. Mechanisms of electromagnetic generation and detection of ultrasonic Lamb waves in ironnickel alloy polycrystals. *J. Appl. Phys.* 48 (1977) 4942–50.
- [96] L. Laguerre, J. C. Aime and M. Brissaud. Magnetostrictive pulse-echo device for non-destructive evaluation of cylindrical steel materials using longitudinal guided waves. *Ultrasonics* 39 (2002) 503–14.
- [97] J. S. Lee, Y. Y. Kim and S. H. Cho. Beam-focused shearhorizontal wave generation in a plate by a circular magnetostrictive patch transducer employing a planar solenoid array. *Smart Mater. Struct.* 18 (2009) 015009.
- [98] J. S. Lee, H. W. Kim, B. C. Jeon, S. H. Cho and Y. Y. Kim. Damage detection in a plate using beam-focused shearhorizontal wave

- magnetostrictive patch transducers. *AIAA J.* 48 (2010) 654–63.
- [99] E. Saidha, G. N. Naik and S. Gopalkrishnan. An experimental investigation of a smart laminated composite beam with a magnetostrictive patch for health monitoring applications. *Struct. Health Monit.* 2 (2003) 273–92.
- [100] L. Zhou, Y. Yang and F-G. Yuan. Design of a magnetostrictive sensor for structural health monitoring of non-ferromagnetic plates. *J. Vibroeng.* 14 (2012) 280–91.
- [101] A. Bybi, C. Granger, S. Grondel, A. C. Hladky-Hennion and J. Assaad. Electrical method for crosstalk cancellation in transducer arrays. *NDT E Int.* 62 (2014) 115–21.
- [102] R. Murayama. Study of driving mechanism on electromagnetic acoustic transducer for Lamb wave using magnetostrictive effect and application in drawability evaluation of thin steel sheets. *Ultrasonics* 37 (1999) 31–8.

ABSTRACT (KOREAN)

비틀림과 자기변형 패치 트랜스듀서의 정량화를 위한 등가 회로 모델 연구

이 준 규

서울대학교 대학원

기계항공공학부

본 논문에서는 최저차 비틀림 모드인 $T(0,1)$ 탄성파를 가진, 그리고 측정하도록 설계된 자기변형 패치 트랜스듀서에 대한 완전 결합 회로 모델을 구축하고자 한다. 다양한 타입의 자기변형 패치 트랜스듀서가 개발되어 왔지만 트랜스듀서의 가진과 측정 메커니즘을 정확하게 고려하고 이를 표현한 회로 모델에 대한 연구는 제한적이었다. 특히, 정교하면서도 가진과 측정에서 동시에 사용할 수 있는 회로 모델의 경우는 아직까지 제시된 바가 없다. 모델을 통한 정량화 연구와 이에 따른 응용이 상당히 진행된 압전 트랜스듀서와 달리 자기변형 패치 트랜스듀서의 경우는 이러한 모델의 부재로 인해 정량화와 응용 측면에서 한계를 가졌다. 따라서 본 연구에서는 자기변형 패치 트랜스듀서의 정량화를 목표로 완전 결합 회로 모델을 설계하고 이에 대한 검증을 수행하였다.

정량적 회로 모델을 설계하기에 앞서, 기존의 단순화된 자기변형 구성 방정식을 통해 얻은 결과값을 스트레인 게이지와 상대적 비교를 하였으며 해당 결과는 자기변형 패치 트랜스듀서의 정량화 가능성을 확인해준다. 실제 회로 모델 설계에 있어서, 구조적 임피던스를 통해 시편과 트랜스듀서의 물리적 구조를 동시에 고려하였으며 자기변형 패치 내의 비선형성 자기변형 현상을 물성치와 함께 고려하여 등가 회로로 표현하였다. 특히, 자기변형 현상에 큰 영향을 주는 자석에 의한 정자기장도 회로 안에 함께 고려하여 가진과 측정, 두 방향성을 가질 수 있도록 설계하였다. 구조적 임피던스와 등가 회로를 하나로 모은 모델은 트랜스듀서에서 얻은 전압을 실제 변형률값으로 전환해주며 반대의 작용 또한 가능케 한다. 개발된 완전 결합 회로 모델은 검증된 스트레인 게이지와의 비교 실험들을 통해서 다양한 변수에 대한 유효성을 입증하였다.

주요어: 유도초음파, 자기변형, 자기변형 패치 트랜스듀서, 정량화, 등가 회로

학 번 : 2012-23944

ACKNOWLEDGEMENTS

This research was supported by the National Research Foundation of Korea (NRF) grant No. 2014M3A6B3063711, No. 2015021967 and No. 2015049675 funded by the Korean Ministry of Science, ICT & Future Planning and contracted through the Institute of Advanced Machinery and Design at the Seoul National University.